

**Synthesis and mechanical characterization of wet chemically grown ZnO
nanowires for nanoelectromechanical sensors**

**Nedves kémiai úton növesztett ZnO nanoszálak előállítása és vizsgálata
nanoelektromechanikai érzékelők fejlesztése céljából**

DOKTORI (PhD) ÉRTEKEZÉS

Erdélyi Róbert



Pannon Egyetem - Műszaki Informatikai Kar

Molekuláris- és Nanotechnológiák Doktori Iskola

vezetője: Prof. Dr. Vonderviszt Ferenc, DSc

Témavezető: Dr. Volk János, PhD

Magyar Tudományos Akadémia Természettudományi Kutatóközpont

Műszaki Fizikai és Anyagtudományi Intézet

2014

Synthesis and mechanical characterization of wet chemically grown ZnO nanowires for nanoelectromechanical sensors

Értekezés doktori (PhD) fokozat elnyerése érdekében

Írta:

Erdélyi Róbert

Készült a Pannon Egyetem Molekuláris- és Nanotechnológiák Doktori Iskolája keretében

Témavezető: Dr. Volk János

Elfogadásra javaslom (igen / nem)

(aláírás)

A jelölt a doktori szigorlaton % -ot ért el,

Az értekezést bírálóként elfogadásra javaslom:

Bíráló neve: igen/nem

.....

(aláírás)

Bíráló neve: igen/nem

.....

(aláírás)

Bíráló neve: igen/nem

.....

(aláírás)

A jelölt az értekezés nyilvános vitáján % -ot ért el.

Veszprém,

.....

A Bíráló Bizottság elnöke

A doktori (PhD) oklevél minősítése:

.....

Az EDHT elnöke

Table of contents

Abstract.....	7
Magyar nyelvű kivonat.....	8
Abstract (Deutsch).....	9
Abbreviations.....	10
1. Introduction.....	11
1.1. Motivation.....	11
1.2. ZnO nanowires and nanorods as building blocks of future nanodevices.....	11
1.2.1. Physical properties of ZnO.....	11
1.2.2. Vapor-phase synthesis of ZnO nanowires and nanorods.....	14
1.2.3. Wet chemical growth of ZnO nanowires and nanorods.....	15
1.2.4. Applications of ZnO nanowires and nanorods.....	17
1.3. Mechanical characterization of nanowires, nanorods and nanotubes.....	23
1.3.1. Electrically and mechanically induced resonance analysis.....	24
1.3.2. Mechanical characterization via axial loading.....	28
1.3.3. Atomic force microscopy based methods.....	31
1.3.4. Other nanomechanical methods.....	34
1.3.5. Mechanical characterization of ZnO NWs/NRs.....	37
2. Methods.....	38
2.1. Two dimensional X-ray diffraction.....	38
2.2. Transmission electron microscopy.....	38
2.3. Field emission scanning electron microscopy.....	39
2.4. Focused ion beam etching.....	40
2.5. Electron-beam lithography.....	40
2.6. Nanomanipulation inside the SEM.....	40
2.7. Atomic force microscopy.....	41
2.8. Finite element method.....	42

3. Design of a novel ZnO nanowire based nanoforce sensor.....	44
4. Substrate effect on the growth of vertical zinc-oxide nanowires.....	50
4.1. Experimental subsection.....	52
4.2. Results and discussion.....	57
4.2.1. SEM and AFM study of the NWs and the different seed layers.....	57
4.2.2. Structural characterization of the NWs and the corresponding seed layers.....	60
4.2.3. Piezoelectric characterization of the NWs.....	64
4.2.4. The effect of seed layer annealing.....	65
5. Validation of the static bending test inside the SEM.....	69
5.1. Experimental subsection.....	71
5.2. Results and discussion.....	73
5.2.1. SEM and TEM study of the InAs nanowires.....	73
5.2.2. Bending modulus of wurtzite InAs nanowires.....	75
6. Mechanical characterization of epitaxially grown ZnO nanorods.....	82
6.1. Experimental subsection.....	82
6.2. Results and discussion.....	83
7. Towards the integrated nanomechanical sensor.....	88
7.1. Synthesis of individual vertical ZnO NWs.....	88
7.1.1. Experimental.....	89
7.1.2. Results and discussion.....	90
7.2. 1D mechanically gated ZnO thin film transistor.....	91
7.2.1. Experimental.....	91
7.2.2. Results and discussion.....	93
8. Summary.....	96
9. Thesis highlights.....	98
10. List of publications.....	100
11. Acknowledgements.....	102
12. Appendix.....	103

12.1. Elasticity theory of wurtzite crystals.....	103
12.2. Piezoelectric theory of wurtzite ZnO.....	104
References.....	106

Abstract

In this thesis the synthesis and mechanical characterization of wet chemically grown ZnO nanowires (NWs) as potential transducers of novel electromechanical sensors are detailed. At first the impact of various ZnO templates on their alignment and geometry was investigated. Scanning electron microscopy, X-ray diffraction, and transmission electron microscopy revealed that the alignment, crystal structure, and geometry of the NW arrays were dictated by the crystal structure of the underlying ZnO. The mechanical properties of the individual NWs were also examined *in situ* inside a scanning electron microscope by a static bending test. The mean bending modulus was measured to be 32.2 GPa, which is significantly lower than that of the bulk ZnO. The validation of the bending test by the more standard resonance excitation method and the piezoelectric characterization of the NWs were also addressed.

Magyar nyelvű kivonat

A disszertációban a szerző egy új típusú, nanoszál alapú erőmérő megvalósítása közben elvégzett anyagtudományi, mechanikai, és mérés technikai kutatásait mutatja be.

A leendő érzékelő olcsó és egyszerű gyártása megköveteli, hogy a ZnO nanoszálak integrálhatóak legyenek a standard félvezető technológiába, azaz azokat hagyományos hordozókon (pl. szilícium, zafír), kontrollálható geometriában ki lehessen alakítani. Ennek érdekében a szerző először a különféle ZnO magrétegek hatását vizsgálta a nedves kémiai úton növesztett ZnO nanoszálak rendezettségére és geometriájára. Atomi erőmikroszkópos, elektronmikroszkópos és röntgendiffrakciós vizsgálatok kimutatták, hogy a nanoszálak rendezettségét, kristályszerkezetét és geometriáját a magréteg kristályszerkezete határozza meg, míg a felületek érdességének észlelhető hatása nem volt. A szerző szintén kimutatta, hogy a polikristályos magrétegek hőkezelésével a nanoszálak rendezettsége nagymértékben javítható. A vezető rétegre növesztett nanoszálak piezoelektromos válaszát pásztázó tűszondás mikroszkóppal vizsgálva sikerült meghatározni a ZnO nanurudak c-tengely irányú diagonális tenzorkomponensét (d_{33}).

A disszertációban a szerző ezután egy sok tekintetben újszerű, statikus nanomechanikai módszert hitelesít egy általánosabban elterjedt dinamikus mérési technikával, melyhez karcsú InAs nanoszálakat használ modell anyagként. Az elektronmikroszkópban végzett *in situ* összehasonlító vizsgálatok során az egyik manipulátor karra egy kalibrált atomi erőmikroszkópos tű, míg a másikra egy hegyes volfrám tű volt rögzítve. Előbbi lehetővé tette az egyedi nanoszálak *in situ* statikus hajlítgatását adott kristálytani irányban, míg utóbbival ugyanezen szálak mechanikai rezonanciájának elektromos térrel való gerjesztése történt. A szerző megmutatta, hogy a két módszer hasonló eredményre vezet. A sikeresen hitelesített hajlítós módszert ezután a szerző a mechanikai szenzorba szánt, alacsony oldalarányú ZnO nanorudak hajlítási modulusának meghatározására használta, melynek kiértékelése során a szálak hossz tengely menti keresztmetszetének inhomogenitását egy két részből felépülő mechanikai modellel vette figyelembe. A hajlítási modulus (32.2 GPa) a tömbi ZnO Young-modulusánál jóval kisebb értéknek adódott (140 GPa a [0001] irányban).

Végezetül a szerző egy 1 dimenziós mechanikus úton vezérelt vékonyréteg tranzisztort állított elő, amelynek elektromechanikai tesztelése során megmutatta, hogy a nedves kémiai úton növesztett ZnO nanoszálak alapját képezhetik egy nanoelektromechanikai érzékelőnek.

Abstract (Deutsch)

Synthese und mechanische Charakterisierung von durch nass-chemisches Verfahren gewachsenen Nanodrähten für nanoelektromechanische Sensoren

In dieser Abhandlung werden die Synthese und die mechanische Charakterisierung von durch nass-chemisches Verfahren gewachsenen ZnO Nanodrähten als potentielle Transducers von neuartigen elektromechanischen Sensoren behandelt. Durch Rasterelektronenmikroskopie, Röntgendiffraktion und Transmissionselektronenmikroskopie wurde erwiesen, dass die Anordnung, die Kristallstruktur und die Geometrie der Nanodrähte durch die Kristallstruktur des darunter liegenden ZnO Templates bestimmt wurden. Die mechanischen Eigenschaften der einzelnen Nanodrähte wurden auch *in situ* im Rasterelektronenmikroskop durch einen statischen Biegungstest untersucht. Der durchschnittliche Youngscher Modul bei Biegung beträgt 32.2 GPa. Die Validierung des Biegungstests durch die standardisierte Resonanzanregungsmethode und die piezoelektrische Charakterisierung der Nanodrähten wurden auch behandelt.

Abbreviations:

AFM:	atomic force microscope
ALD:	atomic layer deposition
BF:	bright-field
BM:	bending modulus
CMOS:	Complementary Metal–Oxide–Semiconductor
CVD:	chemical vapor deposition
DF:	dark-field
DLC:	diamond-like carbon
DSSC:	dye-sensitized solar cell
FEM:	finite element method
FE-SEM:	field emission scanning electron microscope
FIB:	focused ion beam
FWHM:	full width at half maximum
HMT:	hexamethylenetetramine
HRTEM:	high-resolution transmission electron microscopy
LED:	light emitting diode
LF:	lateral force
MBE:	molecular beam epitaxy
MEMS:	microelectromechanical systems
MOCVD:	metal-organic chemical vapor deposition
NEMS:	nanoelectromechanical systems
NF:	normal force
NR:	nanorod
NT:	nanotube
NW:	nanowire
PCCW:	precursor concentration controlling window
PFM:	piezoresponse force microscopy
PLD:	pulsed laser deposition
PMMA:	poly(methyl methacrylate)
PoC:	proof-of-concept
PSPD:	position sensitive photo detector
RMS:	root mean square
SAED:	selected area electron diffraction
SEM:	scanning electron microscope
TEM:	transmission electron microscope
TRCC:	truncated right circular cone
TRHC:	truncated right hexagonal cone
UV:	ultraviolet
VLS:	vapor-liquid-solid
VS:	vapor-solid
XRD:	X-ray diffraction

1. Introduction

1.1. Motivation

The challenges of building ZnO nanowire (NW) based NEMS (nanoelectromechanical systems) devices can be addressed on the following fronts: integration of the NWs into silicon technology; mechanical characterization in the nano-range with high confidence; electrical and electromechanical exploration; design and realization of the integrated device; characterization of the device performance. This thesis contributes mainly to the first two goals, through the following studies:

- Investigating into the impact of the template layer on ZnO NW arrays made using low temperature wet chemical growth.
- Comparison of two independent existing *in situ* methods in scanning electron microscope (SEM) for the exploration of the elastic properties of one dimensional nanostructures; examination of epitaxial ZnO NWs in this manner.

In the introductory sections the basic physical properties of ZnO, and the fabrication routes and importance of ZnO NWs and nanorods (NRs) will be presented. The relevant existing experimental investigation methods of the mechanical properties of NWs, NRs, and nanotubes (NTs) will be also addressed. Then, after a short overview of the applied experimental techniques (see chapter 2), I propose the design of a novel vertical ZnO NR based integrated nanoforce sensor (see chapter 3) and my contributions to the development of such an integrated NEMS device will be described (see chapters 4, 5, 6, and 7).

1.2. ZnO nanowires and nanorods as building blocks of future nanodevices

1.2.1. Physical properties of ZnO

ZnO is a II-VI compound semiconductor. Under different growth conditions ZnO can crystallize into three structures: wurtzite, zinc blende, and rocksalt. Under ambient conditions the thermodynamically most stable phase is wurtzite, which is composed of two interpenetrating hexagonal close packed (hcp) sublattices (Fig. 1a) [1]. The measured lattice

parameters of the hexagonal wurtzite ZnO are $a = 3.249 \text{ \AA}$ and $c = 5.206 \text{ \AA}$. It belongs to the space group of C_{6v}^4 in the Schönflies notation [2]. Both Zn and O atoms are tetrahedrally coordinated to each other giving rise to polar asymmetry along the c -axis.

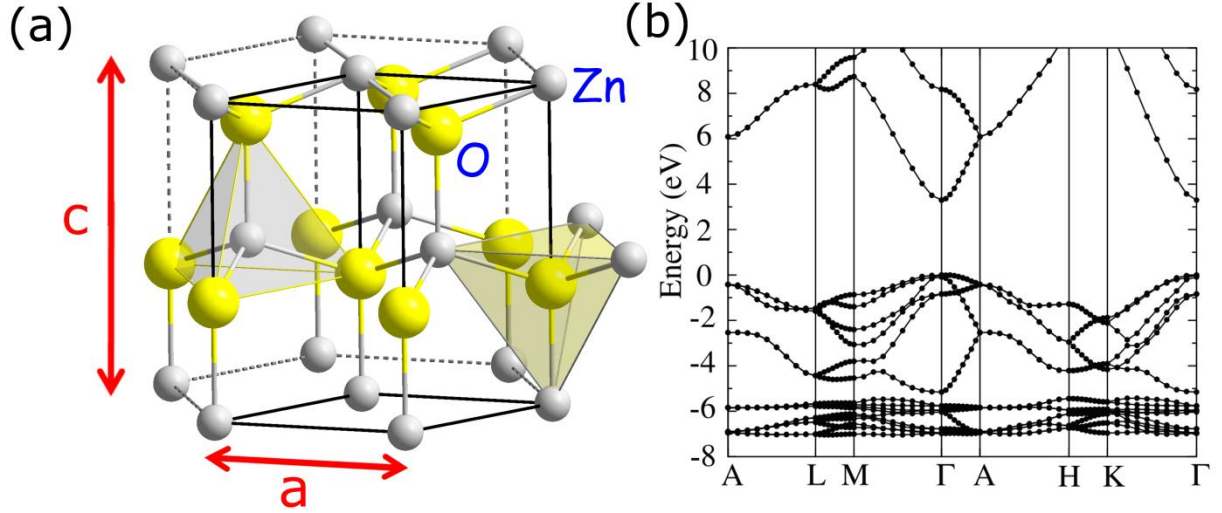


Figure 1. Atomic lattice of ZnO wurtzite crystal showing the tetrahedral coordination of the Zn and O atoms (a) (image a adapted from [3]). Calculated electronic band structure of wurtzite ZnO using the hybrid functional method (b) (image b adapted from [4]).

This polar nature results in many interesting properties, such as piezoelectricity, spontaneous polarization, crystal growth, polarity dependent chemical stability, and defect generation. The Zn terminated (0001) and O terminated $(000\bar{1})$ faces are polar in nature, while the $(11\bar{2}0)$ and $(10\bar{1}0)$ are nonpolar. In other words piezoelectricity is the result of the lack of centrosymmetry. Piezoelectric crystals produce an electric polarization in response to mechanical deformation as described in the Appendix (see subsection 12.2.). The piezoelectric tensor elements of ZnO are comparable to those of other wurtzite type materials, such as AlN, GaN, and InN (Table 1.).

<i>material</i>	e_{33}	e_{31}	e_{15}
ZnO	0.89	-0.51	-0.45
AlN	1.46	-0.60	-0.48
GaN	0.73	-0.49	-0.3
InN	0.97	-0.57	

Table 1. Comparison of bulk piezoelectric moduli of different wurtzite type materials (C/m^2) (data are from [5]).

The electronic band structure of wurtzite ZnO can be determined by theoretical calculations using, for instance, hybrid functional method (HFM) [4]. It can be seen in Fig. 1b that both the valence band maxima and the conduction band minima occur at the Γ point $k = 0$

indicating that ZnO is a direct band gap semiconductor. The band gap of ZnO is 3.44 eV at 0 K and 3.37 eV at room temperature [4], therefore it can be considered as a wide band gap semiconductor. The electronic band structure was determined experimentally by Ivanov *et al.* using electron energy loss spectroscopy (EELS) and ultraviolet photoelectron spectroscopy (UPS) for wurtzite ZnO [6]. It turned out that the Zn face possesses more covalent character, arising from the Zn 4s – O 2p states, while the O face is more ionic.

Defect chemistry plays a very important role in controlling the electrical transport properties of ZnO [4]. Naturally, unintentionally doped ZnO shows n-type conduction with an electron concentration of about 10^{16} – 10^{17} cm⁻³ [7], however, the origin of this n-type conductivity has not been completely understood. Earlier it was believed that the n-type conduction originates due to native defects such as oxygen vacancies (O_v) and zinc interstitials (Zn_i). Look *et al.* [8] suggested that Zn_i are the dominant shallow donors, rather than O_v , with an ionization energy of about 30–50 meV. However, first-principle calculations show that both O_v and Zn_i have high formation energies in n-type ZnO, and therefore none of these native defects are shallow donors [9]. Van de Walle [10] has theoretically shown that H is likely to be the dominant background shallow donor in ZnO materials that are exposed to H during growth. Since the H mobility is large, it can easily diffuse into ZnO in any kind of growth technique. A recent theoretical calculation of Kim and Park [11] suggests that the Coulombic attraction between O_v and Zn_i acts as shallow donors in ZnO. Intentional n-type doping is relatively well established through the substitution of group III elements (Al, Ga, In) on the Zn sites or group VII elements (Cl, Br, I) on the O sites [1] enabling the use of ZnO as a transparent conductive oxide (TCO) material. Park *et al.* e.g. demonstrated Ga doped ZnO (GZO) films showing a low electrical resistivity of $8.12 \cdot 10^{-5}$ Ω cm [12].

ZnO shows strong doping asymmetry (unipolarity), i.e. doping of n-type carriers into the lattice is easy, however, similarly to most wide band gap semiconductors such as GaN, ZnS, SiC, and ZnSe p-type doping is rather challenging [13]. The problem of p-type doping in ZnO can arise for several reasons such as (i) acceptor dopants may be compensated by the native donors (O_v and Zn_i) and background H impurities, (ii) low solubility of the acceptor dopant impurities, and (iii) high activation energy of acceptors (deep impurity level) [14]. The possible p-type dopants in ZnO are group IA and IB elements (Li, Na, K, Ag, and Cu), group V elements (N, P, Sb, and As), and Zn vacancies (Zn_v) [15-17]. It has been also demonstrated experimentally that the band gap of ZnO can be tuned from 2.1 to 6.0 eV by developing $Cd_xZn_{1-x}O$ and $Mg_yZn_{1-y}O$ alloys [1]. ZnO is a promising material for optical and

optoelectronic applications as well, due to its wide and direct band gap, high exciton binding energy (60 meV), and ability to efficient radiative recombination [1].

ZnO in nanostructured form can be easily synthesized by physical methods at high temperature and by chemical methods at low temperature as well. Beside the above attracting physical properties, the economic, even wafer scale fabrication of ZnO nanostructures makes them promising candidates as building blocks for novel nanosized devices. Quasi-one-dimensional ZnO nanostructures (i.e. NWs, NRs, whiskers) are especially important from this aspect. In the literature terms ‘nanowire’ and ‘nanorod’ are usually applied as synonyms, or the ones with lower aspect ratio are frequently referred to as ‘nanorods’, however there is no general consensus. In this thesis both denominations are applied. The existing growth methods can be grouped into two categories: vapor-phase synthesis and solution-phase growth.

1.2.2. Vapor-phase synthesis of ZnO nanowires and nanorods

In vapor-phase synthesis a condensed or powder source material is vaporized at elevated temperature, and then the resultant vapor phase condenses at certain conditions (temperature, pressure, atmosphere, substrate, etc.) to form the NWs with desired morphology. In order to control the diameter, aspect ratio, and crystallinity, a number of different deposition techniques can be applied including chemical vapor deposition (CVD), direct thermal evaporation, pulsed laser deposition (PLD), metal–organic chemical vapor deposition (MOCVD), etc. [18]. Growth can take place in two mechanisms. The vapor-liquid-solid (VLS) mechanism starts with the dissolution of gaseous reactants into nanosized liquid droplets of a catalyst metal, and followed by nucleation and growth of single-crystalline rods and then wires. The one dimensional growth is induced and dictated by the liquid droplets, whose sizes remain essentially unchanged during the entire process of wire growth (Fig. 2a). Each liquid droplet serves as a virtual template to strictly limit the lateral growth of an individual wire [19]. In vapor-solid mechanism (VS) source materials are vaporized under high temperature condition and then directly condensed on the substrate placed in the low temperature region. Once the condensation process takes place, the initially condensed molecules form seed crystals serving as the nucleation sites. As a result, they facilitate directional growth to minimize the surface energy [20].

Fig. 2b shows SEM image of an array of vertical ZnO NWs grown by the VLS mechanism using Au particles as catalyst. The epitaxial growth on the $c\text{-Al}_2\text{O}_3$ substrate yields well-aligned distribution. The transmission electron microscopy (TEM) image of the NWs with the gold catalyst at their tips is shown in Fig. 2c [21].

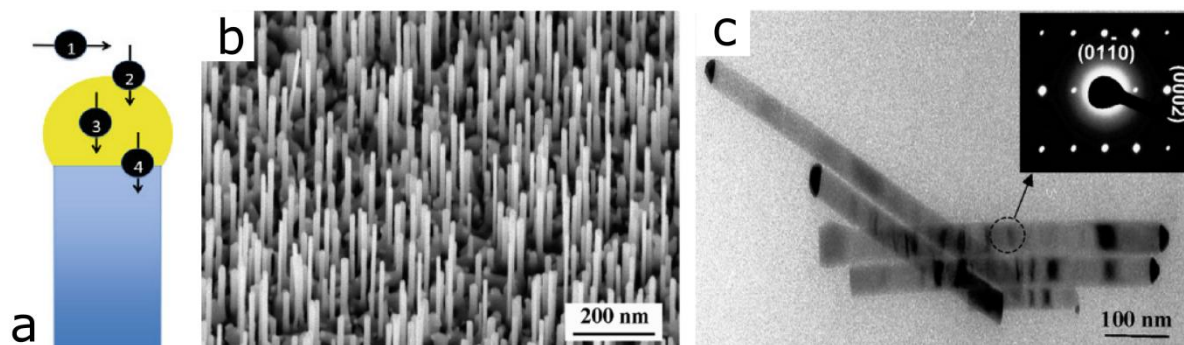
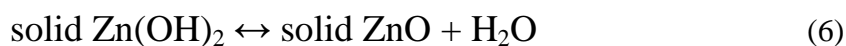
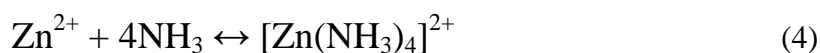
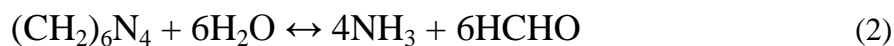


Figure 2. Kinetic steps in VLS mechanism (a): (1) mass transport in the gas phase; (2) chemical reaction on the vapor–liquid interface; (3) diffusion in the liquid phase; and (4) incorporation of atoms in a crystal lattice (image a adapted from [22]). SEM micrograph of vertical ZnO NWs grown on $c\text{-Al}_2\text{O}_3$ substrate by the VLS mechanism using Au particles as catalyst (b). The epitaxial growth on $c\text{-Al}_2\text{O}_3$ yields well-aligned distribution. TEM image of the NWs with Au catalyst at their tips (c). Inset is an electron diffraction pattern recorded from a NW (images b-c adapted from [21]).

1.2.3. Wet chemical growth of ZnO nanowires and nanorods

Usually the gas-phase synthesis methods are expensive and their up-scaling is challenging. In the solution-phase synthesis, the growth process is carried out in a liquid. In most cases aqueous solutions are used and the process is referred to as wet chemical growth process. The wet chemical process of growing ZnO nanostructures has gained immense popularity due to its simplicity and tolerable growth conditions. As synthesis is carried out in aqueous solution, the growth temperatures are lower than the boiling point of water. The wet chemical growth of ZnO nanostructures was first reported by Vergés *et al.* [23]. However, it did not gain much interest till Vayssieres *et al.* [24-25] successfully used the method for the controlled fabrication of ZnO NWs on glass and Si substrates by the thermal decomposition of hexamethylenetetramine ($(\text{CH}_2)_6\text{N}_4$) (HMT) and zinc nitrate ($\text{Zn}(\text{NO}_3)_2$). To initiate the growth from the substrate, a thin layer of ZnO nanoparticles was grown on the substrate (Fig. 3). Note that without any ZnO seed the growth can be hardly initiated. As a counterexample, Yuan *et al.* produced wet chemically grown ZnO NW arrays through heteroepitaxial growth on patterned GaN substrates due to the small lattice mismatch between the GaN substrate plane and the ZnO plane [26]. HMT is a highly water soluble, non-ionic tetradentate cyclic

tertiary amine. Thermal degradation of HMT releases hydroxyl ions which react with Zn^{2+} ions to form ZnO [27]. The ZnO deposition process undergoes by forwarding the intermediate reactions (1)-(6) in equilibrium, which helps to realize stationary growth [28].



Here, NH_3 plays roles as weak base (pH buffer: pH =10.5) in Eq. (3) and $[Zn^{2+}]$ buffer in Eq. (4). Since single zinc nitrate hexahydrate molecule yields single zinc ion in Eq. (1) and single HMT molecule in weak base yields 4 hydroxide ion in Eq. (2), ZnO NR grows in $[Zn^{2+}] < [OH^-]$ condition and is controlled by $[Zn^{2+}]$. It is a general acceptance that the role of HMT is to supply the hydroxyl ions to drive the precipitation reaction [29]. The formation of NRs rather than thin films is due to the different surface energies of different planes in the case of wurtzite ZnO. The surface formation energy of (0001) plane is the highest while that of $\{10\bar{1}0\}$ is the lowest [30]. Therefore ZnO has a tendency to minimize the area of the (0001) plane for minimized total surface energy.

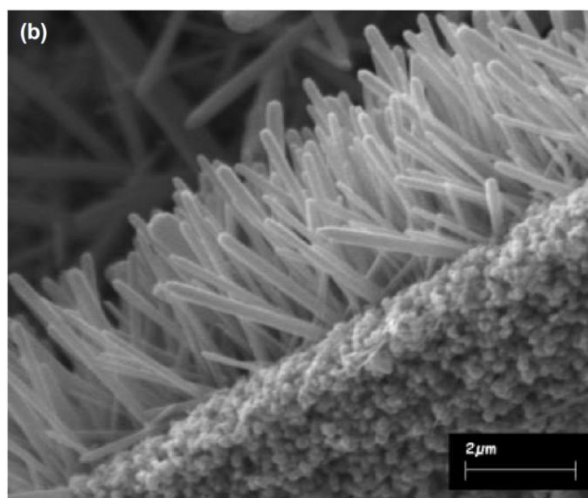


Figure 3. SEM image showing an array of ZnO NRs grown by the aqueous chemical method onto a ZnO nanostructured thin film (image adapted from [25]).

In this thesis the wet chemical approach was applied for ordered growth of vertical ZnO NWs, since the method has several advantages such as, low cost, low temperature, simple, and provides high yield on ZnO coated substrates.

1.2.4. Applications of ZnO nanowires and nanorods

In the last decade, ZnO NWs and NRs have been receiving a great deal of interest due to their unique properties for electronic and optoelectronic applications. A variety of ZnO NW based devices have been demonstrated, including field effect transistors, nanogenerators, ultraviolet (UV) lasers, light emitting diodes (LEDs), solar cells, and photodetectors. This section is the review of the above applications. The most productive research group in this field is led by Prof. Zhong Lin Wang at the Georgia Institute of Technology in Atlanta.

Gao *et al.* have applied the perturbation theory for calculating the piezoelectric potential distribution in an anchored vertical ZnO NW as pushed by a lateral force at the top [31]. The analytical solution produced a result that showed very good agreement with the full numerically calculated result using the finite element method (FEM). The calculations show that the piezoelectric potential in the NW almost does not depend on the z-coordinate along the NW unless very close to the two ends. The potential difference occurs between the tensed and compressed sides of the bent piezoelectric NW (Fig. 4a-b). For moderate deflection the maximum potential at the surface of the NW is directly proportional to the lateral displacement of the NW and inversely proportional to the cube of its length-to-diameter aspect ratio. The magnitude of piezoelectric potential for a NW of diameter 50 nm and length 600 nm is ~0.3 V. This potential drop across the NW serves as the gate voltage for the piezoelectric field effect transistor demonstrated by Wang *et al.* [32]. They demonstrated the principle of NW-based nanoforce and nanopressure sensors by building a piezoelectric field effect transistor that is composed of a ZnO NW bridging across two contacts, in which the source to drain current is controlled by the bending of the NW (Fig. 4c-h). The origin of the operation was attributed to the carrier trapping effect (Fig. 4i) and the creation of a charge depletion zone (Fig. 4j) under elastic deformation due to the coupled piezoelectric and semiconducting dual properties of ZnO. They excluded the role of piezoresistivity because of the nearly antisymmetric distribution of the strain across the width of the NW.

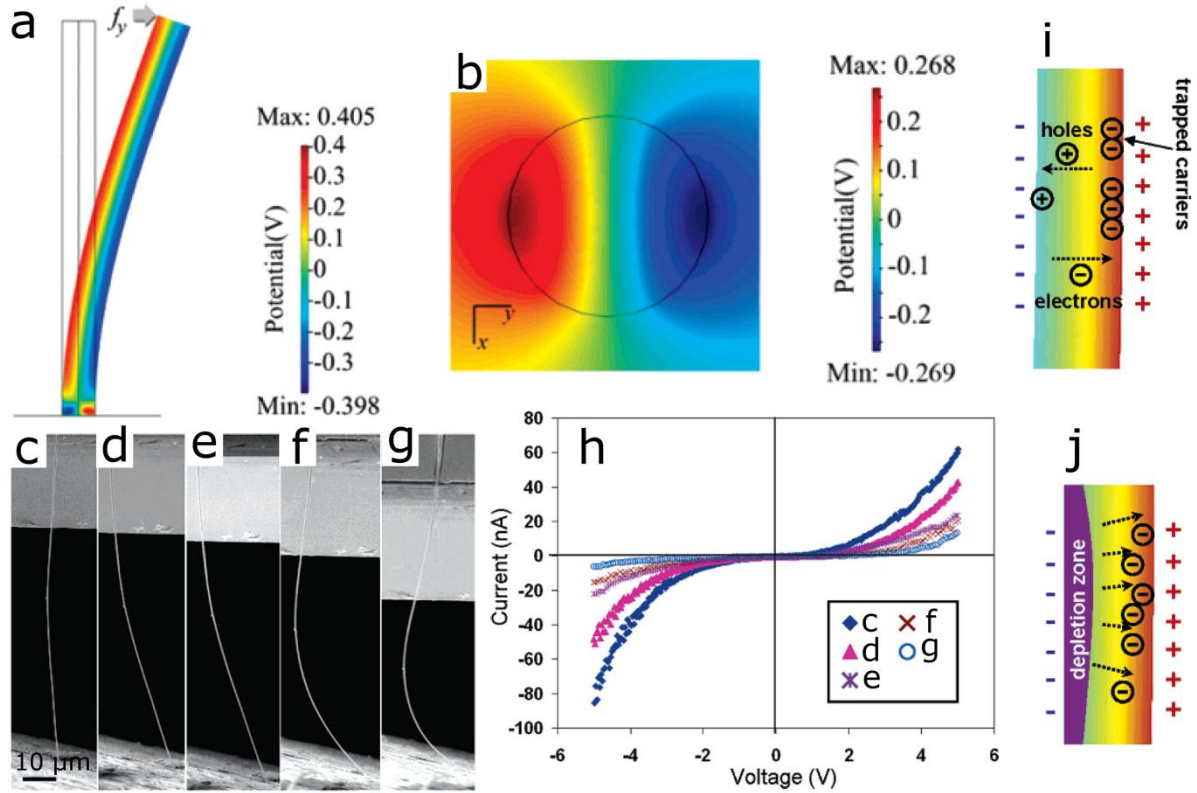


Figure 4. Side (a) and top (b) cross-section of the potential distribution for a ZnO NW with a diameter of 50 nm and a length of 600 nm at a lateral bending force of 80 nN as the result of finite element calculation (images a-b adapted from [31]). SEM images with the same magnification showing the gradual bending of a ZnO NW bridging across two contacts (c-g) and the corresponding I-V characteristics of the ZnO NW for the five different bending cases (h). Schematic of the carrier trapping effect (i) and the creation of a charge depletion zone in the NW (j) as the result of the coupled piezoelectric and semiconducting dual properties of ZnO (images c-j adapted from [32]).

The word ‘piezotronics’ was created by Z. L. Wang from words piezoelectric and electronics. Piezotronic devices are using the piezoelectric potential created in materials with piezoelectricity as a gate to tune the charge carrier transport properties. An assembled piezotronic device for instance was reported recently by Wu *et al.* [33]. They demonstrated large-array three-dimensional circuitry integration of piezotronic transistors based on bundles of wet chemically grown vertical ZnO NWs. The NW bundles serve as pixels of an addressable pressure/force sensor matrix for tactile imaging. The schematic of the device is shown in Fig. 5a. At the bottom and top ends of the NWs metal-semiconductor interfaces are formed by gold contacts leading to Schottky junctions. The origin of the operation of the tactile pixels is the following. During operation the contact between the NWs and top electrodes is reverse biased. Upon applying a normal stress accumulation of piezoelectric charges at both Schottky contacts induces the distribution of piezopotential. Because of the

orientation of the polar c-axis in the as-synthesized ZnO NWs (red arrow in Fig. 5a), negative piezopotential is induced at the reverse-biased top Schottky contact, which raises the barrier height (Fig. 5b inset) at that contact and hence decreases the transport conductance of the device. Fig. 5b shows the current responses for an individual pixel under different pressures, illustrating the gate modulation effect of applied pressure. In other words the operation is based on barrier-interface modulation that enables enhanced sensitivity. The transistors are independently addressable and the device matrix can achieve shape-adaptive tactile imaging and self-powered, multidimensional active sensing. The 3D piezotronic transistor array has plenty of potential applications in human-electronics interfacing, smart skin, and microelectromechanical systems (MEMS). The weak point of the device is its dimensions. The area of one NW bundle ($20\mu\text{m} \times 20\mu\text{m}$) and the spacing between them ($\sim 100\mu\text{m}$) are far above the submicron range.

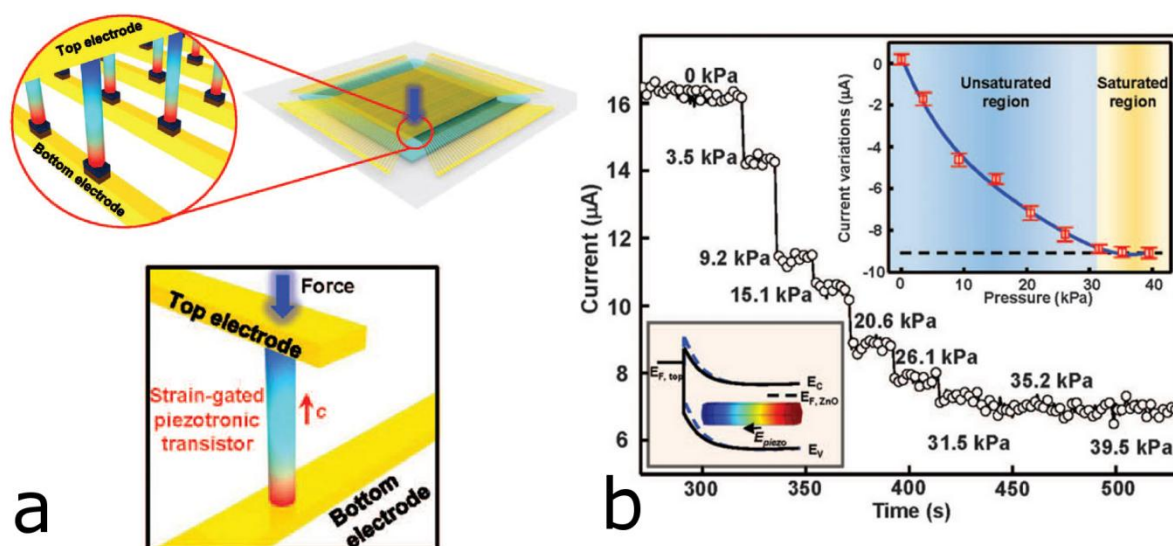


Figure 5. Schematic illustration of the three-dimensional tactile sensor composed of strain-gated piezotronic transistors (a), current responses for an individual pixel under different pressures (b), and schematic band diagram illustrating the change in Schottky barrier height of the reverse-biased top contact due to the modulation effect of strain-induced piezopotential (b inset) (images a-b adapted from [33]).

Wang *et al.* have converted nanoscale mechanical energy into electrical energy by means of ZnO NW arrays deflected with a conductive Pt coated atomic force microscopy (AFM) tip in contact mode [34]. The origin of the operation was attributed to the coupling of piezoelectric and semiconducting properties in ZnO. As it was shown above, the bending of a NW creates a strain field and an electric potential is created by the relative displacement of the Zn^{2+} cations with respect to the O^{2-} anions, as a result of the piezoelectric effect in the wurtzite crystal structure. Thus, these ionic charges cannot freely move and cannot recombine without

releasing the strain, i.e. the potential difference is maintained as long as the deformation is in place and no foreign free charges are injected. The compressed side of the ZnO NW has negative potential and the stretched side has positive potential. Since ZnO is an n-type semiconductor the Pt-ZnO contact between the probe and the NW is a Schottky barrier and dominates the entire transport process. The base of the NW was grounded and an external load of R_L was applied, which is much larger than the resistance R_I of the NW (Fig. 6a). The AFM was scanning across the NW arrays in contact mode. When the AFM conductive tip reaches and bends the NW, it induces the deformation. Hence it is in contact with the stretched surface of positive potential so the metal–semiconductor interface in this case is a reverse-biased Schottky diode, and little current flows (Fig. 6b). When the AFM tip is in contact with the compressed side, the tip–ZnO interface is a positively biased Schottky diode, and it produces a sudden increase in the output electric current (Fig. 6c). The flow of the free electrons from the loop through the NW to the tip will neutralize the ionic charges distributed in the volume of the NW. This approach having the potential of converting mechanical energy into electricity was called "nanogenerator".

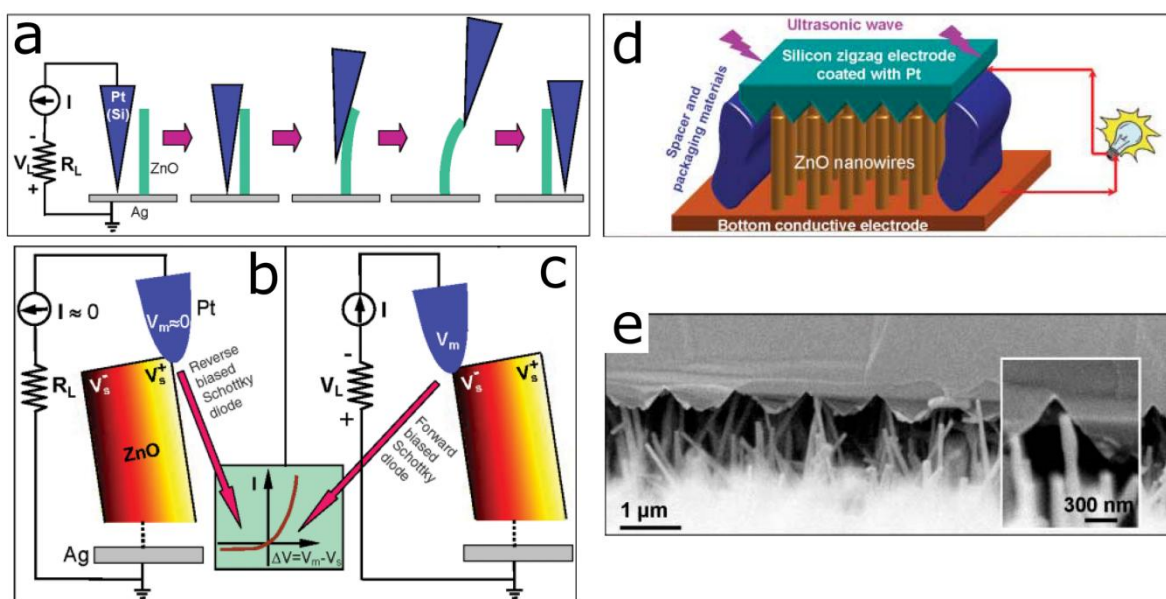


Figure 6. Experimental setup and procedures for generating electricity by deforming a ZnO NW with a conductive AFM tip (a). Schematic of the contacts between the AFM tip and the semiconductor ZnO NW at two reversed local contact potentials (b and c), showing reverse- and forward biased Schottky rectifying behavior, respectively (images a-c adapted from [34]). Schematic of the design and structure of the assembled nanogenerator (d). Cross-sectional SEM image of the nanogenerator, which is composed of aligned NWs and the zigzag electrode (e) (images d-e adapted from [35]).

One year later they demonstrated an assembled device including the vertically aligned NW arrays and a zigzag metal electrode placed above the NWs with a small gap [35] (Fig. 6d-e). The zigzag electrode acts as an array of parallel integrated metal tips that simultaneously and continuously create, collect, and output electricity from all of the NWs. The device is driven by an ultrasonic wave and produces continuous direct-current output. The approach offers the technology for harvesting energy from the environment, and a potential solution for powering nanodevices and nanosystems.

However, Alexe *et al.* soon published a skeptical paper doubting the signal generation mechanism of the nanogenerator, since they have observed similar voltage signals and similar "energy harvesting" from piezoelectric ZnO and nonpiezoelectric Si NW arrays [36]. Among other things they state, that the charge generated in ZnO by the piezoelectric effect will be screened by internal free charges in a very short time. They attributed the measured signals to different sources than the piezoelectric effect, such as features of the measuring instruments and set-up, therefore the energy is rather harvested from the instruments than from the NWs. The operation principle of this vibrating top contact type nanogenerator is still under debate.

Huang *et al.* demonstrated room-temperature UV lasing in vertical <0001> oriented ZnO NW arrays grown on sapphire substrates [37]. The NWs formed natural laser cavities with diameters varying from 20 to 150 nanometers and lengths up to 10 micrometers (Fig. 7a-b). They observed surface-emitting lasing action at 385 nanometers under optical excitation, with an emission linewidth less than 0.3 nanometer. The chemical flexibility and the one-dimensionality of the NWs make them ideal miniaturized laser light sources.

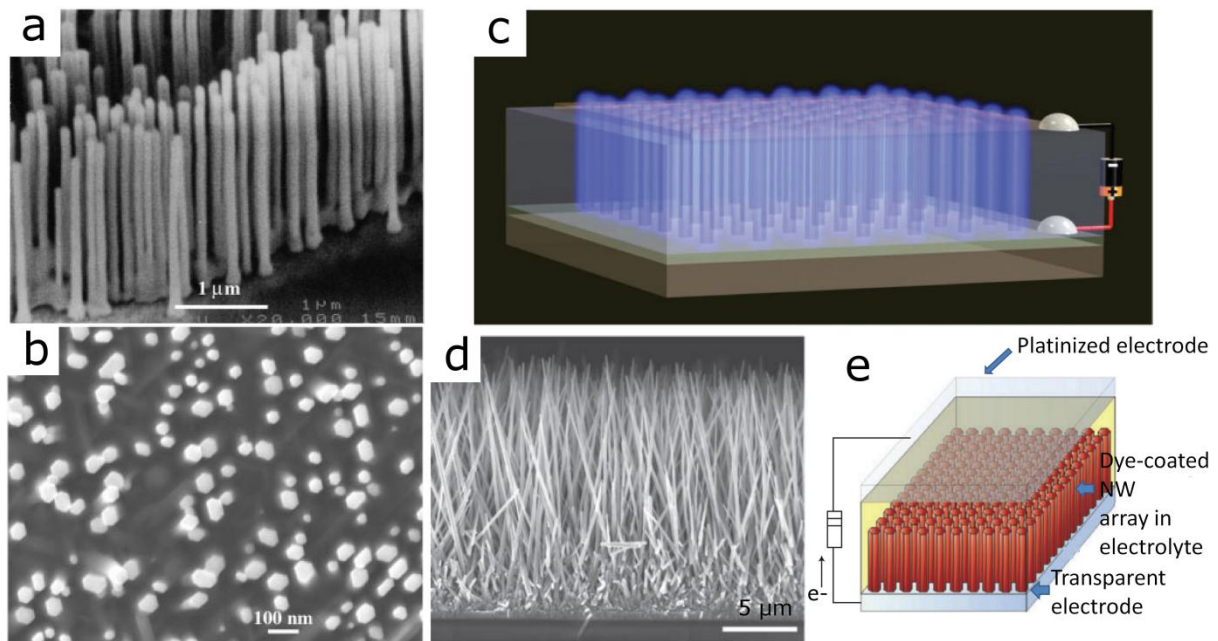


Figure 7. Tilted-view (a) and top-view (b) SEM micrographs of ZnO NWs on sapphire substrate forming natural laser cavities (images a-b adapted from [37]). Design overview of the LED based on ZnO NWs arranged in a controlled pattern on the p-GaN film (c) (image c adapted from [38]). Oriented ZnO NWs replacing the traditional nanoparticle film in a DSSC (d) and the schematic diagram of the cell in which light is incident through the bottom electrode (e) (images d-e adapted from [39]).

Zhang *et al.* demonstrated high-brightness UV–blue electroluminescence from n-ZnO/p-GaN (NWs/film) heterojunction LED devices [40]. They observed a blue shift in the electroluminescence with the increase of bias voltage, indicating the modification of external voltage to the band profile in the depletion region. In addition, the heterojunction LED device exhibited a high sensitivity in responding to UV irradiation. However, the position of these nanosized light sources was not controlled. Xu *et al.* fabricated nanoscale light emitters in the same way but in a controlled pattern on the substrate [38] (Fig. 7c).

Law *et al.* introduced a novel dye-sensitized solar cell (DSSC) in which the traditional nanoparticle film is replaced by a dense array of oriented, crystalline ZnO NWs (Fig. 7d) [39]. Central to this device is a thick film of NWs that provides a large surface area for the adsorption of light-harvesting molecules and direct electrical pathways to ensure the rapid collection of carriers generated throughout the device (Fig. 7e). The ZnO NW anode featured a surface area up to one-fifth as large as a nanoparticle cell. They demonstrated a full Sun efficiency of 1.5%.

Kind *et al.* demonstrated an optical gating phenomenon analogous to the commonly used electrical gating in ZnO NWs [41]. To characterize their photoconducting properties they

electrically contacted individual NWs following two different routes. The NWs were dispersed directly on pre-fabricated gold electrodes, and electron-beam lithography was used to fabricate Au electrodes on top of the NWs as well. The conductivity of the ZnO NWs proved to be extremely sensitive to UV light exposure, as shown on Fig. 8. Therefore these NWs have become promising candidates for applications such as highly sensitive UV light detectors, chemical and biological sensors, and switching devices for nanoscale optoelectronics. Yang *et al.* demonstrated the coupling of piezoelectric, optical, and semiconducting properties of ZnO NWs by fabricating a metal-semiconductor-metal photodetector [42]. During testing the device they applied axial compressive or tensile strain in the wire. The responsivity of the photodetector was enhanced upon UV light illumination onto the wire by introducing a -0.36% compressive strain in the wire, which effectively tuned the Schottky barrier height at the contact by the produced local piezopotential. Three-way coupling of semiconducting, photonic and piezoelectric properties of semiconductor NWs (i.e. piezo-phototronics) offers the possibility to tune and control the electro-optical processes by strain induced piezopotential.

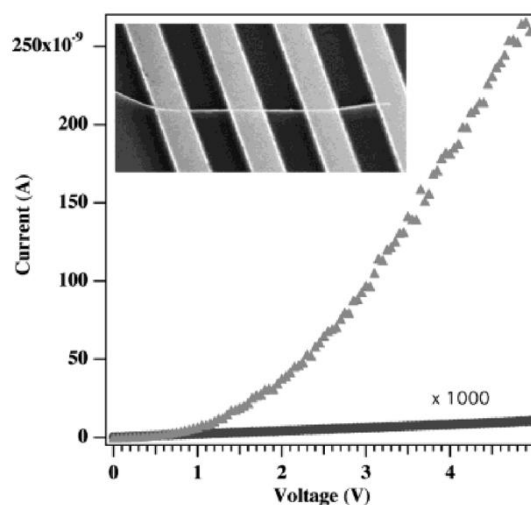


Figure 8. I-V curves showing dark current and photocurrent of a single ZnO NW under 365 nm, 0.3 mWcm^{-2} UV light illumination. The inset reveals a SEM micrograph of a 60 nm ZnO NW bridging four Au electrodes (image adapted from [41]).

1.3. Mechanical characterization of nanowires, nanorods and nanotubes

Mechanical characterization in the nanorange is highly challenging and often requires long and complicated sample preparation. Several techniques were developed by a number of

groups for measuring the elastic modulus and/or the strength of individual one dimensional nanostructures. Existing NW/NR/NT mechanical characterization techniques in the literature can be grouped into the following categories.

1.3.1. Electrically and mechanically induced resonance analysis

The oscillation of one-end-affixed NWs/NRs/NTs can be induced by an alternating electric field (Fig. 9a) or by periodic mechanical excitation (Fig. 9b) as well. These kinds of experiments aim to determine the natural resonance frequency, which can be related to mechanical properties. The weak point of this method is that it is limited to the elastic properties of the nanostructures, i.e. deformation, defect initiation mechanisms, and fracture/tensile strength cannot be determined. The experiments are usually carried out in SEM or TEM. Although the size of specimen stage in TEM is very limited, it has the advantage that the crystal quality of the examined nanostructures can be simultaneously observed. On the other hand, in SEM the experiments are rather comfortable due to larger specimen stage.

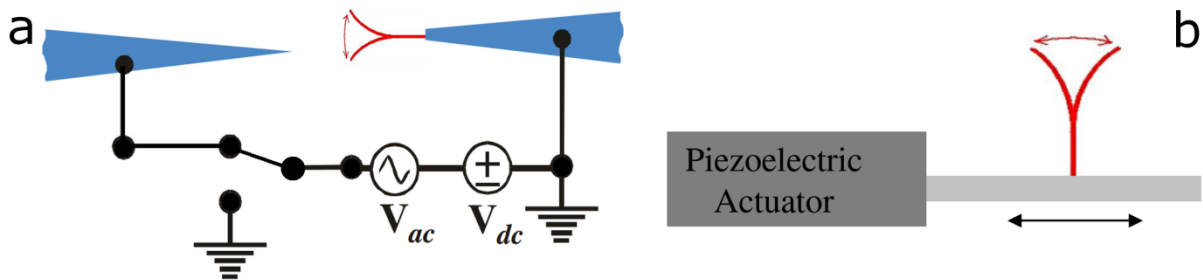


Figure 9. Oscillation of one-end-affixed NW induced by an alternating electric field (a) and a piezoelectric actuator (b).

Let us assume, that the natural resonance frequency of the NW is ν_1 . In the case of electric-field-induced resonance (Fig. 9a) the NW as a cantilever is attached one end to an electrode and the other end is left free. The NW is then driven to vibrate by an electric field between the substrate electrode and a second electrode (counter electrode) positioned near the NW. The electric field contains both direct and alternating components with tunable frequency. The sum of the applied potential and the contact potential (V_{CPD}) between the counter electrode and the NW can be described by the following form:

$$V = (V_{DC} + V_{CPD}) + V_{AC} \cos(2\pi\nu t), \quad (7)$$

where V_{DC} is the direct part, and V_{AC} is the alternating part of the applied electric field having a frequency of ν . The electrostatic force exerted on the NW is essentially entirely at the tip, where the charges are concentrated (as expected from classical electrostatics applied to conducting needle-shaped conductors). The force equals the product of the induced electric charge (proportional to V) and the electric field (also proportional to V). Hence the charge on the tip and the electric field can be assumed to be αV and βV , respectively. α is a NW dependent constant that depends on the geometry. Therefore the electrostatic force at the tip is

$$\begin{aligned}
F(t) &= \alpha\beta V^2 = \alpha\beta[(V_{DC} + V_{CPD}) + V_{AC} \cos(2\pi\nu t)]^2 = \\
&\alpha\beta \left[(V_{DC} + V_{CPD})^2 + \frac{1}{2}V_{AC}^2 + 2(V_{DC} + V_{CPD})V_{AC} \cos(2\pi\nu t) + \frac{1}{2}V_{AC}^2 \cos(2\pi(2\nu)t) \right] = \\
&= F^{(0)} + F^{(1)} \cos(2\pi\nu t) + F^{(2)} \cos(2\pi(2\nu)t). \tag{8}
\end{aligned}$$

The relative position of the NW to the counter electrode can usually be precisely tuned using piezoelectric manipulators. As long as the equilibrium position of the NW is perpendicular to the electrostatic force (off axis position), the vibrational response of the NW as a function of the driving frequency (ν) closely follows the classical behavior predicted by the Euler-Bernoulli model for elastic rods. The appearance of resonances is classically dictated by the Euler equation

$$-EI \frac{\partial^4 U(x,t)}{\partial x^4} + f(x,t) = \rho A \frac{\partial^2 U(x,t)}{\partial t^2}, \tag{9}$$

where $U(x,t)$ is the time dependent deflection from the equilibrium axis at position x along the NW, E is the Young's modulus, ρA is the mass per unit length, I is the second moment of inertia, and $f(x,t)$ is the externally applied force. If the applied frequency matches the natural resonance frequency of the NW, resonance occurs. This is the case of forced resonance. Note that the first and the second harmonic of $F(t)$ could both drive the NW to resonate independently (Eq. 8), therefore $\nu = \nu_1$ and $\nu = \frac{\nu_1}{2}$ are two possible resonant frequencies [43]. If the longitudinal axis of the non-excited NW is parallel to the electrostatic force (in axis position) parametric resonances can be induced due to the instability leading to oscillations at possible frequencies of $\nu = \frac{2\nu_1}{n}, n = 1, 2, 3, \dots$ [43]. However, Shi *et al.* have shown experimentally and theoretically that in the case of sinusoidal wave excitation only the first two parametric resonances can be found [43]. For a randomly oriented NW the vibration becomes complicated because both the transverse and the axial forces are effective, and hence

forced and parametric resonances would be mixed [43]. Nevertheless, one chooses whatever arrangement, it has to be ensured that the natural frequency of the NW is not overestimated as twice the true value or underestimated as half the true value by sweeping a wide frequency range.

The method was first applied by Poncharal *et al.* [44] in order to characterize the mechanical properties of multiwalled carbon NTs. The NTs were resonantly excited at the fundamental frequency and higher harmonics as well in a TEM (Fig. 10a-c). The relationship between these frequencies and the elastic bending modulus (BM) (i.e. the Young's modulus measured by bending) of the NT can be described by the following equation resulting from the Euler-Bernoulli analysis [44]

$$\nu_j = \frac{\beta_j^2}{8\pi} \frac{1}{L^2} \sqrt{D^2 - D_i^2} \sqrt{\frac{E_b}{\rho}}, \quad (10)$$

where L is the length, D is the outer diameter, D_i is the inner diameter, E_b is the BM, ρ is the density, and β_j is a constant for the j th harmonic: $\beta_1 = 1.875$, $\beta_2 = 4.694$. They found, that the elastic BM as a function of diameter decreases sharply from about 1 to 0.1 TPa with increasing diameter from 8 to 40 nm. The method has been also applied to a nanobalance for nanoscopic particles in the picogram-to-femtogram mass range. Eq. (10) is widely applied for the evaluation of such resonance experiments, however, in the case of solid NWs the equation becomes simpler due to the disappearance of the inner diameter (D_i). It can be easily admitted, that the BM theoretically equals to the Young's modulus along the longitudinal axis of the NW: during bending the inner part of the NW suffers longitudinal compression while the outer part suffers longitudinal tension. Liu *et al.* [45] applied the electric-field-induced resonance technique to probe the mechanical properties of WO_3 NWs directly grown on tungsten tips inside TEM. The results indicated that the BM is basically constant at diameter larger than 30 nm, while it largely increases with decreasing diameter when diameter becomes smaller than 30 nm. This diameter dependence was attributed to the lower defect density in NWs with smaller diameter, as imaged by *in situ* TEM (Fig. 10h-i). Chen *et al.* [46] experimentally revealed the size dependence of Young's modulus in [0001] oriented ZnO NWs in SEM. They found, that the BM of NWs with diameters smaller than about 120 nm increases dramatically with decreasing diameters, and is significantly higher than that of the larger ones whose modulus tends to that of bulk ZnO. They explained the increase in the modulus by the increase of the surface stiffening effect for the small NW diameter.

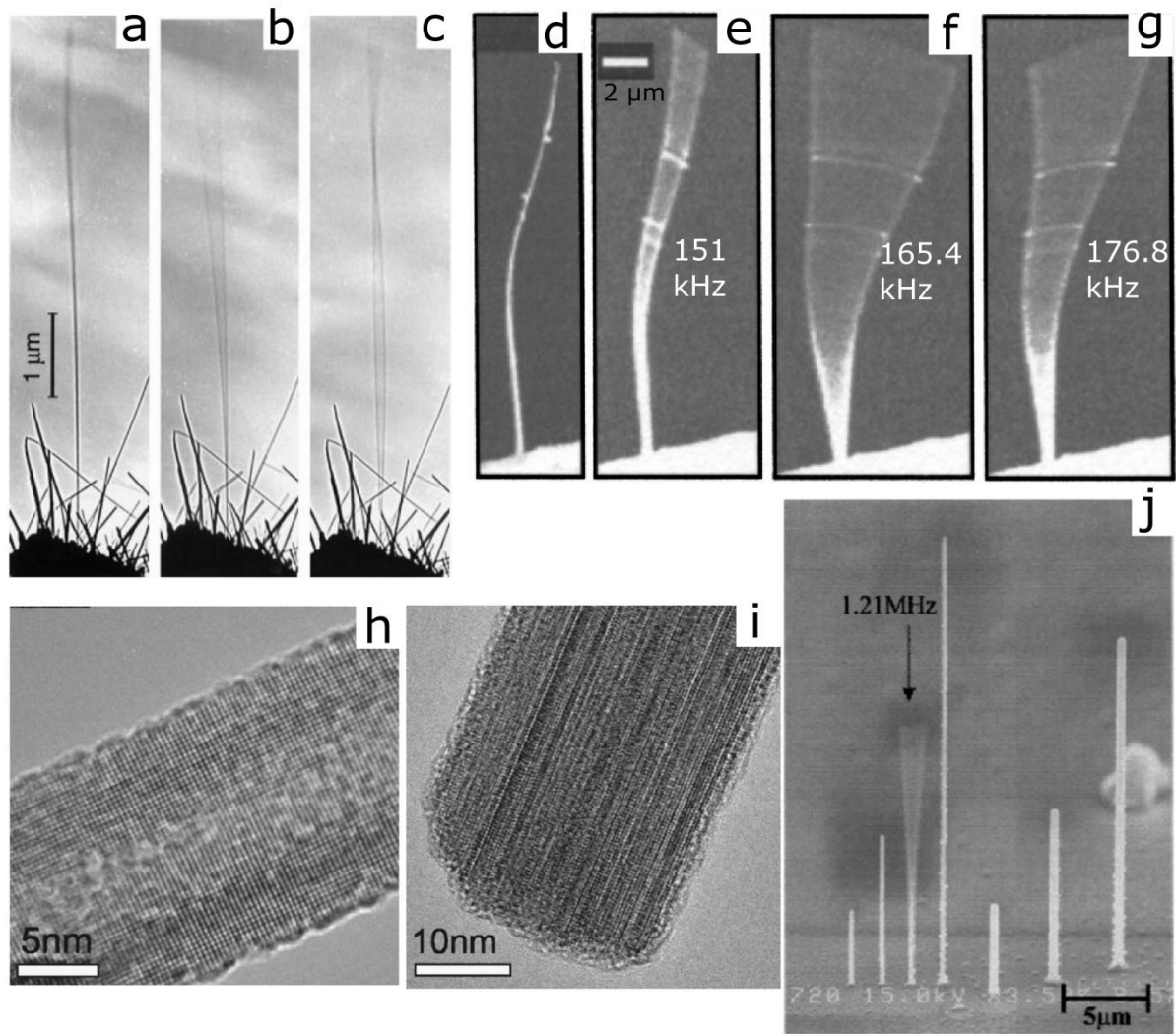


Figure 10. TEM images of multiwalled carbon NT responses to resonant alternating applied potentials: in the absence of a potential (a), excitation of the fundamental mode of vibration (b), resonant excitation of the second harmonic (c) (images a-c adapted from [44]). SEM micrographs of a SiO₂ NW in the absence of excitation (d), and driven mechanically at three closely spaced resonant frequencies as the result of NW anisotropy (e-g) (images d-g adapted from [47]). *In situ* high-resolution TEM (HRTEM) images corresponding to WO₃ NWs with smaller diameter (h), and larger diameter (i) (images h-i adapted from [45]). SEM micrograph showing the oscillations of a diamond-like carbon pillar excited mechanically by a piezoelectric actuator (j) (image j adapted from [48]).

Fujita *et al.* [48] applied a piezoelectric actuator for the mechanical excitation (Fig. 9b) of oscillations in diamond-like carbon (DLC) pillars grown using Ga⁺ focused ion beam-induced CVD with a precursor of phenanthrene vapor in SEM (Fig. 10j). They found, that there is a balance between the DLC growth rate and surface bombardment by the ions, and this played an important role in the stiffness of the pillars. Some of the DLC pillars showed a very large Young's modulus over 600 GPa. Dikin *et al.* [47] investigated the mechanical resonance of

amorphous SiO₂ NWs in SEM induced by both electrical and mechanical excitations. The NWs were held by an electrode fixed at the end of a piezodriver which was responsible for the mechanical excitation, and a counterelectrode was used to electrically excite oscillations. For some NWs they observed up to three closely spaced resonances that are a result of the NW anisotropy (Fig. 10d-g).

1.3.2. Mechanical characterization via axial loading

Similar to the case of macroscopic prismatic objects, the mechanical properties of NWs/NRs/NTs can be examined by applying an axial load on the double clamped nanostructures. However, in the nanorange these experiments are usually carried out in an electron microscope. The axial load can be performed by clamping the nanostructures in between two AFM cantilever tips and subjecting them to tension or compression loads, or a microelectromechanical system (MEMS) can be used as test platform for the mechanical characterization. The main advantage of these methods is that they are not restricted to the elastic properties, however, they require significant amount of specimen preparation time.

Yu *et al.* examined the tensile properties of multiwalled carbon NTs in SEM using a special “nanostressing stage” [49]. The NTs were clamped between two opposing AFM cantilever tips by using electron beam-induced deposition. The stiffer tip was actuated by a picomotor which was responsible for the application of the tensile load, and the softer tip was bent from the tensile load applied to the NT linked between the tips. By recording the whole tensile loading experiment, both the deflection of the soft cantilever (the force applied on the NT) and the length change of the NT were simultaneously obtained. The NTs broke in the outermost layer, and the tensile strength of this layer ranged from 11 to 63 GPa. Analysis of the stress-strain curves for individual NTs indicated that the Young's modulus of the outermost layer varied from 270 to 950 GPa. Lin *et al.* carried out the mechanical characterization of boron NWs in practically the same arrangement, however, they applied buckling load instead of tensile [50] and a nanomanipulator was responsible for the actuation. The Young's modulus of the boron NWs was measured to be 117 GPa. Xu *et al.* studied the elastic and failure properties of single ZnO NWs along the polar direction [0001] by *in situ* SEM tension (Fig. 11a-b) and buckling tests (Fig. 11c-e) [51]. Both tension and buckling were carried out on NWs welded between an AFM cantilever mounted on the SEM stage and a nanomanipulator tip. Deformation was achieved by moving the manipulator towards or away from the AFM probe. Both tensile modulus (from tension) and BM (from buckling) were

found to increase as the NW diameter decreased from 80 to 20 nm. The BM increased more rapidly than the tensile modulus, which demonstrates that the elasticity size effects in ZnO NWs are mainly due to surface stiffening. The tension experiments also showed that the fracture strain and strength of ZnO NWs increased as the NW diameter decreased.

Zhu *et al.* performed tension tests on NWs by locating a MEMS-based material testing stage inside SEM and TEM (Fig. 11f) [52]. Hence the deformation mechanism of NWs under tensile loading could be *in situ* examined. The testing system consists of an actuator and an independent load sensor fabricated by means of surface micromachining. The tensile load was measured electronically by a capacitive sensor. The NWs to be studied were clamped on the test bed by electron beam-induced deposition. Prior to the welding the fine positioning of the NWs onto the test stage was achieved by a nanomanipulator. NW elongation was obtained by measuring the gap between the actuator and the load sensor. As an example they examined the mechanical properties of polycrystalline Pd NWs and the Young's modulus was 20–30% lower than that of a bulk polycrystalline Pd, which was explained by grain boundary relaxation and creep. Another feature revealed by the test is that the yield stress of the NWs was much higher than that of nanocrystalline Pd in bulk form. This phenomenon was attributed to the lowered defect density in nanoscale. Naraghi *et al.* developed a MEMS test platform with off-chip actuation for mechanical characterization of polymeric nanofibers in ambient conditions under optical microscope [53]. Engineering stresses and strains were obtained directly from images of the MEMS platform, by extracting the relative rigid body displacements of the device components by digital image correlation. The accuracy in determining displacements by this optical method was shown to be better than 50 nm. This technique enables the mechanical characterization of NWs composed of electron beam sensitive materials. E.g. physical aging and cross-linking in polymeric fibers subjected to the SEM electron beam do not permit its use. In the application of this method, the mechanical behavior of electrospun polyacrylonitrile nanofibers with diameters ranging from 300 to 600 nm was investigated. The stress-strain curves demonstrated an apparent elastic-perfectly plastic behavior with elastic modulus of 7.6 GPa and large irreversible strains that exceeded 220 %. They improved the MEMS test platform using on-chip actuation and the results on polyacrylonitrile nanofibers agreed well with off-chip measurements (Fig. 11g-h) [54].

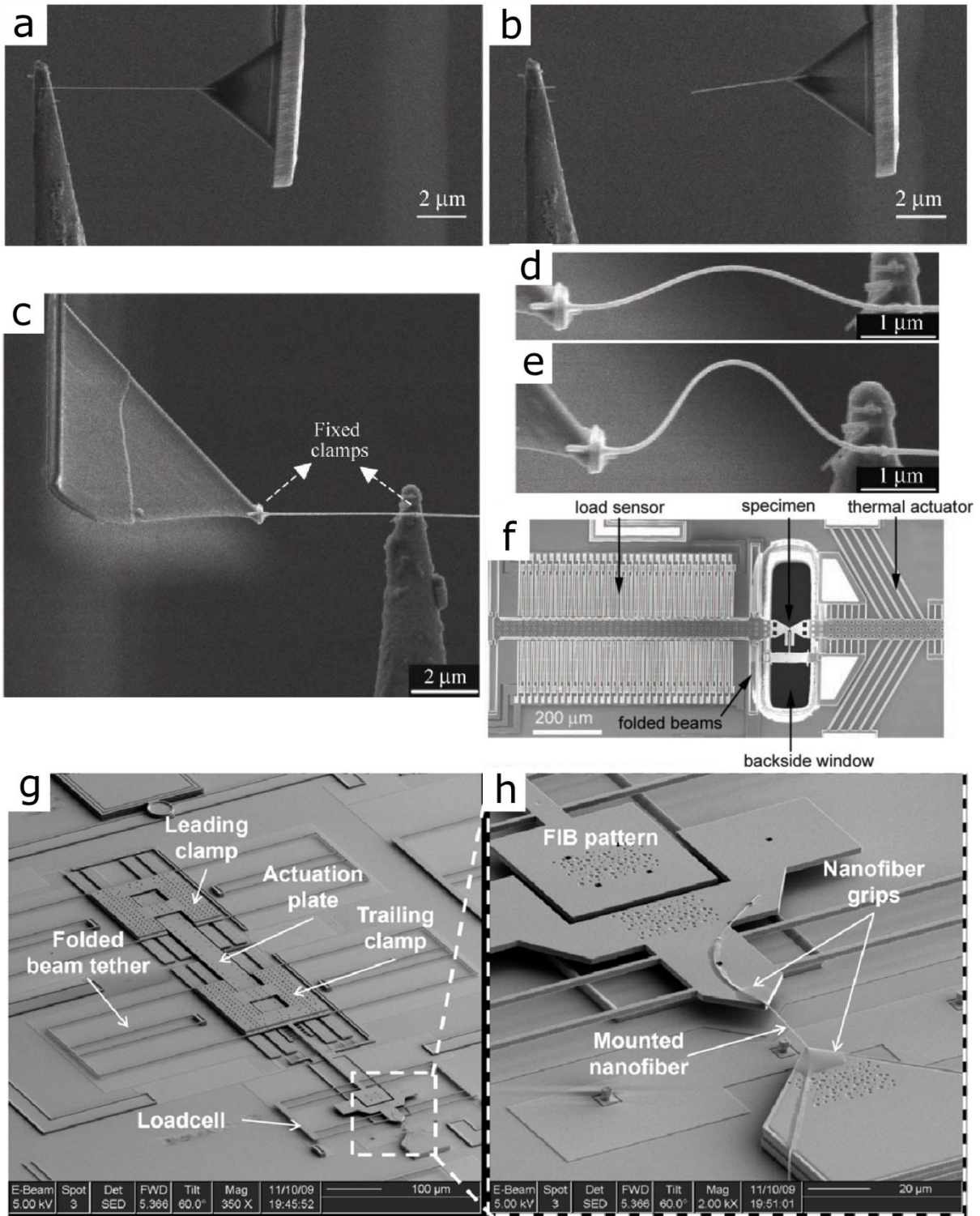


Figure 11. SEM images taken during the tensile test of a ZnO NW with diameter of 20 nm (a-b). Fracture occurs on the NW when the applied load reaches a certain value (fracture load) (b). SEM images showing the buckling test of a ZnO NW with diameter of 46 nm (c-e) (images a-e adapted from [51]). *In situ* SEM and TEM tensile testing device including actuator, load sensor, and specimen (f) (image f adapted from [52]). SEM images of the on-chip actuated MEMS platform for nanomechanical experiments under ambient conditions (g-h) (images g-h adapted from [54]).

1.3.3. Atomic force microscopy based methods

AFM is also a promising tool for the mechanical investigation of NWs/NRs/NTs, since cantilever deflections and torsions and hence normal and lateral forces (NFs and LFs) acting on the tip are precisely monitored by the position sensitive photo detector (PSPD). Therefore AFM is capable of applying and detecting NFs and LFs in nano-Newton range. Similarly to axial loading AFM based methods are not restricted to the elastic properties. Bending can be performed by applying NFs or LFs on the individual nanostructures by the tip of the AFM cantilever. Due to the finite radius of curvature of the tip bending by NFs can be performed only in the case of NWs with diameters significantly higher than the dimensions of the tip. Otherwise the tip would slip off from the NW to be measured. From this aspect, the application of LFs seems more general-purpose, however, the main weak point of the latter is that the lateral output of the PSPD has to be well calibrated in order to obtain fair results. In the usually applied indirect calibration methods many error sources exist, therefore the elastic parameters in the literature have to be carefully handled.

Wong *et al.* used the AFM to determine the mechanical properties of individual horizontal SiC NRs and multiwalled carbon NTs pinned at one end to the surface of the substrate by exerting lateral loads by the tip of the AFM cantilever [55]. The bending force was measured versus displacement along the unpinned lengths. The carbon NTs were about two times as stiff as the SiC NRs. Continued bending of the SiC NRs ultimately led to fracture, whereas the NTs exhibited an interesting elastic buckling process. The strengths of the SiC NRs were substantially greater than those found previously for larger SiC structures, and approached theoretical values.

Paulo *et al.* examined the mechanical elasticity of Si NWs [56], which were grown horizontally between the two facing Si(111) sidewalls of microtrenches prefabricated on a Si(110) substrate, resulting in suspended single and double clamped nanowire-in-trench structures. The deflection of the NWs was induced and measured by the controlled application of NFs with the AFM tip. The agreement between the NW deflection measurements and the theoretical behavior of single and double clamped elastic beams demonstrated the overall elastic beamlike behavior. Ni *et al.* performed nanoscale three-point bending tests directly on individual horizontal amorphous SiO₂ NWs bridging a trench by exerting normal loads with the AFM tip (Fig. 12a) [57]. The NWs were double clamped by electron beam-induced deposition. Elastic modulus of the amorphous SiO₂ NWs was measured to be 76.6 GPa,

which is close to the reported value of the bulk SiO₂. The NWs exhibited brittle fracture failure in bending.

Wu *et al.* studied the mechanical behavior of double clamped Au NWs of different diameters [58]. The horizontal NWs were bridging a trench, similarly to the above methods, however, they applied lateral loads instead of a normal indentation (Fig. 12b, f-g). They found that the Young's modulus is essentially independent of diameter and very close to the bulk value, whereas the yield strength is largest for the smallest diameter wires, with strengths up to 100 times that of bulk materials, and substantially larger than that reported for bulk nanocrystalline metals. Wen *et al.* performed controlled LF AFM measurement of the mechanical properties of double clamped ZnO NWs in the same arrangement [59]. They have demonstrated that contrary to most of the reports the Young's modulus is diameter independent and close to the bulk value down to diameters of 18 nm. The tensile strength of these materials increased for small diameter wires approaching values of 7.00 GPa, which is consistent with reduced levels of defect incorporation as the materials dimensions are reduced. The latter measurement was also carried out *in situ* inside a SEM by Celik *et al.* [60]. They incorporated a customized AFM into the vacuum chamber of the SEM in order to establish the visibility of bending and breaking Ni NWs (Fig. 12c-e). Experimental results revealed that Ni NWs have significantly higher yield strengths than their bulk counterparts, although their elastic modulus values are comparable to bulk Ni modulus values.

The experiment carried out by Song *et al.* on perpendicularly standing ZnO NWs is also based on the LF analysis, however, it fundamentally differs from the above detailed methods [21]. The AFM tip was scanning over the surface in contact mode (Fig. 12h), and they acquired simultaneously the topography and LF image of the aligned NWs. The elastic modulus of the individual NWs was derived from the images (Fig. 12i-j). For the [0001] ZnO NWs/NRs grown on a sapphire surface with an average diameter of 45 nm, the elastic modulus was measured to be 29 GPa.

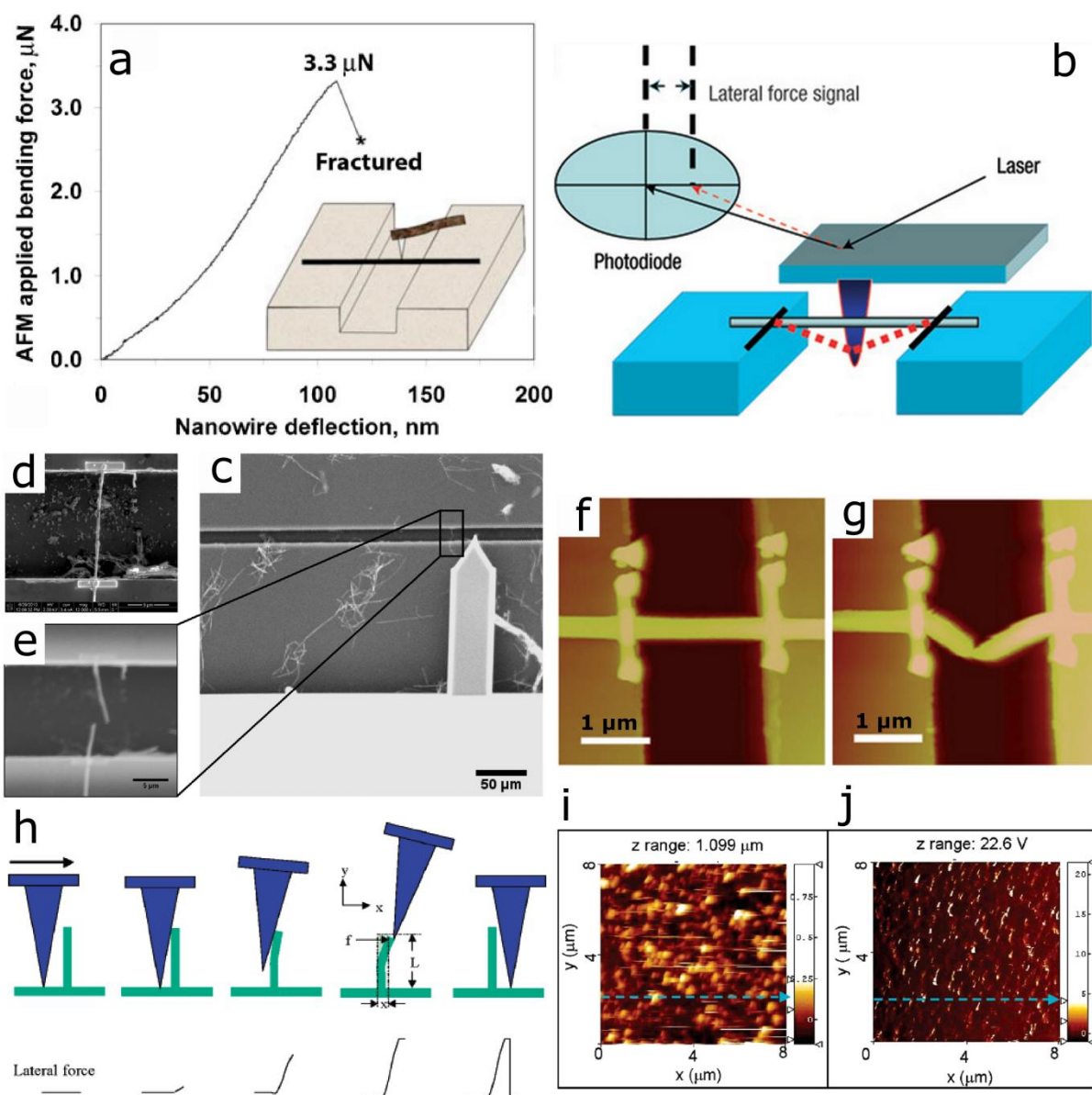


Figure 12. NW deflections obtained on a suspended SiO_2 NW during a nanoscale three-point bending test (a) (image a adapted from [57]). Schematic of a double clamped wire in a lateral bending test with an AFM tip (b). AFM image taken after elastic manipulation of a 200 nm thick Au NW (f) using the method sketched in (b), and AFM image obtained after plastic manipulation (g) (images b and f-g adapted from [58]). SEM micrograph of an AFM cantilever mounted in a customized AFM located in the SEM, which is bending NWs suspended over a trench (c). SEM image of a Ni NW suspended over a trench (d), and the same NW after fracture (e) (images c-e adapted from [60]). Procedures for measuring the elastic modulus of a vertical NW in the AFM contacting mode (h). Topography image (i) and LF image (j) of aligned ZnO NW arrays received in AFM contacting mode. The elastic modulus of each NW in the scanning range can be derived from these images (images h-j adapted from [21]).

1.3.4. Other nanomechanical methods

In the following I briefly discuss a few other methods, which cannot be classified in any of the above techniques.

Li *et al.* measured the hardness and elastic modulus of horizontal Ag NWs lying on a glass substrate by applying a nanoindenter [61]. The indenter tip was used to image and locate the Ag NWs and then *in situ* indent them with the same tip. The indentation impression was also imaged with the same tip (Fig. 13e). Post-test imaging provided the ability to verify that the test was performed in the anticipated location, which maximizes the reliability of the data. The hardness and elastic modulus were calculated from the load-displacement curve. It was found that the Ag NWs have comparable hardness and elastic modulus to bulk Ag.

A nanomanipulator arm equipped with an AFM cantilever offers a perfect tool to carry out static bending tests on one-end-affixed NWs/NRs/NTs *in situ* inside a SEM. Hoffmann *et al.* manipulated individual vertical ZnO NWs with a calibrated AFM tip mounted on a nanomanipulator arm [62]. The substrate with the NWs was mounted on a piezo stack. The coarse positioning of the AFM tip toward the sample was done with the robotic arm and the fine positioning, as well as the manipulation of the NWs, was achieved by moving the sample with the piezo stack. They carried out static bending (Fig. 13a-c) and tensile experiments. Hence the displacements of the AFM probe corresponded to the bending and tensile forces. The fracture strain in the bending test was found to be of 7.7 % and revealed a strength about twice as high as in the tensile test. From the tensile experiments, the Young's modulus could be measured to be within 30% of that of bulk ZnO. Manoharan *et al.* applied bending loads on one-end-affixed ZnO NWs using a tipless AFM cantilever with known spring constant mounted on a manipulator to determine the Young's modulus (Fig. 13d) [63]. The NWs were oriented perpendicular to the edge of a silicon wafer and glued at the end near the edge of the wafer by focused ion beam-induced Pt deposition. Young's modulus was measured to be about 30% of the modulus value at the bulk scale.

Marszalek *et al.* formed Au NW columns by pressing a gold-coated AFM tip against a gold-coated coverslip [64]. The NW could be compressed by a few nanometers and then stretched back by moving a piezoelectric actuator that pushed or pulled the NW against the AFM cantilever (Fig. 13f). During these cycles, the forces applied to the NW were measured and its length was also monitored. NWs elongated and shortened under force in quantized steps. The

results were explained by the sliding of crystal planes within the Au NWs creating stacking faults that change the local structure from face-centered cubic to hexagonal close packed.

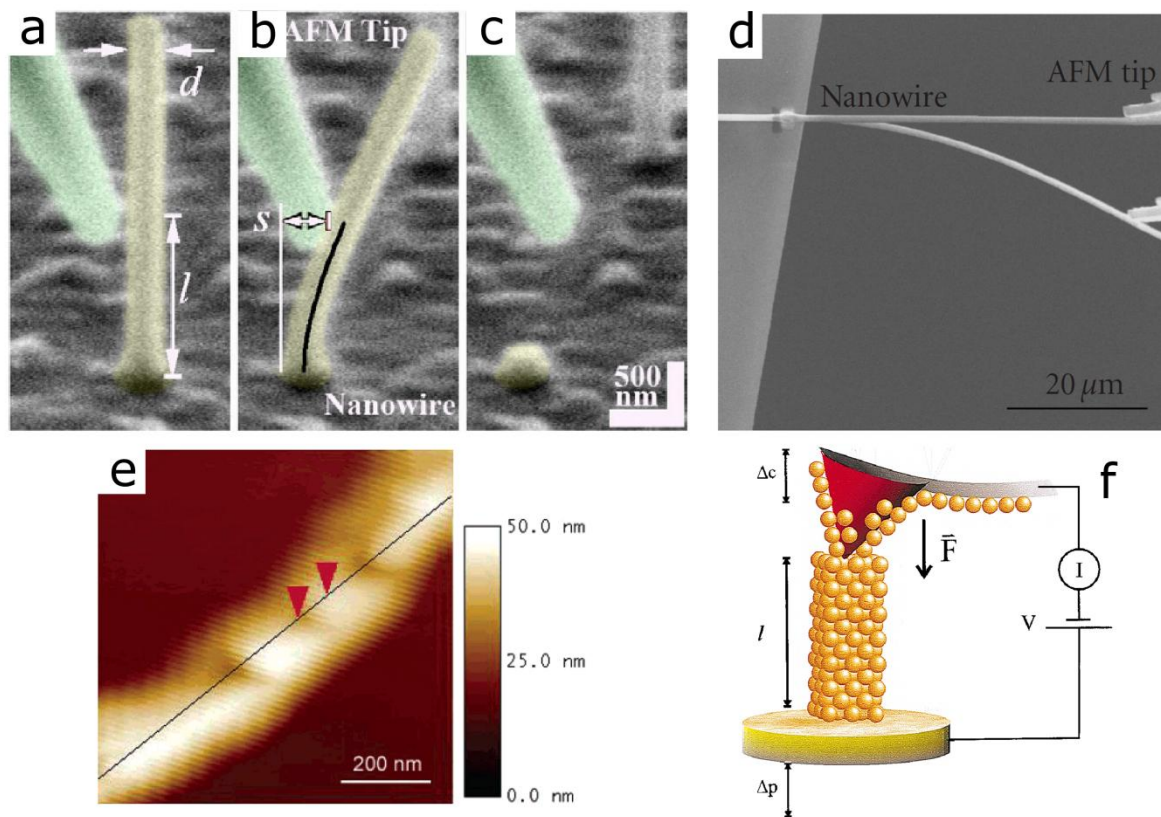


Figure 13. SEM micrographs showing a sequence of an *in situ* bending experiment performed on a vertical ZnO NW: images recorded before any deformation (a), right before fracture (b), and after fracture (c) (images a-c adapted from [62]). Superimposed SEM images from the *in situ* bending of a ZnO NW showing the specimen and only the edge of the loading cantilever (d) (image d adapted from [63]). AFM image of indents on a silver NW (e) (image e adapted from [61]). Schematic of the experimental set-up used to capture quantized plastic deformation in gold NWs (f) (image f adapted from [64]).

Table 2 summarizes the experimentally determined Young's modulus/bending modulus values of NWs/NRs/NTs of different materials with the bulk values for comparison. The data are adapted from the papers introduced in subsections 1.3.1., 1.3.2., 1.3.3., and 1.3.4.

Material	Method	Ref.	NW/NR/NT Young's modulus/Bending modulus [GPa]	Bulk Young's modulus [GPa]
multiwalled carbon NTs	resonance analysis	[44]	100-1000	1060 (graphite, parallel to the basal plane)
crystalline WO ₃ NWs	resonance analysis	[45]	105-313	300
crystalline ZnO NWs	resonance analysis	[46]	135-221	140
diamond-like carbon pillars	resonance analysis	[48]	~100, >600	-
amorphous SiO ₂ NWs	resonance analysis	[47]	47	72 (fused silicon oxide fibers)
multiwalled carbon NTs	axial loading	[49]	270-950	1060 (graphite, parallel to the basal plane)
crystalline B NWs	axial loading	[50]	117	380-400
crystalline ZnO NWs	axial loading	[51]	~135-170 (tensile modulus) ~130-210 (bending modulus)	140
polycrystalline Pd NWs	axial loading	[52]	99	132 (polycrystalline Pd)
polyacrylonitrile nanofibers	axial loading	[53]	7.6	-
SiC NRs	lateral force analysis by AFM	[55]	610-660	600
multiwalled carbon NTs	lateral force analysis by AFM	[55]	1280	1060 (graphite, parallel to the basal plane)
crystalline Si NWs	normal force analysis by AFM	[56]	186	169
amorphous SiO ₂ NWs	normal force analysis by AFM	[57]	76.6	73 (thermally grown SiO ₂ thin film)
polycrystalline Au NWs	lateral force analysis by AFM	[58]	70	78
crystalline ZnO NWs	lateral force analysis by AFM	[59]	133	140
Ni NWs	lateral force analysis by AFM	[60]	262	190-236
crystalline ZnO NWs	lateral force analysis by AFM	[21]	29	140
polycrystalline Ag NWs	nanoindenter	[61]	88	144 (polycrystalline Ag)
crystalline ZnO NWs	nano manipulation in SEM	[62]	97	140
crystalline ZnO NWs	nano manipulation in SEM	[63]	40	140

Table 2. Young's modulus/bending modulus values of NWs/NR/s/NTs composed of different materials and the corresponding bulk modulus values. The nanostructures were mechanically characterized by a number of different methods (also indicated).

1.3.5. Mechanical characterization of ZnO NWs/NRs

In the last few years a considerable effort has been done to investigate the mechanical properties of ZnO NRs and NWs [21, 46, 51, 59, 62-63, 65-70]. This interest is mainly fueled by the appearance of novel ZnO NW based energy harvesting [35, 71] and mechanical sensor devices [32]. The basic mechanical quantities strongly influence the attainable device performance such as output voltage of a nanogenerator [31] or sensitivity of a piezoelectric force sensor [32].

ZnO NRs/NWs crystallize in hexagonal wurtzite (6 mm) form, where the c-axis of the crystal is parallel to the long symmetry axis of the nanocrystal. Although for macroscopic ZnO single crystals all of the five independent elements of the 6 x 6 elasticity matrix are well known for decades [72], the mechanical characterization of nanostructured ZnO is highly challenging and aims to determine only the Young's modulus by using either tensile or bending experiments. The applied techniques include electric-field-induced resonance frequency analysis [46, 65-67], tensile test by using MEMS [68-69], LF analysis with AFM [21, 59], as well as static bending and tensile tests in SEM [51, 62-63, 70]. The obtained results scatter in a surprisingly broad range of 20–200 GPa even though the tensile and bending modulus can be just slightly different (for comparison, the bulk Young's modulus of ZnO in [0001] direction is 140 GPa [72]). Moreover, there is no general consensus how the size effects the mechanical properties of ZnO NRs/NWs. The origin of this strong scattering can be either the large difference in NR/NW quality in the different references or the inaccuracy of the applied characterization methods. The elasticity theory of wurtzite crystals is briefly detailed in Appendix (see subsection 12.1.).

2. Methods

2.1. Two dimensional X-ray diffraction

The fundamental method to study the atomic structure of crystals is diffraction, which can be performed using a beam of electrons, neutrons or high energy photons. In the case of X-ray diffraction (XRD), the scattering occurs on the electron cloud of the atoms, hence the electron density distribution of the observed material can be determined from the diffraction pattern after appropriate evaluation. X-ray powder diffraction is of long standing experimental tool to determine lattice dimensions, orientation, texture, residual stress, crystallite size, percent crystallinity, structure refinement (Rietveld) or identify phase [73]. In two-dimensional XRD a large portion of the diffraction rings can be measured simultaneously, depending on the detector's size and position [74-75]. The detection surface can be a spherical, cylindrical or flat. In the case of flat detector, the sample-to-detector distance can be tuned making it possible to change the angular coverage. The two-dimensional diffraction pattern contains far more information than a one-dimensional profile collected with the conventional diffractometer. In this work a Bruker AXS, D8 Discover with GADDS type two-dimensional XRD was used to study the crystallographic relationship between wet chemically grown ZnO NWs and the corresponding ZnO seed layer.

2.2. Transmission electron microscopy

Transmission electron microscopy (TEM) is among the most powerful materials characterization methods due to its high lateral spatial resolution (with aberration correction 0.05 nm). Two basic modes can be distinguished in TEM according to the role of the post-specimen lenses: they can magnify either the diffraction pattern from the sample produced at the back focal plane of the objective lens; or they can magnify the image produced at the image plane of the objective lens. The selected-area aperture in the image plane of the objective lens can be used to limit the diffracting volume of the specimen and hence the so called selected area electron diffraction (SAED) pattern is obtained. The SAED pattern is a superposition of diffraction patterns from crystallites in the illuminated area that possess distinct orientations. The three primary image modes that are used in conventional TEM work are bright-field microscopy (BF), dark-field microscopy (DF), and high-resolution electron microscopy (HRTEM). Since the electron beam interacts readily with the sample, TEM

specimens are required to be at most 200 nm thick. Probably the most important aspect of the TEM technique is the preparation of high-quality thin foils for observation, which carry the characteristics of the specimen to be observed. Besides the common sample preparation methods, nowadays the so called focused ion beam (FIB) lift-out technique becomes more and more important [76]. The latter makes possible to localize the area on the surface of the sample to be thinned with micrometer accuracy, and cut and lift out a thin piece of cross-sectional or plan-view lamella using FIB and nanomanipulator. The lamella is glued on the TEM grid *in situ* inside the FIB chamber afterwards. In this work two, a JEOL JEM-3010 and a Phillips CM20 type, TEMs were applied to study the crystal structure of the different NWs. The InAs NWs were removed from their original substrate and dispersed on a TEM grid, while in the case of ZnO NWs a cross-sectional TEM lamella was prepared by the FIB lift-out technique.

2.3. Field emission scanning electron microscopy

In scanning electron microscopy (SEM) the sample is scanned with a beam of focused electrons in a raster fashion, and various signals are detected, which are produced due to the interaction between the electrons and the atoms of the sample. The primary beam electrons lose energy by repeated random scattering and capture within a teardrop-shaped volume (interaction volume), which may extend from less than 100 nm to around 5 μm into the surface depending on the energy of the electron beam, the atomic number and the density of the specimen. The detected signals, which contain information about the surface topography and composition, are combined with the position of the beam to produce different images. The electron gun can be thermionic, but improved spatial resolution and minimized sample damage can be achieved using field emission cathode utilized in so called field emission scanning electron microscopy (FE-SEM) [77]. Monitoring of low energy (<50 eV) secondary electrons and high energy back-scattered electrons are the most common imaging modes in SEM. Since the energy of secondary electrons is low, they can escape the sample within a few nanometers from the surface, and therefore the secondary electron image is especially sensitive to the change of the surface morphology. In this work a Zeiss 1540XB type FE-SEM was applied in secondary electron imaging mode to examine the geometry of the synthesized NWs/NRs and to visualize the nanomechanical experiments carried out *in situ* inside the SEM chamber.

2.4. Focused ion beam etching

In the Zeiss 1540XB FE-SEM system a focused ion beam (FIB) column is also incorporated. The beam of focused Ga⁺ ions is suitable for ablation or deposition of materials. The typical accelerating voltages and currents of the Ga⁺ ions in our system are 3-30 kV and 1pA-50nA, respectively. During milling the primary ion beam hits the sample surface and sputters a small amount of material, which leaves the surface as either secondary ions or neutral atoms. The primary beam also produces secondary electrons. At higher primary currents, a great deal of material can be removed by sputtering, allowing precision milling of the specimen down to a sub micrometer or even a nano scale. The area to be milled can be localized with high accuracy on the sample surface by the high resolution FE-SEM. In this work FIB was used to prepare a cross-sectional TEM lamella and to customize the tip of the AFM probes applied *in situ* inside the SEM to bend the NWs.

2.5. Electron-beam lithography

Electron-beam lithography is the practice of scanning a focused beam of electrons to draw custom shapes on a surface covered with an electron sensitive resist. The electron beam changes the solubility of the resist enabling selective removal of either the exposed (positive resist) or non-exposed (negative resist) regions of the resist by immersing it in a developer solvent. In this work a JEOL IC 848-2 type SEM together with an Elphy Quantum Elphy 3.0 electron beam controller hardware/software was used to define cylindrical nucleation windows in the resist for NW growth. In case of typical resist material (PMMA, 300 nm) and low beam current (4 pA) the attainable smallest feature size is ca. 60-100 nm, while the minimal distance between two objects is in the 150-200 nm range.

2.6. Nanomanipulation inside the SEM

Development of micro- and nano-manipulation has enabled researchers to simultaneously image and manipulate small objects in SEM and TEM. Micro- and nano-manipulation deal with handling of extremely small objects on the order of 10⁻⁴ to 10⁻⁹ m. Piezoelectric stick-slip actuators can be considered as the foundation of modern micro- and nano-manipulation due to their benefits, such as simple structure, high positional accuracy, unlimited movable distance, and high stability as they are supported by guiding surfaces. Fig. 14a shows the schematic of these actuators. They are built up from a piezoelectric element and a sliding mass that moves

relative to the former. Fig. 14b shows the typical saw-tooth voltage usually applied to the piezoelectric element. It consists of two parts. In the so called stick phase the voltage slowly increases from 1 to 2, leading to the extension of the piezoelectric element by a distance D . Due to the so called “stick-slip” friction between the piezoelectric element and the sliding mass, the sliding mass also advances. In the slip phase the voltage is quickly reduced from 2 to 3, and therefore the piezoelectric element quickly shrinks. However, the inertia of the sliding mass prohibits it from moving backward as quickly, which leads to a net forward displacement of the sliding mass by a distance of $d < D$. This technique enables nanoscale precision combined with a wide range of motion *in situ* inside the electron microscope [78].

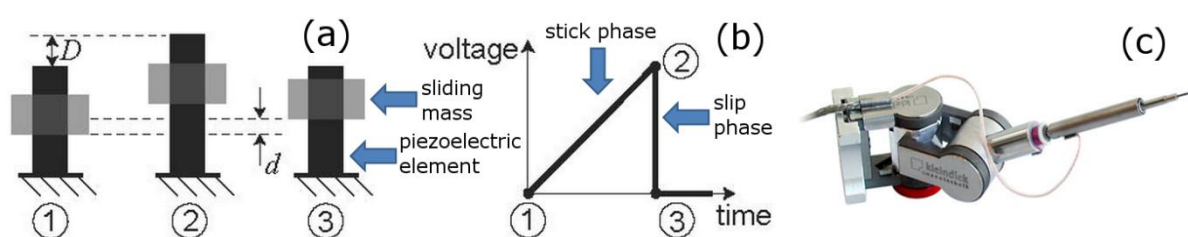


Figure 14. Schematic of the piezoelectric stick-slip actuator which is composed of a piezoelectric element and a sliding mass that moves relative to the piezoelectric element (a). Saw-tooth voltage applied to the piezoelectric element (b) (images a-b adapted from [78]). The Kleindiek MM3A-EM nanomanipulator arm (c).

The Kleindiek MM3A-EM nanomanipulator arms used in this work (Fig. 14c) are composed of three piezoelectric stick-slip motors. The resolution of the left-right and up-down movement is 5 nm, while that of the in-out movement is 0.5 nm [79]. The robotic arms were applied to carry out *in situ* nanomechanical tests on the individual NWs inside the SEM chamber. The nanomanipulator was essential during the FIB lift-out TEM lamella preparation as well.

2.7. Atomic force microscopy

The invention of the atomic force microscope (AFM) [80] was mainly fueled by the fact, that the scanning tunneling microscope (STM) enables only the investigation of conducting materials, therefore other physical processes had to be found to map surfaces. In our AIST-NT SmartSPM 1010 type atomic force microscope (AFM) besides the common imaging modes (contact mode, tapping mode) a series of physical processes can be applied for image formation. One specific imaging mode is the so called piezoresponse force microscopy (PFM) [81], where a conducting AFM probe scans the surface of a ferroelectric or piezoelectric material in contact, and an oscillating voltage is applied to the tip. Due to the alternating

electric field and the electromechanical behavior of the specimen, small out-of-plane and in-plane vibrations are induced in the material. These oscillations are detected using lock-in technique as the first harmonic component of the tip deflection and torsion. The phase of the electromechanical response of the surface yields information on the polarization direction below the probe. In this work AFM was applied to examine the surface topography and roughness of different ZnO seed layers in tapping mode and to study the inverse piezoelectric effect on vertical ZnO nanopillars. The electromechanical study of a 1D proof-of-concept (PoC) device was also carried out in the AFM.

2.8. Finite element method

In this work numerical calculations carried out by COMSOL Multiphysics (version 4.2a) were applied to determine the piezoelectric potential, mechanical stress, and mechanical strain distributions in complex geometries. COMSOL was also applied to calculate the Young's modulus of InAs NWs. COMSOL is a finite element method (FEM) modeling tool. The FEM analysis is composed of several steps as follows. At first the complex geometries are divided into discrete portions (i.e. finite elements) that are connected by nodes. Therefore a structured grid is obtained, which is usually called a mesh. Then equations of equilibrium are applied to each element resulting in the construction of a system of simultaneous equations. The equations take into the account the applicable physical considerations such as compatibility and constitutive relations. Finally the system of equations is solved for unknown values using the techniques of partial differential equations.

Findings

3. Design of a novel ZnO nanowire based nanoforce sensor

As we have seen in subsection 1.2.4., the anchored piezoelectric ZnO NW produces an electric potential difference between its tensed and compressed sides in response to applied bending load. Hence, it seems to be a plausible idea to contact the opposite sidewalls of the NW and use this potential difference for pressure sensing. However, this task is technologically extremely difficult, because local metal deposition would be necessary, which is a rather challenging and expensive process e.g. with electron beam induced deposition inside the SEM (EBID). Moreover the metal layer, as equipotential surface, would weaken the piezoelectric signal.

Let us consider a vertical ZnO NW with hexagonal cross-section standing on a ZnO/Si substrate and create a FEM model in COMSOL. For the sake of simplicity let us assume, that there is a Si substrate of 300nm x 300nm x 150 nm beneath the seed layer of 300nm x 200nm x 50nm, where 50 nm is the thickness. The edge of the NW's hexagonal cross-section (a) is 25 nm, while its length is 600 nm. The NW stands perpendicularly in the middle of the ZnO layer, and the c -axis of ZnO in the model is also perpendicular to the substrate, while the long symmetry axis of the hexagonal cross-section corresponds to the $\langle 11\bar{2}0 \rangle$ crystallographic direction. Only the bottom plane of the substrate is anchored. The elastic constants of the compliance matrix and the elements of the piezoelectric tensor for ZnO applied in the model were adapted from [5]. It was also assumed, that there are no free charge carriers, i.e. we have a perfect dielectric material. Fig. 15a shows the COMSOL model of this arrangement with the ideal meshing by triangular elements. Let us now push the NW by a lateral force of 80 nN along the x -axis at the top along the $\langle 11\bar{2}0 \rangle$ crystallographic direction, as depicted by a red arrow in Fig. 15a. According to our simulations the piezoelectric potential difference occurring as the result of a lateral bending takes place not only between the two sides of the NW, but inside the whole depth of the seed layer under the NW as well (Fig. 15d). Moreover, the magnitude of the potential in the layer falls in a one order of magnitude higher range. Similarly, the mechanical stress and strain also penetrate into the ZnO thin film (Fig. 15b-c). The x - z plane cross-sections in Fig. 15b-d include the longitudinal axis of the NW and the vector of the bending load.

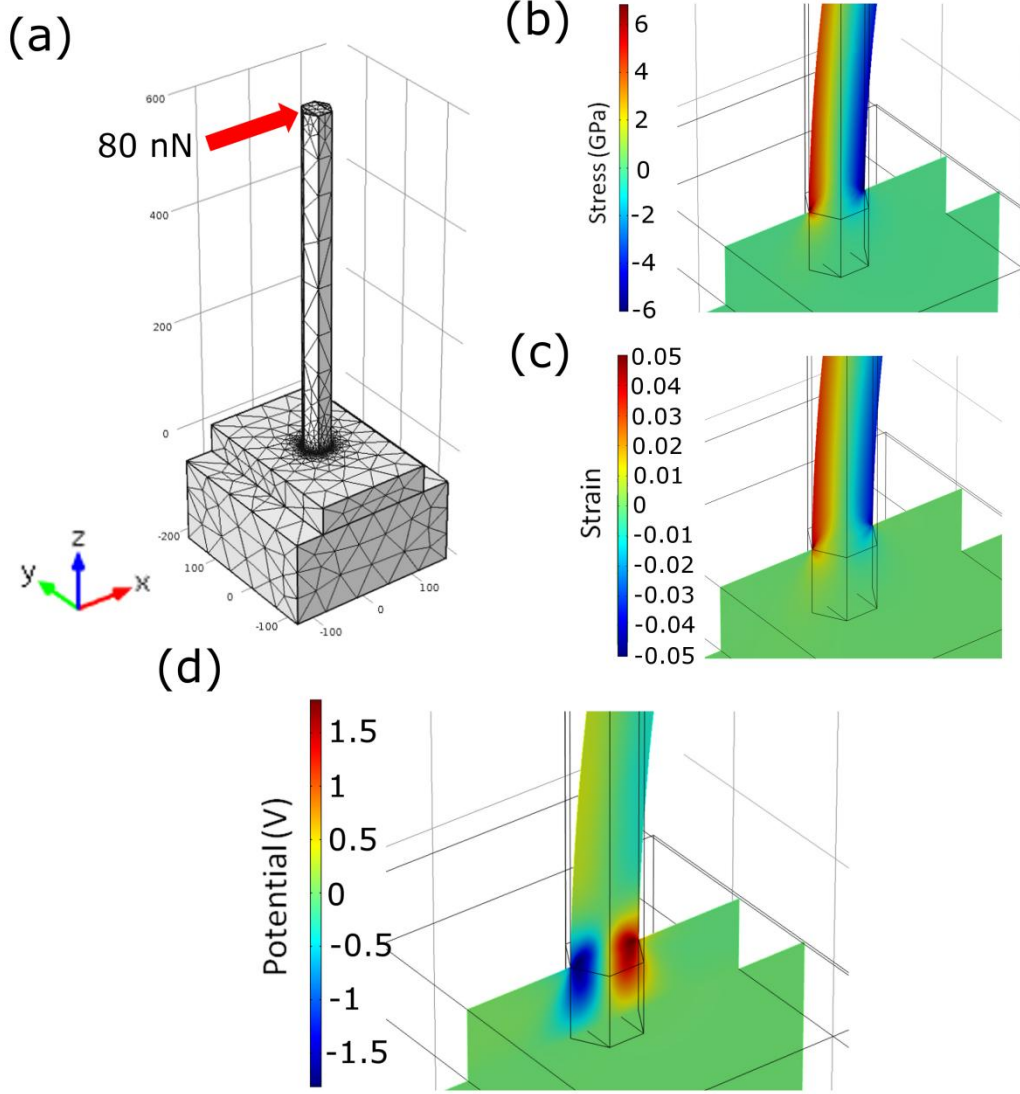


Figure 15. COMSOL model of the NW/seed layer/substrate assembly showing the ideal meshing by triangular elements (a) (parameters: edge of the hexagonal cross-section: 25 nm; NW length: 600 nm; ZnO seed layer thickness: 50 nm). Cross-section of the τ_{zz} component of the mechanical stress (b), the ε_{zz} component of the mechanical strain (c), and the electric potential distribution (d) for the bottom part of the bent NW and the seed layer as the result of finite element calculation (bending force at the top: 80 nN).

Besides piezoelectricity ZnO shows piezoresistivity as well, i.e. the electrical resistivity changes when mechanical stress is applied. The resistivity change ($\Delta\rho_{ij}$) is connected to stress (τ_{kl}) by a fourth-rank tensor (π_{ijkl}), the piezoresistance tensor

$$\frac{\Delta\rho_{ij}}{\rho_{ij}} = \sum_{kl} \pi_{ijkl} \tau_{kl}, \quad (11)$$

where ρ_{ij} is the relaxed resistivity. Here τ_{kl} represents a force applied in the k direction to a unit area of the plane whose outward-drawn normal lies in the l direction. Generally the

resistivity (and hence the resistivity change) is also a rank-2 tensor, since for anisotropic materials the current may not flow in exactly the same direction as the electric field.

In the case of piezoresistivity the mechanism of ZnO layer resistance modulation is obvious, however, the piezoelectric phenomenon needs a little explanation. When a ZnO crystal is elastically deformed, a piezoelectric potential field is created. The piezoelectric potential is created by the polarization of ions in the crystal rather than the free-mobile charges. Since the charges associated with the ions are affixed to the atoms, they cannot freely move. Depending on the doping level, a given amount of free carriers also exist in the semiconductor, which may partially screen. However, according to Wang *et al.* [82], they cannot totally cancel out the piezoelectric charges at a moderate carrier density of $\sim 10^{16}$ – 10^{17} cm⁻³. Only in the case of an ideal insulator, in which the density of free carriers is negligible, the internal electric field and the potential are governed by piezopolarization. Only in this ideal case a FEM analysis performed on the NW with the seed layer (Fig. 15d) is valid. Therefore, depending on the chosen thin film deposition method and hence the quality of the ZnO seed reduction in magnitude of the potential is possible.

During the bending of the ZnO NW a change in the resistance of the ZnO layer can be expected due to the gating effect of the piezoelectric potential. This could be detected for instance by cutting a narrow channel (ribbon) from the seed layer above an insulating substrate, on which a single NW stands, and measure the resistance of the channel. The proposed mechanism for the gating, similarly to the case of the NW field effect transistor of Wang *et al.* [32], is the following. When the piezopotential appears inside the seed layer, some free electrons in the n-type ZnO crystal may be trapped at the positive side surface (Fig. 16a) and become non-movable charges, thus lowering the effective carrier density in the channel. On the other hand, even if the positive potential side could be partially neutralized by the trapped electrons, the negative potential remains unchanged. Hence, the piezo-induced electric field is retained across the width of the channel. The free electrons will be repulsed away by the negative potential and leave a charge depletion zone around the negative side (Fig. 16b). Consequently, the width of the conducting channel inside the ZnO seed layer under the NW becomes smaller and smaller while the depletion region becomes larger and larger with the increase of the NW bending. Zhou *et al.* have shown that the conductance of a bent ZnO microwire shows a slow recovery (during permanent mechanical deformation the I-V curve of the ZnO wire was continuously measured by a sweeping voltage from -2 to 2 V applied for more than 14 min) [83]. However, the piezoelectric potential across the wire had a

lifetime of ~ 100 s. This is long enough for effectively gating the transport current inside the ZnO channel thus a piezoelectric field effect transistor is possible based on the piezoelectricity of ZnO. According to Zhou the slow screening process is likely due to the strong trapping effect of the electrons by vacancy/impurity/surface states in ZnO, which results in a slow release of the trapped charge.

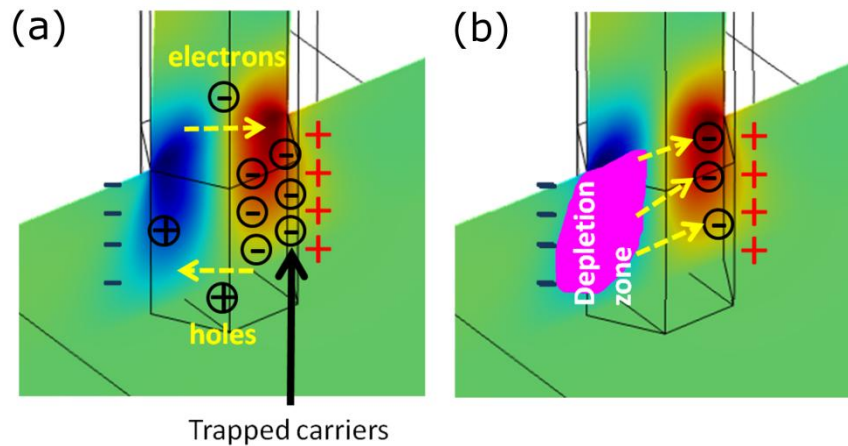


Figure 16. Schematic of the carrier trapping effect (a) and the creation of a charge depletion zone (b) in the ZnO channel cut from the seed layer beneath a bent NW as the result of the coupled piezoelectric and semiconducting dual properties of ZnO. The yellow dashed line in (b) indicates the direction of the electron's repulsion.

Fig. 17 shows the schematic of my proposed device. A highly doped p-type Si wafer with a thermal oxide layer at the top is used as substrate and a field-effect transistor behaving as a capacitor with three ZnO conducting channels in a three pointed star shape between the Ohmic electrodes. The ZnO channels and electrodes are cut from a thin ($d < 50\text{nm}$) ZnO layer deposited onto the insulating oxide by dry etching. A perpendicularly standing ZnO NR is grown on the seed layer at the midpoint, i.e. at the intersection of the three channels. We expect a change of the conductance of the channels with increasing the elastic bending or compressive deformation of the NR by manipulation. It can be presumed that the normal forces could cause both vertical compression and bending of the NR through buckling. The origin of the operation could be either the piezoresistivity or the coupled piezoelectric and semiconducting nature of ZnO, or both as well. Therefore each channel bridging the corresponding ZnO electrodes acts as a field effect transistor in which the source to drain current is controlled by the forces acting on the NR. The role of the highly doped Si gate electrode at the bottom is to set the operating point of the device (back gate). Low-resistance Ohmic contact on either undoped or Al-doped ZnO electrodes can be made by depositing Ti/Au metal layer structures [84-85]. This approach is suitable for the direction dependent

detection of forces by monitoring simultaneously the current in each conducting channel, i.e. it makes 3D sensing in small sizes possible.

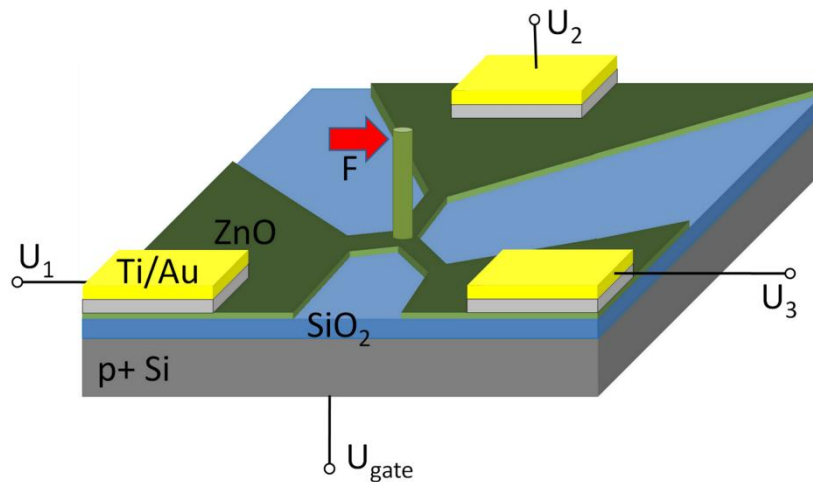


Figure 17. Schematic of the proposed integrated device for the direction dependent detection of forces in the nanorange.

The long-range goal of this work, thus, is to utilize the above piezopotential and resistivity change of the seed layer under the NW in an integrated NEMS device for the detection of forces in the nanorange. The idea of the device is mainly fueled by the current modulation in a single ZnO NW achieved by mechanical deformation demonstrated by Wang *et al.* [32] and the integrated piezotronic transistors demonstrated by Wu *et al.* [33] (see subsection 1.2.4.). However, the main advantage of our approach is the low dimensions of the NWs and hence good resolution. Moreover, here top contact for the NW is not needed, which makes the technology simpler and the device more robust. A 3 dimensional force sensor composed of a vertical ZnO wire of submicron size has a variety of potential applications. On the one hand if a ZnO NW formed one pixel of a novel piezoelectric/piezoresistive fingerprint detector, the $50\mu\text{m} \times 50\mu\text{m}$ pixel size of nowadays common capacitive and optical devices could be considerably decreased. Hence detection of higher spatial frequencies of features on the human fingertip could be possible leading to higher security. On the other hand the ZnO NW 3D force sensor offers a perfect tool for different in-vitro or in-vivo biophysical measurements, e.g. detection of cellular traction forces with subcellular resolution. Tan *et al.* applied polymer microrods for the latter purpose, however, in their approach the deflection of the rods and hence the cellular forces were detected optically making in-vivo experiments impossible [86].

In chapters 4, 5, and 6 I explore the following problems to be solved in order to realize a novel ZnO NR based integrated nanoforce sensor: (i) I give evidence of an e-beam lithography process, which enables the preparation of vertical ZnO NR arrays on different substrates and the SEM, XRD, TEM, and PFM characterization of the structures is also discussed (see chapter 4) [T1, T2]; (ii) I describe the validation of an in situ static bending test inside the SEM (see chapter 5) [T3]; (iii) I describe the mechanical characterization of epitaxially grown ZnO NRs using the validated static bending test (see chapter 6) [T4]. Finally, in chapter 7, without striving for completeness I show the first promising results towards the device fabrication (and characterization) and the future perspectives. However, the actual integrated 3D device is beyond the scope of this thesis.

4. Substrate effect on the growth of vertical zinc-oxide nanowires

As it was described previously, vertically aligned ZnO NW and NR arrays are currently attracting a great deal of interest due to a variety of potential applications, ranging from photovoltaics, light emitting devices [87], and piezotronics through to chemical, biological, and gas sensing [88]. As well as their diverse needs in terms of functionalization and device structure, each of these applications has different requirements in terms of nanostructure geometry, spacing, and alignment. For example, Xu *et al.* reported that arrays of NW near UV/blue LEDs showed enhanced electroluminescence when there was better vertical alignment and length uniformity [38]. The same was found to apply for NW “nanogenerator” arrays, in which more highly ordered, more vertically oriented ZnO NWs/NRs gave improved performance [35, 71]. High aspect ratio is found to be important for ZnO NWs used as electrodes in DSSCs [39, 89]. Near-surface light wave manipulation by means of an inverse designed homoepitaxial ZnO NR array [90] and rod type photonic crystal optical line defect waveguides [91] both require very good alignment and precise control of NW/NR dimensions. Wang *et al.*, on the other hand, reported that ZnO NW gas sensors showed excellent response for H₂, NH₃, and CO detection irrespective of the degree of alignment [92].

In the case of the targeted integrated ZnO NR based nanoforce sensor the vertical orientation of an individual NR is essential in order to obtain equal sensitivity in all lateral directions. The latter can be easily proved by the following. Let us consider the COMSOL model of Fig. 15 with a slight change: the NW is tilted by 20° around the short symmetry axis of the hexagonal cross-section (Fig. 18a). The direction of the c-axis is still parallel to the longitudinal axis of the NW, and the seed layer is also in this crystallographic orientation. Let us then assume that the NW is pushed at its free end by a force of 80 nN being parallel to the plane of the sample surface and perpendicular to the axis of NW tilt, as depicted by a red arrow in Fig. 18a. Cross-sectional (x-z) distribution of the piezoelectric potential (Fig. 18b) induced in the seed layer in response to bending shows an obvious asymmetry. The plane of the cross-section includes the longitudinal axis of the NW and the vector of the bending load. If we plot the line profile along the dashed black line of Fig. 18b, this asymmetry is more obvious (Fig. 18d). Namely, the absolute value of the piezopotential maximum is higher while the width of the ‘peak’ is lower on the left side (negative side) than on the right side (positive side). The same is true when the opposite bending load is applied (Fig. 18c and e), however, here the polarity is the

opposite. Therefore it can be presumed that due to this tilt the same load from different lateral directions can lead to electric potential distributions with different features. Without a strong control over the vertical alignment the reproducibility of the device's production will be troublesome, as well as its calibration. It would be also favorable to bend a single NW instead of a bundle of NWs, since in the latter case the prediction of the piezopotential is very challenging.

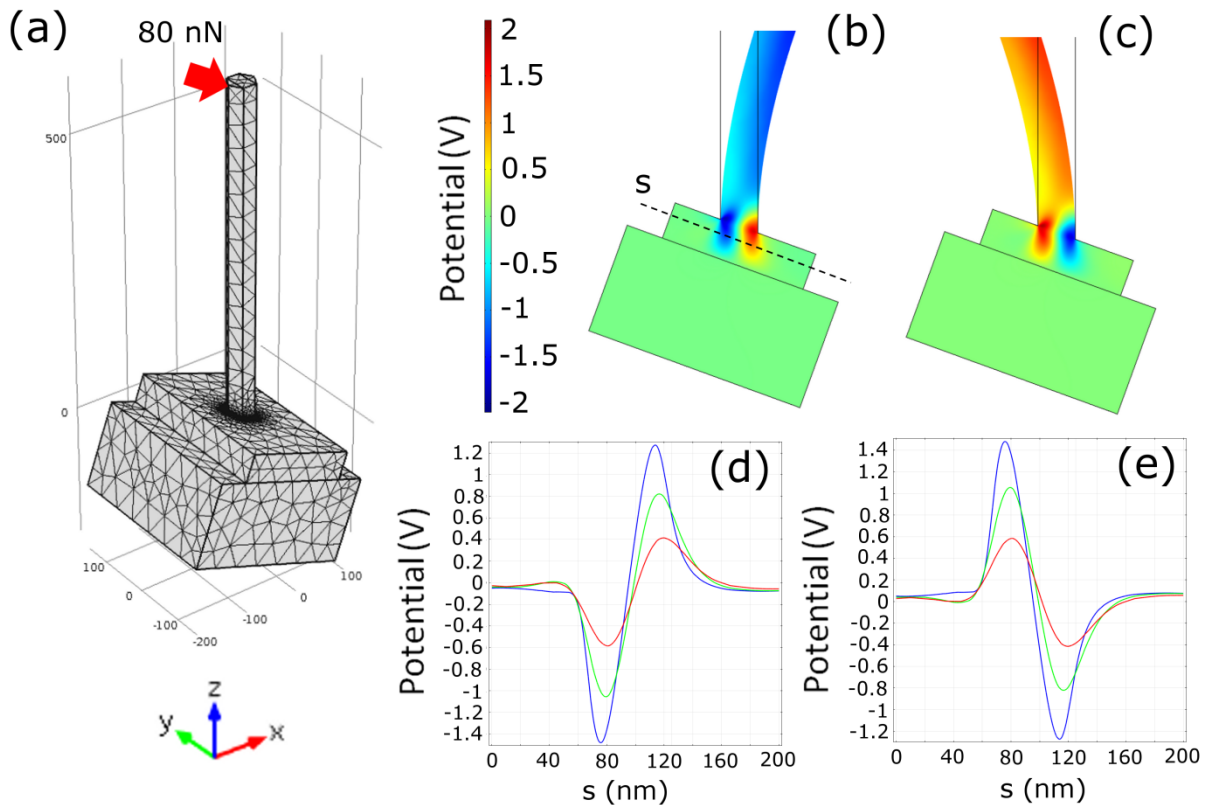


Figure 18. COMSOL model of the tilted NW/seed layer/substrate assembly showing the ideal meshing by triangular elements (a) (parameters: edge of the hexagonal cross-section: 25 nm; NW length: 600 nm; ZnO seed layer thickness: 50 nm; tilt angle: 20°). Cross-section of the electric potential distribution for the bottom part of the bent (and originally tilted) ZnO NW and the seed layer as the result of finite element calculation (b) (bending force at the top: 80 nN). Line profiles along axis-s on (b), where the distance between axis-s and the top surface of the ZnO seed layer is 12.5 nm (blue line), 25 nm (green line), and 37.5 nm (red line) (d). Cross-section of the electric potential distribution when the bending load is the opposite (c). Line profiles of the electric potential distribution in the seed layer when the bending load is the opposite (e). The line colors have the same meaning as in the case of (d).

In previous work, it was demonstrated that regular epitaxial arrays of highly uniform ZnO NRs could be formed homoepitaxially on ZnO single crystals by wet chemical growth [93]. However, for most applications, an alternative substrate material would be preferable to reduce the cost, and to integrate the nanostructure with conventional substrates, e.g. Si,

sapphire, or glass. Heteroepitaxial ZnO NWs can be grown on lattice-matched substrates by several dry deposition methods [37, 94-95]. However, in the case of wet chemical methods, a ZnO seed layer template is required. This seed layer has been found to strongly influence the geometry and orientation of the NRs/NWs which are grown on top [96]. For the purpose of my nanoforce sensor conventional substrates are preferred to integrate it later into a conventional logic circuit. Although CMOS (Complementary Metal–Oxide–Semiconductor) technology in my case is not necessary for signal read-out, it would be also interesting to integrate the NWs with it. If one wants to read out e.g. the piezoelectric charges generated by a single ZnO NW, it is desirable to grow NWs on a CMOS integrated circuit system due to its high noise immunity and low static power consumption. However, since CMOS technology applies cheap Si(100) substrates, the synthesis of vertical ZnO NWs on a CMOS integrated circuit system is not an obvious task.

In this chapter, the effect of the seed layer on the geometry and alignment of patterned vertical ZnO NWs is investigated through a comparative study of seven different types of ZnO seed surfaces. Although patterned growth of ZnO NWs/NRs has already been proposed by several groups on different ZnO seed layers, such as sputtered [97-98], MOCVD [99], colloidal [96], or hydrothermally grown textured [100] thin films, it was not possible to obtain as regular and uniform arrays as those grown on ZnO single crystals [90, 93]. In the following I examine the impact of seed layer with the aim of understanding the factors which influence the regularity and uniformity of the NW arrays.

4.1. Experimental subsection

The first of the seven seed layers was the Zn terminated surface of a c-axis oriented, hydrothermal ZnO single crystal (CrysTec GmbH; denoted as “BULK”). The second ZnO seed layer was an epitaxial ZnO thin film grown by pulsed laser deposition (PLD) on c-sapphire (denoted as “PLD/sapphire”) using a KrF excimer laser (248 nm) [101]. The third ZnO seed layer was ZnO grown by atomic layer deposition (ALD) onto a thick (~6 μ m) epitaxial MOCVD GaN film (TDI Corporation) on c-sapphire (denoted as “ALD/GaN”). The layer was grown with 500 ALD cycles at 300 °C deposition temperature [102]. The fourth ZnO seed layer was ZnO grown by PLD on Si(111) (denoted as “PLD/Si”) [103]. The fifth ZnO seed layer was also deposited by PLD onto Si(100), but this time a 130 nm thick thermal SiO₂ was grown prior to the ZnO growth. This sample was denoted as “PLD/SiO₂/Si” [103]. The sixth ZnO seed layer was again a PLD ZnO on c-sapphire, but here a 100 nm thick highly

textured (111) oriented Pt buffer layer was deposited before the ZnO growth in a DC magnetron sputtering system, as described elsewhere [104]. This sample was denoted as “PLD/Pt/sapphire”. The last seed layer was grown on a Si(100) wafer in Ar/O₂ atmosphere by DC reactive magnetron sputtering of an Al doped (2 wt %) Zn target (denoted as “Sputt/Si”). In order to stabilize the glow discharge, a pulse signal was added to the direct current voltage. The deposition was carried out without bias voltage or substrate preheating [105]. It should be noted that no attempt was made to remove the native amorphous SiO₂ passivation layer on the surface of either the (111) or (100) Si substrates. PLD/sapphire, PLD/SiO₂/Si and PLD/Pt/sapphire were deposited at the National Institute for Materials Science (NIMS) in Japan, ALD/GaN and Sputt/Si were deposited at MTA TTK MFA, and PLD/Si seed layer was made at Nanovation SARL in France.

The process flow for the fabrication of the ZnO NWs is shown in Fig. 19 [90, 93]. First of all each seed surface was washed ultrasonically in acetone, ethanol, and deionized water (Fig. 19a). In order to provide patterned templates for subsequent NW growth, a ~300 nm thick poly(methyl methacrylate) (PMMA) resist layer was spin coated onto each seed surface, and a regular triangular lattice (150 μm x 150 μm, with a lattice constant of 500 nm) of circular growth windows (~120-130 nm in diameter) was then exposed in the PMMA layer by e-beam lithography (Fig. 19b). After development, NW arrays were synthesized using a low temperature wet chemical method (Fig. 19c) based on an aqueous solution having the same concentrations (4 mM) of zinc nitrate hexahydrate (Zn(NO₃)₂·6H₂O) and HMT ((CH₂)₆N₄), as reported elsewhere [23]. During NW growth the solution and the specimens were in a tightly closed glass bottle (Fig. 19f), which was placed into a multipurpose oven. The specimens were mounted upside-down on a polytetrafluoroethylene (PTFE) sample holder in order to prevent any precipitates that formed in the nutrient solution from falling onto the substrates which would have inhibited the growth of the NWs. Fig. 19e shows the plot of the air temperature profile inside the oven during nanostructure growth as a function of time (black squares): at first the temperature was increased gradually by 60 °C/h up to 85 °C and was then held at 85 °C for 2 hours. Then the heating was turned off and after an overnight cooling the sample was removed from the growth solution. Nevertheless, the actual temperature of the nutrient solution during nanostructure growth does not reach even 80 °C, as plotted by red circles in Fig. 19e. At solution temperature of 62 °C the nutrient solution became cloudy indicating the initiation of the reaction (dashed line in Fig. 19e). Finally the PMMA layer was

removed in acetone and the specimens were thoroughly rinsed with deionized water (Fig. 19d).

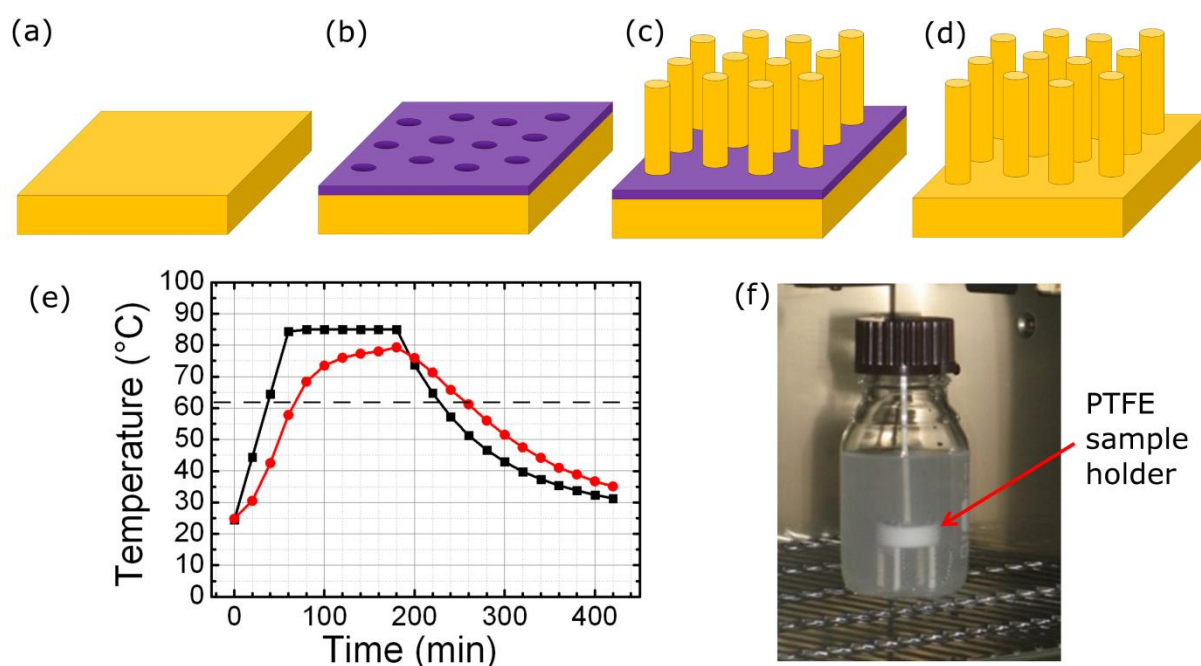


Figure 19. Schematic process flow of ZnO NR arrays. The fabrication steps are: surface treatment of ZnO seed surface (a), pattern generation in PMMA by e-beam lithography (b), chemical NW growth (c), and PMMA removal (d). Measured air temperature vs. time inside the multipurpose oven (black squares) and the corresponding actual solution temperature vs. time (red circles) during nanostructure growth (e). The dashed line indicates the initiation of the reaction. The NRs were synthesized in an aqueous solution: the specimen was mounted upside-down on a PTFE sample holder (f).

The resulting ZnO NW arrays were imaged by FE-SEM. Before nanostructure growth, the surface of the substrates was studied by AFM in semicontact mode. The thickness of the layers was determined by means of spectroscopic ellipsometry (Woollam M2000D rotating-compensator ellipsometer). The resistivity of the seed layers was measured using a four point probe method.

The crystal structure of BULK, PLD/sapphire, PLD/Si, PLD/Pt/sapphire and Sputt/Si seed layers and the corresponding NW arrays was investigated using high resolution XRD with a 50 μm diameter spot size, i.e. sufficiently smaller than the patterned areas. The XRD measurements were carried out at NIMS in Japan. A section of the Debye-Scherrer ring was studied using a 2D-detector system. In this approach, a $2\theta/\chi$ mapping around the (0002) peak is acquired simultaneously. The dispersion in the crystallographic alignment can then be estimated from the full width at half maximum (FWHM) along the χ direction while the

distribution of the c lattice parameter (and, hence, strain information) can be deduced from the FWHM along the 2θ direction [106].

In addition a cross-sectional TEM lamella representing the PLD/Pt/sapphire layer with the corresponding NWs was prepared and examined using TEM. The lamella was cut using FIB etching in the Zeiss 1540XB cross-beam system equipped with nanomanipulator. In order to protect the NWs from amorphization during the milling, photoresist was infiltrated at first into the NWs using spin coater. Hence the whole length of the NWs was covered with the protective polymer. The area to be thinned could be localized with micrometer accuracy on the sample surface by the high resolution FE-SEM and a high energy (30 keV, 5 nA) Ga^+ ion beam was used for sputtering. The thinning process of FIB was monitored by a scanning electron beam (Fig. 20a). After cutting out, the lamella was lifted out by the nanomanipulator and fixed onto a TEM grid inside the SEM chamber using SEM glue (Fig. 20b). The final thinning was made on the TEM grid. In order to minimize the thickness of the amorphized region at the front- and backside of the lamella, the final thinning was carried out using lower current (10-100 pA) Ga^+ beam.

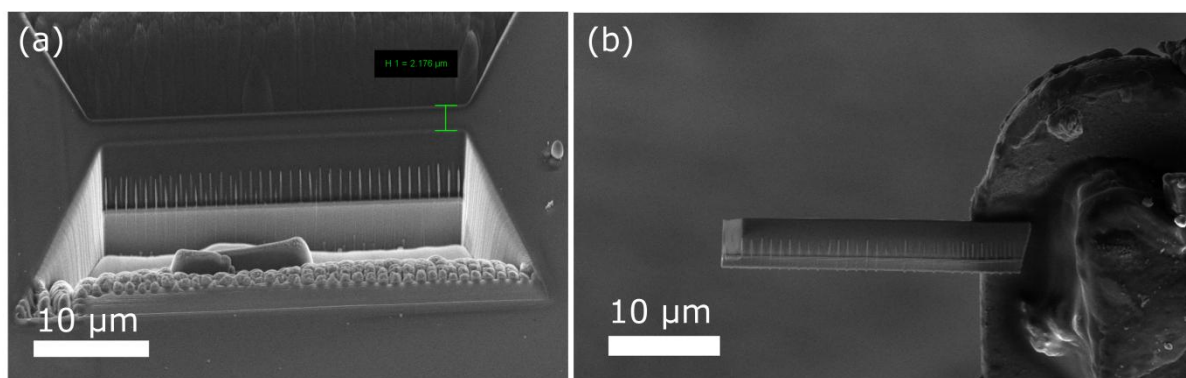


Figure 20. SEM micrographs of the cross-sectional TEM lamella preparation. Protecting photoresist was infiltrated into the NWs, the area to be thinned was localized, and the thinning process of FIB was monitored by the electron beam (a). The lamella was lifted out by nanomanipulator and glued on the TEM grid *in situ* inside the SEM chamber (b).

The piezoelectric activity of individual NRs was characterized by piezoresponse force microscopy (PFM) where the mechanical response of the investigated NRs was recorded on an alternating voltage signal. Our SmartSPM multimode scanning probe microscope mounted with a conductive AFM tip was used at an excitation signal of frequency of 52 kHz and amplitude of 6V. In order to determine the d_{33} constant (corresponding to longitudinal expansion/contraction along the c -axis in response to the applied electric field) of the inverse piezoelectric tensor represented by a 3×6 matrix in Voigt notation (see subsection 12.2. in

Appendix) for the NR the major part of the applied voltage has to be dropped on the NR, that is the resistance of the substrate is to be minimized. For this purpose NRs grown on PLD/Pt/sapphire were used, since a highly conductive Pt thin film of 100 nm exists beneath the ZnO seed layer of ~218 nm resulting in an overall sheet resistivity of 2.3 Ω/sq and providing an excellent bottom electrode for the NRs. In order to avoid the fracture of the NRs in contact mode scanning thicker NRs were synthesized for this particular purpose. However, in this case I applied a growth temperature of 95 °C (instead of 85 °C) and a concentration of 10 mM (instead of 4 mM), and wider nucleation windows (~500 nm) were generated in the PMMA with a spacing of 1 μm between them. The growth program (Fig. 19e) was interrupted after 2 h. For further protection the NRs were infiltrated by spin-coated photoresist. In order to make their tips accessible for the scanning probe the polymer was partly etched back in oxygen plasma (Fig. 21a). The photoresist encapsulation is also beneficial for increasing the PFM contrast. Note, that in the arrangement of Fig. 21a the underlying ZnO seed will also contribute to the piezoresponse signal. However, due to its lower vertical dimension compared to the NRs, the majority of the applied voltage will drop across the NRs. Nevertheless, for comparison I determined the d_{33} constant for the seed layer as well before resist infiltration at a position far from the patterned region (Fig. 21b).

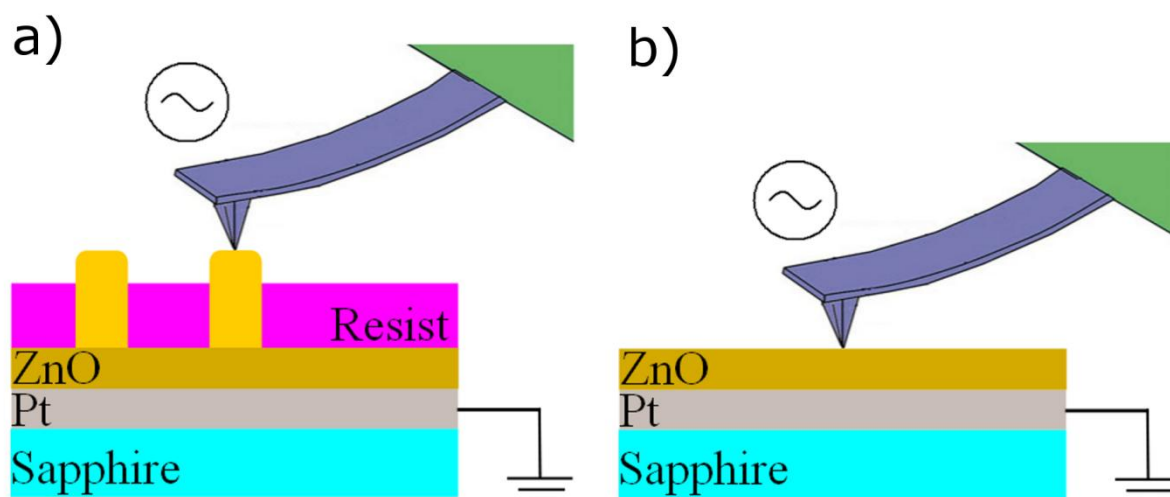


Figure 21. Schematic of the PFM characterization of ZnO NRs grown on PLD/Pt/sapphire (a) and the PLD/Pt/sapphire seed layer without the NRs (b). In order to avoid the fracture of the NRs in contact mode scanning thicker NRs were synthesized, which were infiltrated by spin-coated photoresist.

In order to study the impact of seed layer postdeposition annealing on NW alignment, I annealed three ZnO seed layers deposited by CVD on Si(100) in a quartz tube furnace at temperatures of 500 °C, 700 °C and 900 °C for 2h. The original thickness of the layers was

200 nm and the annealing atmosphere was artificial air (20% O₂ + 80% N₂). A fourth sample was left without heat treatment. After annealing ZnO NWs were grown on all four CVD ZnO layers by our template assisted wet chemical method, as described above. Although the shape of the air temperature profile in the oven was the same (Fig. 19e), in this case I applied 95 °C (instead of 85 °C) and a concentration of 10 mM (instead of 4 mM), and wider nucleation windows (~500 nm) were generated in the PMMA. The resulting NWs were examined in SEM. Before NW growth the surface of the seed layers was studied by AFM in semicontact mode. The deposition of CVD ZnO layers was done at CEA LETI (France).

4.2. Results and discussion

4.2.1. SEM and AFM study of the NWs and the different seed layers

As expected, the NWs grew in defined positions determined by the direct e-beam writing. The SEM micrograph of the patterned PMMA on BULK and the corresponding NWs are shown in Fig. 22.

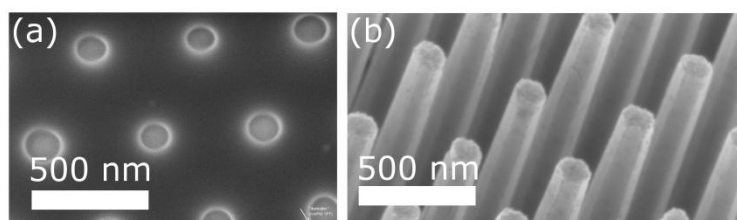


Figure 22. SEM micrograph of patterned PMMA layer on BULK (a) and the corresponding NW array (b). Note, that the electron beam can broaden the PMMA holes during SEM observation due to heating of the polymer.

The SEM images in Fig. 23a-n show that while all the growths gave regular arrays with NW ~2 μm long and 100-200 nm diameter, the various seed surfaces resulted in different NW morphologies and orientations. The NWs grown on the BULK (Fig. 23a and h), PLD/sapphire (Fig. 23b and i), ALD/GaN (Fig. 23c and j), and PLD/Si (Fig. 23d and k) seed surfaces were strongly aligned with the normal to the surface, while those grown on PLD/SiO₂/Si (Fig. 23e and l), PLD/Pt/sapphire (Fig. 23f and m), and Sputt/Si (Fig. 23g and n) had greater dispersion in their orientation and a more tapering geometry. Moreover, the NWs grown on the BULK, the PLD/sapphire, and the ALD/GaN showed a common relative orientation of their hexagonal crystal facets in the surface plane (Fig. 23a-c). Closer observation of the NW grown on the Sputt/Si (Fig. 23g and n), PLD/Pt/sapphire (Fig. 23f and m), PLD/SiO₂/Si (Fig.

23e and l), and PLD/Si (Fig. 23d and k) also revealed that, in some cases, multiple NWs grew in single growth windows.

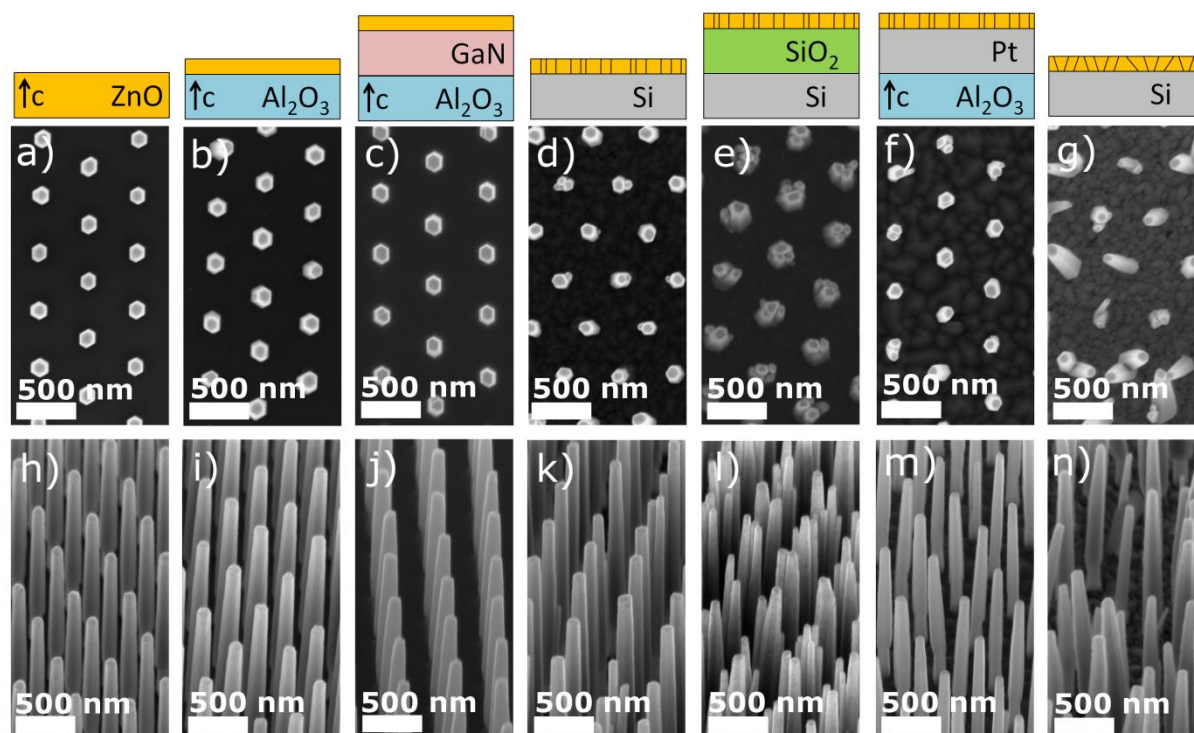


Figure 23. Top- (upper row) and tilted-view (lower row) scanning electron micrographs of vertical ZnO NWs grown on different substrates: ZnO single crystal (a and h); PLD deposited ZnO on c-Al₂O₃(0001) (b and i); ALD deposited ZnO on GaN/c-Al₂O₃(0001) (c and j); PLD deposited ZnO on Si(111) (d and k); PLD deposited ZnO on thermal SiO₂/Si(100) (e and l); PLD deposited ZnO on Pt/c-Al₂O₃(0001) (f and m); reactive magnetron sputtered ZnO on Si(100) (g and n)

Table 3 shows the thickness, resistivity, and root mean square (RMS) roughness for the different seed surfaces.

sample	seed layer				
	deposition	thickness (nm)	resistivity (Ωcm)	roughness(nm)	crystal structure
BULK			1.5×10^2	0.18	single crystal
PLD/sapphire	PLD	139	5.40×10^{-1}	0.46	epitaxial
ALD/GaN	ALD	32	1.94×10^{-3}	0.28	epitaxial
PLD/Si	PLD	427	4.19×10^{-1}	3.88	highly textured
PLD/SiO ₂ /Si	PLD	45	4.01×10^1	1.78	highly textured
PLD/Pt/sapphire	PLD	218	5.12×10^{-5}	9.85	highly textured
Sputt/Si	sputtering	155	4.14×10^{-3}	7.58	textured

Table 3. Details of the compared seed structures (in the case of PLD/Pt/sapphire, an effective resistivity is calculated for the ZnO/Pt bilayer).

The AFM images in Fig. 24 suggest that the PLD/Si (Fig. 24d), PLD/SiO₂/Si (Fig. 24e), PLD/Pt/sapphire (Fig. 24f), and Sputt/Si (Fig. 24g) seed layers are composed of tiny crystals. In the case of PLD/Si and Sputt/Si, the grains appear to range from several tens of nanometers up to hundred nanometers in diameter, while, in the case of PLD/Pt/sapphire, the grain diameters appear to be in the several hundreds of nanometer range, and in the case of PLD/SiO₂/Si, far below the one hundred nanometer range. This could explain the presence of multiple NWs on the PLD/Si, PLD/SiO₂/Si, PLD/Pt/sapphire, and Sputt/Si seed layers, since the average grain size is comparable to or lower than the diameter of the e-beam lithography patterned growth windows (~120-130 nm). Thus, there is a significant probability that more than one grain in the seed layer can nucleate in a single growth window. This explanation is supported by the observation that fewer multiple NW grew on the PLD/Pt/sapphire, which had larger crystals (Fig. 24f), than the PLD/Si, PLD/SiO₂/Si and Sputt/Si. The BULK, PLD/sapphire and ALD/GaN substrates have the smoothest surfaces, moreover, they also have significantly larger grain sizes. This could explain the common relative orientation of the NW hexagonal crystal facets as the result of epitaxial growth of the NWs on grains large enough to spread out below several or all of the growth windows. It has to be noted here, that PLD/SiO₂/Si seems to be a promising candidate as a CMOS compatible seed layer supporting very good vertical NW alignment. However, PLD deposition is usually carried out at substrate temperatures far above the CMOS temperature limit (400 °C).

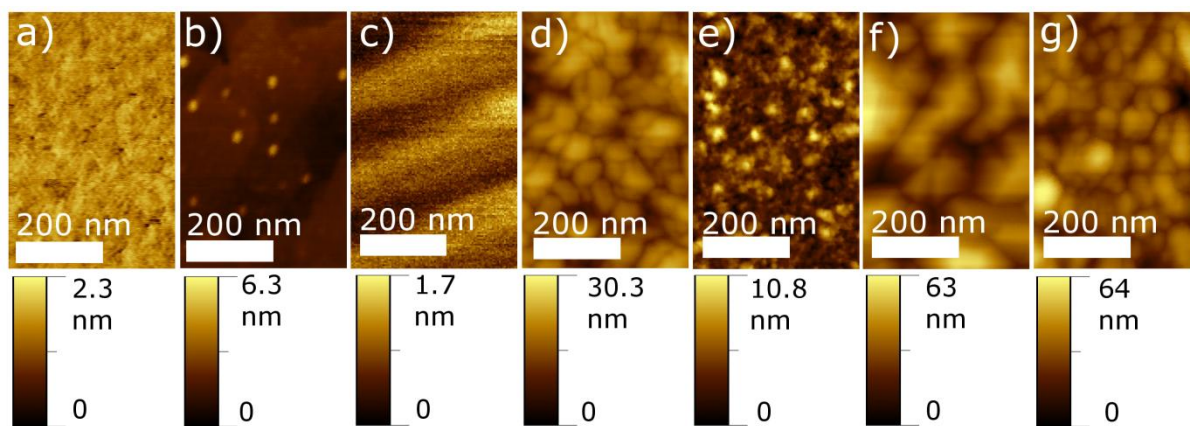


Figure 24. AFM images of ZnO seed surfaces: ZnO single crystal (a); PLD deposited ZnO on c-Al₂O₃(0001) (b); ALD deposited ZnO on GaN/c-Al₂O₃(0001) (c); PLD deposited ZnO on Si(111) (d); PLD deposited ZnO on thermal SiO₂/Si(100) (e); PLD deposited ZnO on Pt/c-Al₂O₃(0001) (f); reactive magnetron sputtered ZnO on Si(100) (g).

4.2.2. Structural characterization of the NWs and the corresponding seed layers

By comparing the RMS roughness values listed in Table 3 and the SEM images of the grown NW arrays (Fig. 23), it can be seen that the smoother seed surfaces have more aligned NWs. However, it is not obvious whether the roughness or the crystal structure of the seed layers is responsible for the growth direction of the NWs. In order to establish a better understanding of the relationship between the seed layer and the NWs, a more sophisticated structural investigation was needed. Since the size of the e-beam lithography patterned areas was larger ($150\ \mu\text{m} \times 150\ \mu\text{m}$) than the diameter of the X-ray beam spot ($\sim 50\ \mu\text{m}$) of the used XRD system, the patterned parts with NWs and the unpatterned parts without NWs can be examined separately. XRD was applied on BULK, PLD/sapphire, PLD/Si, PLD/Pt/sapphire and Sputt/Si.

In a pole figure measurement, a certain set of hkl - or $hkil$ -planes is selected by fixing the detector (2Θ) and incident beam (Θ) angle. Hence, the scattering vector \mathbf{S} is fixed in space, and diffraction will only occur if the normal of the selected hkl -/ $hkil$ -planes is parallel to the diffraction vector. Therefore, the sample has to be tilted (Ψ) and rotated (Φ) in space. Pole figures can be interpreted by considering the intersections of the normal to the selected hkl -/ $hkil$ -planes with an imaginary hemisphere, situated above the sample surface (Fig. 25a). The projection of this hemisphere on a planar surface results in a pole figure, for which the intensity in each point is proportional to the number of grains in the film that have their normal to the selected hkl -planes pointing to the point with coordinates (Ψ, Φ) on the hemisphere.

XRD pole figures of the BULK crystal and the corresponding NW array revealed 6-fold rotational symmetry with sharp $\{10\bar{1}1\}$ peaks (not shown here), which can be explained by their wurtzite-type single crystalline nature. The XRD pole figure for the PLD/sapphire layer in Fig. 25b also shows 6-fold symmetry for the $\{10\bar{1}1\}$ plus an epitaxial relationship based on a 30° in-plane twist with respect to the c-sapphire substrate (Fig. 25c; $\text{ZnO } [10\bar{1}0] \parallel \text{sapphire } [11\bar{2}0]$) [107], as has been generally reported in the literature [108-109]. This epitaxy, in spite of a 18.4% in-plane lattice mismatch, can be explained as a result of the compliant nature of wurtzite ZnO [110]. The schematic of the epitaxial relationships of ZnO (0001) layer and the Al_2O_3 (0001) substrate is shown in Fig. 25d. Although ALD/GaN was not examined here, it has to be noted that the epitaxial nature of the film growth for ALD ZnO on a thick epitaxial MOCVD GaN film on c-sapphire was also presented previously by Baji *et al.* [111]. In the

case of the PLD/Si, PLD/Pt/sapphire, and Sputt/Si samples, the seed layers and NWs all had rings in XRD pole figures, indicative of preferential c-axis orientation along the film growth direction and random crystallographic orientation in the film plane [103]. Indeed, the high adatom mobility in PLD allows the ZnO to crystallize readily even on amorphous substrates, such as the native SiO₂ passivation layer on the surface of the Si substrate [112].

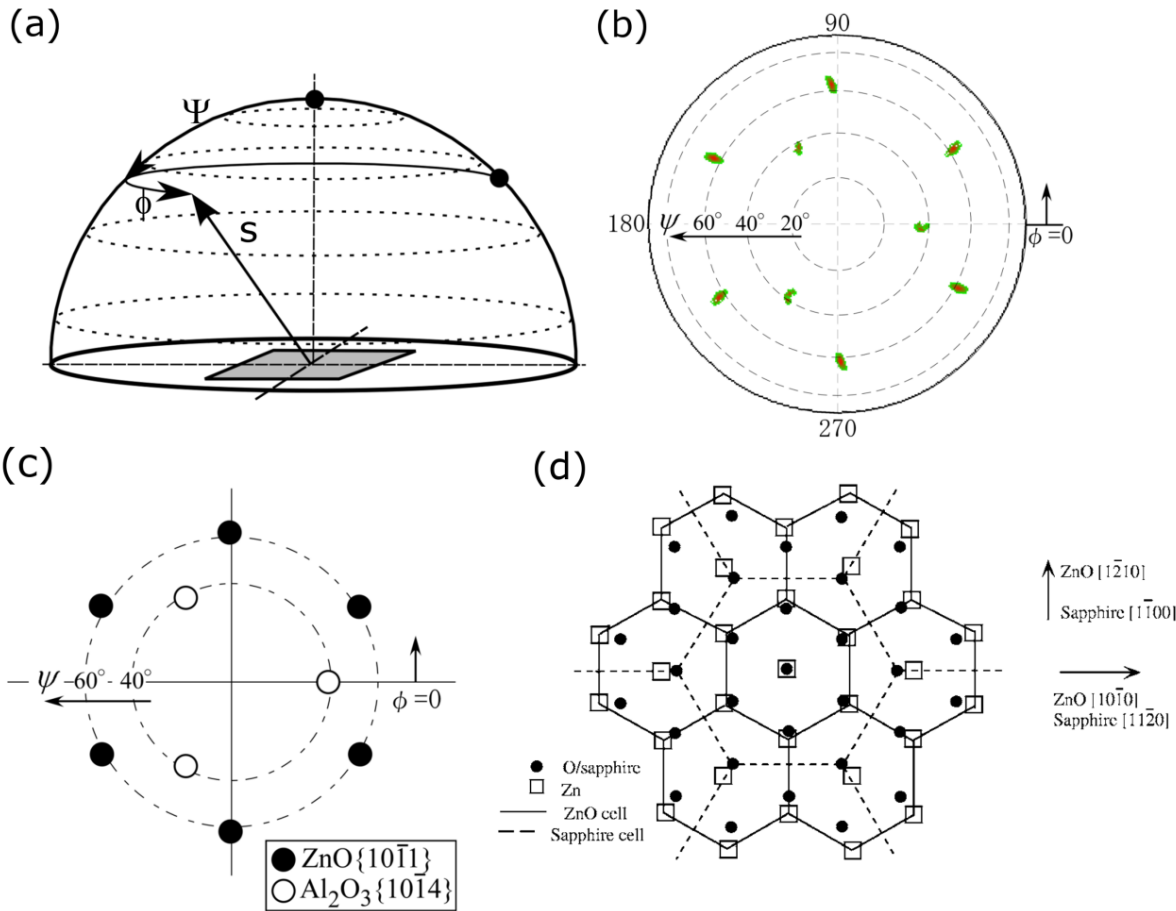
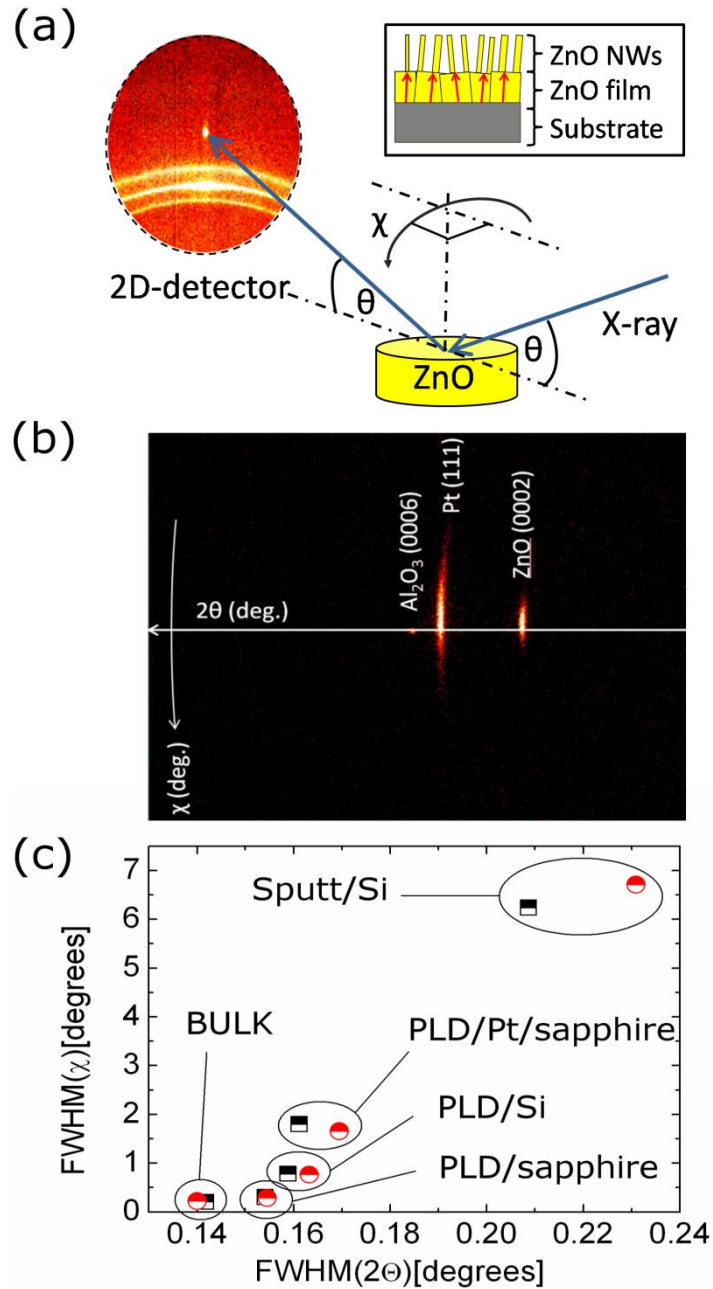


Figure 25. (a) Schematic illustration of pole figure measurement. Measured (b) and theoretical (c) pole figure for PLD deposited ZnO on c-Al₂O₃(0001). Schematic diagram showing the epitaxial relationships of ZnO (0001) grown on Al₂O₃ (0001) (d) (image d adapted from [7]).

In previous XRD studies of the PLD ZnO/SiO₂/Si, Zerdali *et al.* found pole figures with sharp rings and deduced that the films had a fibrous texture with strong preferential orientation of the c-axis along the film normal and an a-axis which was oriented randomly in the film plane [103]. Such a structure is coherent with the SEM image in Fig. 23d, which shows that the facets of the NWs are not aligned collectively in the same direction, but denoting random in-plane rotation of the NW grains. The same is true for the NWs on the PLD/Pt/sapphire and Sputt/Si surfaces (Fig. 23f and g).



to reproduce the crystallographic dispersion in the seed layers. Fig. 26c also shows that the FWHM 2θ for the NW arrays are significantly lower than those of their seed layer when grown on the more disoriented seed layers (Sputt/Si, PLD/Pt/sapphire, PLD/Si). This can be explained as the result of strain relaxation during NW growth.

The impact of the roughness on the NW growth was investigated by an additional PLD/sapphire type specimen having a rougher top surface. The AFM image in Fig. 27a for this ZnO surface shows a significantly higher surface roughness (4.15 nm) than that for the former PLD/sapphire in Fig. 24b (0.46 nm). In contrast, the SEM observations on both NW arrays show almost the same morphologies (Fig. 27b and c). Hence, the alignment of the NWs is mainly dictated by the crystal structure of the seed surface and not by the surface roughness.

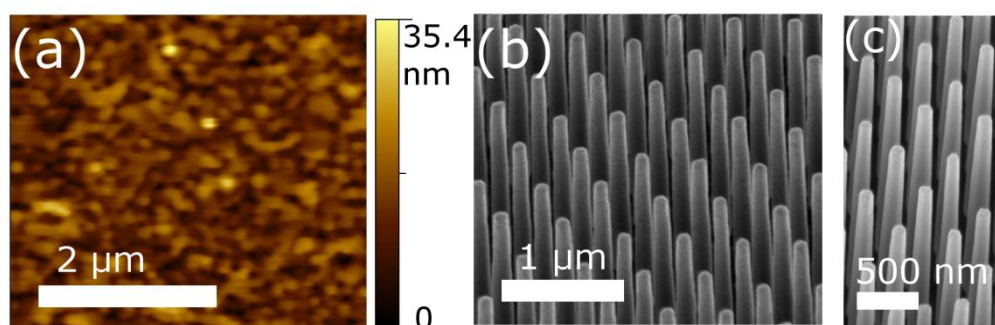


Figure 27. AFM image of a PLD deposited ZnO seed layer on c-sapphire with increased roughness (a) and scanning electron micrograph for the corresponding NW array (b). For comparison, the SEM image of the NWs grown on PLD/sapphire (c).

A more detailed examination of the crystallographic relationship between the seed layer and the NWs can be achieved if we record SAED patterns from different parts of the cross-sectional TEM lamella of PLD/Pt/sapphire. Fig. 28a and b show bright field TEM images with different magnifications taken from the lamella. It can be seen, that the ZnO seed layer above the Pt buffer layer is composed of columnar grains of a few hundred nanometers. The NWs consist of two parts: a shaft at the bottom, which was formed by filling the hole in the PMMA layer and a longer upper part. In accordance with the SEM images and the XRD results the alignment of the NWs show dispersion about the surface normal. Fig. 28c depicts the SAED pattern taken from the grain beneath a given NW from the $z = [2\bar{1}\bar{1}0]$ zone axis. This was considered as reference, and further two SAED patterns were recorded without tilting the sample from the corresponding shaft, and the upper part of the NW (not shown here). In the case of the latter two the ZnO crystal was in the same zone axis as the grain

underneath, however, we observed a slight twist between the seed crystal and the NW, which can be explained by the nature of the thinning method and can be considered as an artifact. Therefore homoepitaxial relationship exists between the ZnO seed grains and the corresponding NWs.

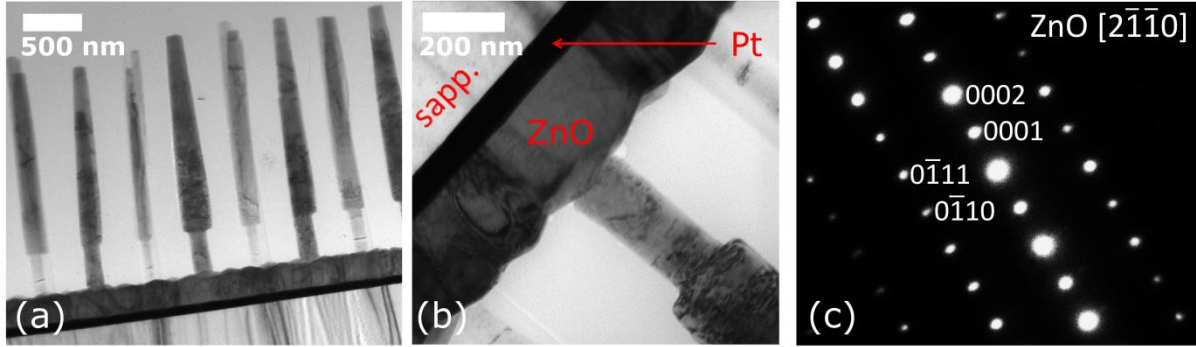


Figure 28. Transmission electron micrographs of vertical ZnO NWs grown on PLD deposited ZnO on Pt/c-Al₂O₃(0001) in lower (a) and higher (b) magnification; SAED pattern taken from a ZnO grain in the seed layer having a homoepitaxial NW above (c).

4.2.3. Piezoelectric characterization of the NWs

Fig. 29e shows the SEM micrograph of the thick bundles of highly ordered NWs before resist infiltration synthesized on PLD/Pt/sapphire for the piezoelectric characterization. The obtained AFM height (Fig. 29b) and the corresponding piezoresponse (Fig. 29d) image show that the maximal piezoresponse values were obtained at the NWs and the calculated d_{33} values are in the 6-12 pm/V range, similarly to the results reported by Scrymgeour *et al.* [113]. The mean value for the NWs is 8.4 ± 1.7 pm/V, which is close to the bulk value (12.4 pm/V) obtained for Li compensated highly resistive ($>10^8$ Ω cm) ZnO crystal [114] which can be regarded as the maximal experimental value for ZnO. The averaging was done on the pixels corresponding to the NWs, and \pm indicates the standard deviation of the measurements. The obtained piezoresponse map recorded for comparison on the seed layer (Fig. 29c) shows that the calculated d_{33} for the underlying PLD ZnO falls in a lower range (3-7 pm/V). The mean value for the seed layer is 4.8 ± 0.6 pm/V. Here the averaging was done on the whole piezoresponse map. The considerably high difference between the piezoelectric constant of the seed layer and that of the NWs is presumably due to the difference between the charge carrier concentrations. It is well known for decades, that piezoelectric semiconductors show a strong dependence of the piezoelectric coefficient on the carrier concentration and hence the conductivity, i.e. the piezoelectric coefficient decreases when the carrier concentration

increases [115]. This screening phenomenon can also influence the operation of the proposed nanoforce sensor, as discussed in chapter 3. Although in the targeted NEMS device the piezoelectricity of the seed layer plays the higher role instead of the electromechanical behavior of the NR, the relatively high piezoresponse of the wet chemically grown NRs can be beneficial for other types of nanoelectromechanical sensors and energy harvesting devices.

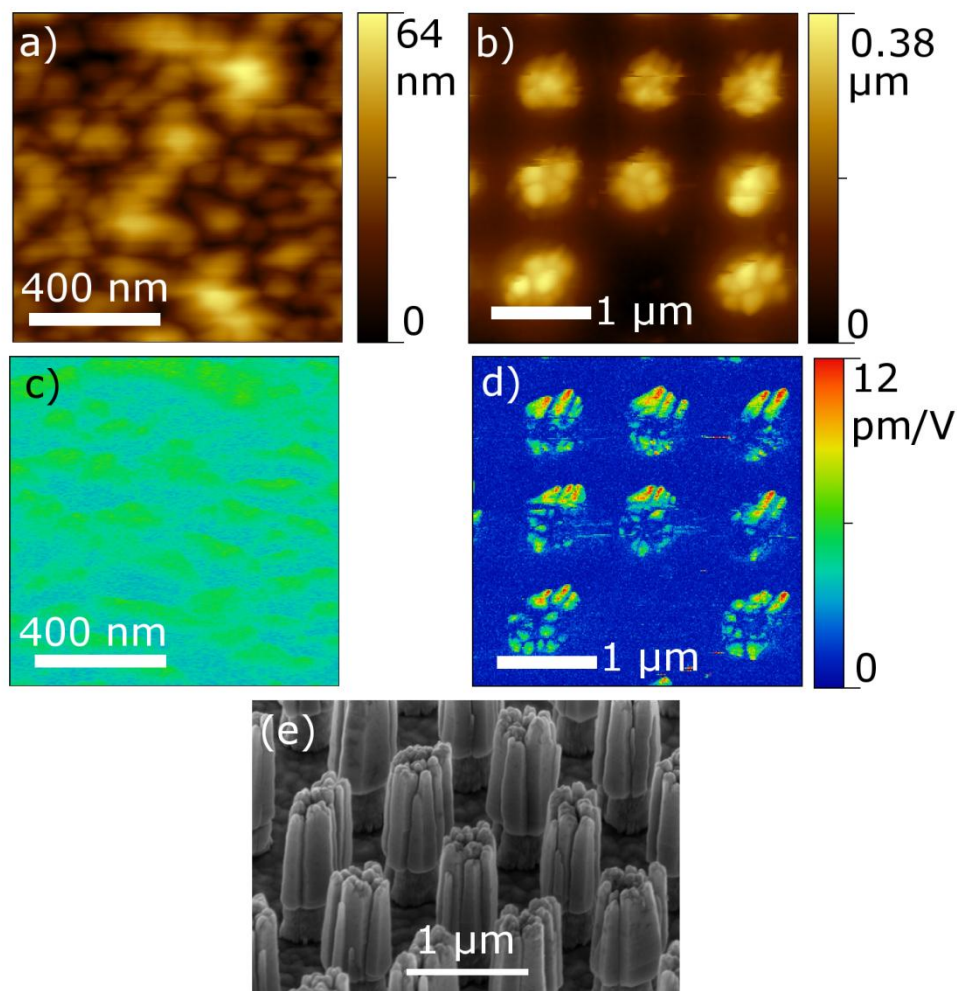


Figure 29. The measured contact mode height and the corresponding piezoresponse map of the PLD ZnO seed layer (a and c respectively) and those of the NWs after resist infiltration and plasma etching (b and d respectively). SEM image of the thick polycrystalline ZnO NRs grown on PLD/Pt/sapphire template (e).

4.2.4. The effect of seed layer annealing

The AFM images in Fig. 30 show, that the grain size of the CVD ZnO seed layers increased with increasing postdeposition annealing temperature. If we compare the SEM images of the obtained NW bundles with the corresponding seed layers, it can be concluded, that higher temperature results in a better vertical NW alignment.

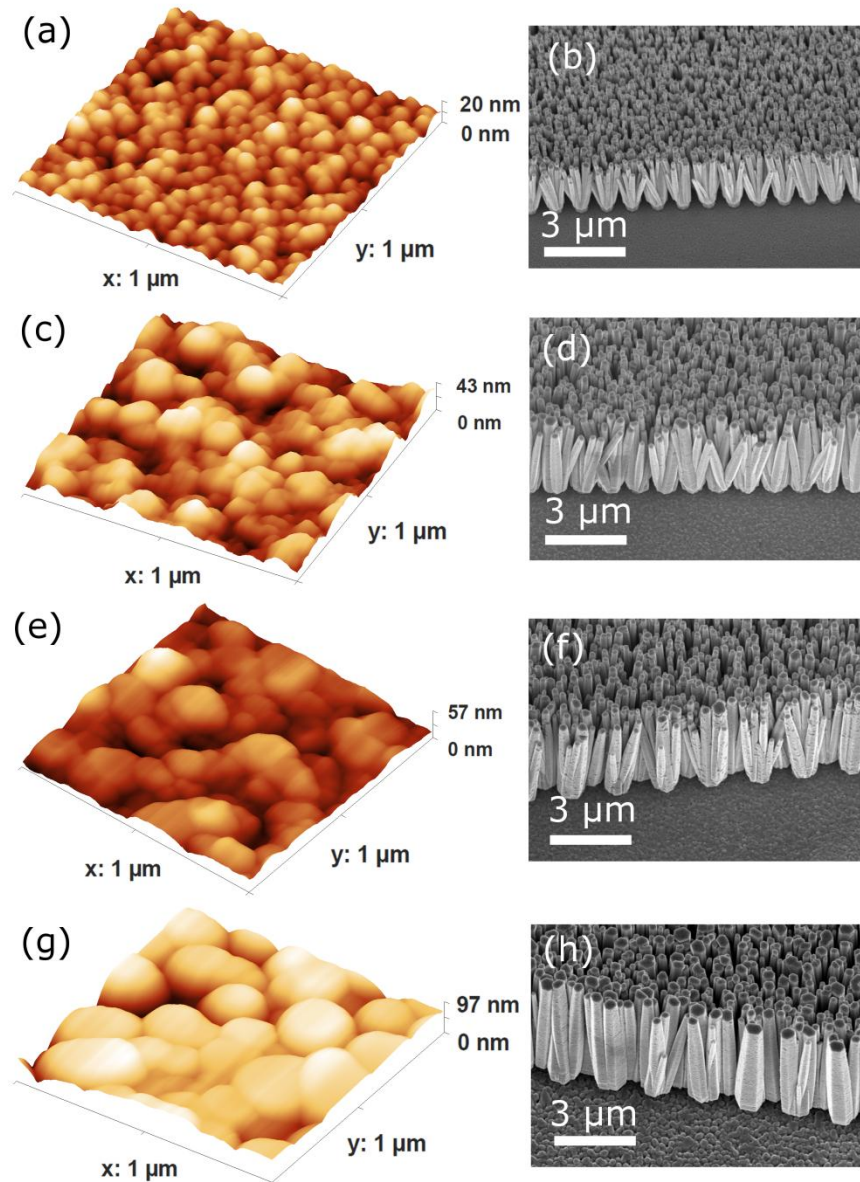


Figure 30. Tapping mode AFM topography images of CVD ZnO seed layers: without postdeposition annealing (a), and after postdeposition annealing for 2h at 500°C (c), 700°C (e), and 900°C (g). SEM micrographs of the corresponding ZnO NW bundles: (b), (d), (f), and (h), respectively.

It is well known for a long while, that the conditions of thin film deposition strongly influence the layer formation process and hence the quality of the resulting polycrystalline thin film [116]. It was also shown that postdeposition annealing can be beneficial to improve the crystallite orientation of polycrystalline ZnO thin films. Lad *et al.* observed increased alignment of (002) crystal planes parallel to the substrate and considerable stress relief after annealing up to 700 °C [117]. Moreover Gupta *et al.* observed a process of coalescence during postdeposition annealing (at temperatures up to 1073 °C) leading to increased grain size [118]. Since the alignment of my NWs is dictated by the dispersion in the

crystallographic orientation of the underlying ZnO seed, it is not surprising, that definite improvement in the vertical alignment can be achieved by additional heat treatment of seed layers. From the point of view of CMOS compatibility it can be concluded, that although the NWs are grown on Si(100), unfortunately the high annealing temperatures (>500 °C) are far above CMOS technology limit (400 °C).

In summary, regular ZnO NW arrays were grown on various ZnO seed surfaces using low temperature wet chemical growth at template windows patterned in a resist overlayer using e-beam lithography. SEM study revealed that NW arrays which were seeded on ZnO single crystal and ZnO thin films grown epitaxially on c-sapphire by PLD and GaN/c-sapphire by ALD showed strong c-axis alignment with the surface normal and a common relative orientation of their hexagonal crystal facets in the surface plane. This was taken to be indicative of a-axis ordering with respect to the substrate and is consistent with the NWs growing epitaxially on ZnO grains in the seed layers which were relatively large compared to the spacing of the NWs (500 nm) and thus encompassed many template windows. It can be anticipated that such in-plane ordering may offer novel properties in applications such as photonic crystals [91] or self-forming laser cavities, in which the relative orientation of grain boundaries plays an important role, since they act as light scatterers [119]. NW arrays grown on less oriented ZnO underlayers (on both Si, SiO₂/Si, Pt/sapphire substrates) showed reduced c-axis alignment, and the crystallographic orientation in the plane was random. In the case of polycrystalline ZnO seed layers, the alignment of the NWs showed increased dispersion about the normal and occasionally showed multiple NW emanating from a single nucleation window. It was inferred from AFM images that this may be due to the grain size in the seed layer being smaller than the template window in the resist layer.

Quantitative XRD, AFM and TEM analysis revealed that the crystal quality and alignment of the NWs was determined by the dispersion in the crystallographic orientation of the seed layer while the effect of the surface roughness appeared to be negligible. The growth approach and substrate/seed-layer/NW combinations examined in this study demonstrated the potential for low-cost fabrication of highly aligned NW arrays with precise tuning of the NW/NR dimensions and positioning plus some degree of control over the form, out-of-plane alignment, and in-plane crystallographic orientation via the choice of seed layer. This could have potential for use in applications ranging from active nanophotonic elements to energy harvesting and sensor devices. In particular, NWs grown on epitaxial ZnO layers grown on c-sapphire by PLD gave comparable results to those grown on bulk hydrothermal substrates.

This agrees with studies contrasting the homoepitaxial regrowth of ZnO thin films on hydrothermal ZnO and PLD ZnO/sapphire by CVD [120] and suggests that epitaxial layers on sapphire may offer a lower-cost and wider area alternative to single crystal substrates as templates for the growth of highly ordered ZnO NW arrays. Therefore vertical NWs can be grown onto conventional substrates and hence integrated into Si technology, which is essential for state-of-the-art ZnO NW based NEMS devices.

As it was pointed out by PFM the wet chemically grown NRs showed high piezoelectric constant (8.4 ± 1.7 pm/V) which can be beneficial for nanomechanical sensors and energy harvesting devices. It was also shown, that definite improvement in the vertical alignment of the NWs can be achieved by additional heat treatment of seed layers.

5. Validation of the static bending test inside the SEM

Since the main goal of this work is the development of a ZnO NR based nanoforce sensor device, it is essential to determine the Young's modulus of these perpendicularly standing nanocrystals. It can be seen in Fig. 23, that they can be practically considered as one-end affixed cantilevers. The most common method to determine the Young's modulus of one dimensional one-end affixed nanostructures is the resonance excitation method [44] (see subsection 1.3.1.). However, the low aspect ratio of my template assisted wet chemically grown ZnO NRs (<20) makes this experiment rather difficult because of their rigidity, which leads to the necessity of high exciting voltages inside the electron microscope and makes the resonances unrecognizable. Furthermore, the method strongly depends on the electrical properties of the substrate and the NWs to be measured. Moreover, the low aspect ratio also leads to high resonance frequencies (compared to common NWs with resonance frequencies in the kHz range); therefore high frequency arbitrary function generator would be necessary for the excitation. For instance, if we choose a typical NR from Fig. 23h grown on BULK having a length of 1570 nm and a hexagonal cross-section with an edge of $a = 81$ nm, the natural resonance frequency can be estimated according to the classical equation of one-end affixed cantilever [121]:

$$v_{rez} = \frac{\beta_i^2}{2\pi L^2} \sqrt{\frac{EI}{m}} \quad (12)$$

where β_i is a constant for the i th harmonic: $\beta_1 = 1.875$, and $\beta_2 = 4.694$, E is the Young's modulus along the longitudinal axis (i.e. in the [0001] direction; here 140 GPa was applied as the bulk Young's modulus of ZnO [72]), m is the unit length mass, L is the length of the cantilever, and I is the second moment of inertia. By considering the edge of the hexagon (a), m and I can be calculated for the hexagonal cross-section:

$$m = \frac{3\sqrt{3}}{2} a^2 \rho \quad (13)$$

$$I = \frac{5\sqrt{3}}{16} a^4 \quad (14)$$

where ρ is the mass density of ZnO (5.61 g/cm^3). The result for I is valid for both a horizontal and a vertical axis through the centroid. Therefore the first harmonic can be estimated to be $\nu_1 = 41.9 \text{ MHz}$.

Due to the aforementioned problems, I performed a well controlled *in situ* static bending test in a SEM on individual cantilevered nanostructures to determine the bending modulus (BM). In this chapter first I prove, that the static bending experiment leads to the same result as the more commonly used resonance excitation method, and I determine the BM of low aspect ratio homoepitaxially grown vertical ZnO NRs using the static method afterwards in chapter 5. Here for the validation I present the examination of high aspect ratio (typically ~ 100) InAs NWs, which allow us to carry out both experiments since it is rigid enough for static bending experiment but has a moderately low first natural resonance frequency (typically ~ 500 - 600 kHz). Note, that these methods are not restricted to special materials. Although neither static bending nor the resonance excitation in electron microscope is novel, to my knowledge this thesis, and the corresponding publication [T3], is the first work on applying both techniques on the same individual, cantilevered nanostructures. To understand better the connection between the determined elastic modulus and elasticity theory, see the related part of Appendix (subsection 12.1.).

InAs is a III–V semiconductor, which has a number of parameters, such as direct band gap of 0.36 eV , electron mobility greater than $20.000 \text{ cm}^2 \text{ V}^{-1} \text{ s}^{-1}$ at 300 K , strong spin-orbit interaction, Schottky-barrier free contacts, and gate tunable electron density, which makes it a good candidate for future nanoelectronics [122]. However, the number of reports about the mechanical observation of InAs cantilevered nanostructures is very limited. Mariager *et al.* excited three different acoustic oscillations of vertical InAs NWs by a femtosecond laser pulse [123]. Lexholm *et al.* studied the dynamic behavior of epitaxially grown InAs NWs with diameters ranging from 40 to 90 nm using optical stroboscopic imaging. They observed a decrease in Young's modulus with smaller diameters [124]. However, the crystal structure of their NWs was not examined in details, but claimed to go towards wurtzite for smaller diameters. InAs in bulk form always shows pure zinc-blende structure, nevertheless wurtzite InAs was observed for the first time by Koguchi *et al.* in nanowhiskers [125]. Caroff *et al.* showed that the crystal structure of InAs NWs can be controlled with NW diameter and the growth temperature [126]. At small diameters the wurtzite structure is typical, and as the diameter is increased, mixed phases with different zinc-blende content or pure cubic structure

can be achieved. By sidewall deposition during growth, Shtrikman *et al.* demonstrated a method to obtain thicker NWs with pure wurtzite crystal structure [127].

5.1. Experimental subsection

The examined NWs were synthesized by solid source molecular beam epitaxy (MBE) on InAs(111)B substrates in a Varian GEN II MBE machine at the Niels Bohr Institute (University of Copenhagen). The substrates were degassed at 250 °C for 1 h in a buffer chamber, and at 550 °C for 8 min, with an As backing pressure, immediately before depositing gold. A thin layer of gold was evaporated at this elevated temperature and then annealed for 4 min. Hereafter the temperature was lowered to 445 °C, and the growth initialized by opening the In shutter. The wires were grown for 30 min at this temperature and for another 30 min with a temperature ramp to 455 °C. High flux rates of both In and As₂ was used, with beam equivalent pressures (BEP) of 7.0×10^{-7} Torr and 1.3×10^{-5} Torr, respectively, giving a V/III ratio of 19. The growth takes place via VLS mechanism (see subsection 1.2.2.).

The crystal structure of the obtained nanostructures was examined by TEM. The morphology of the NWs was examined by FE-SEM and the mechanical characterization was composed of two *in situ* successive measurements on the individual NWs in the SEM chamber. At first I carried out a static bending test on a randomly selected NW by an AFM cantilever mounted on a nanomanipulator arm. The AFM cantilever was fixed to the very end of the robotic arm (Fig. 14c) at its support chip by soldering. A soft silicon nitride cantilever (Veeco DNP-S20) was chosen to maximize the sensitivity of the method. Fig. 31c shows the SEM micrograph of the triangular nitride cantilever attached to the support chip with a sharp tip at the end. Before mounting the nitride chip on the nanomanipulator arm, the spring constant was calibrated in AFM using a reference Si cantilever. The NW was bent at its free end along the $\langle 11\bar{2}0 \rangle$ crystallographic direction by a lateral load perpendicular to the vertical axis by moving the sample with the stage towards the AFM tip (Fig. 31a). The direction of the stage movement was lying in the same axis (x-axis on Fig. 31b) as the $\langle 11\bar{2}0 \rangle$ crystallographic direction and was perpendicular to the plane of the AFM cantilever. During manipulation the stage (together with the robotic arm) was tilted around the x-axis by 45° to make the height of the applied load visible (Fig. 31d). In order to maintain a permanent contact between the tip of the probe and the sidewall of the NW during manipulation, an incision was etched by FIB at the end of the tip with a radius of curvature comparable to the cross-sectional radius of the NW.

The schematic side-view and top-view of the measurement and a typical SEM image recorded during the manipulation are shown in Fig. 31a, 31b, and 31d respectively.

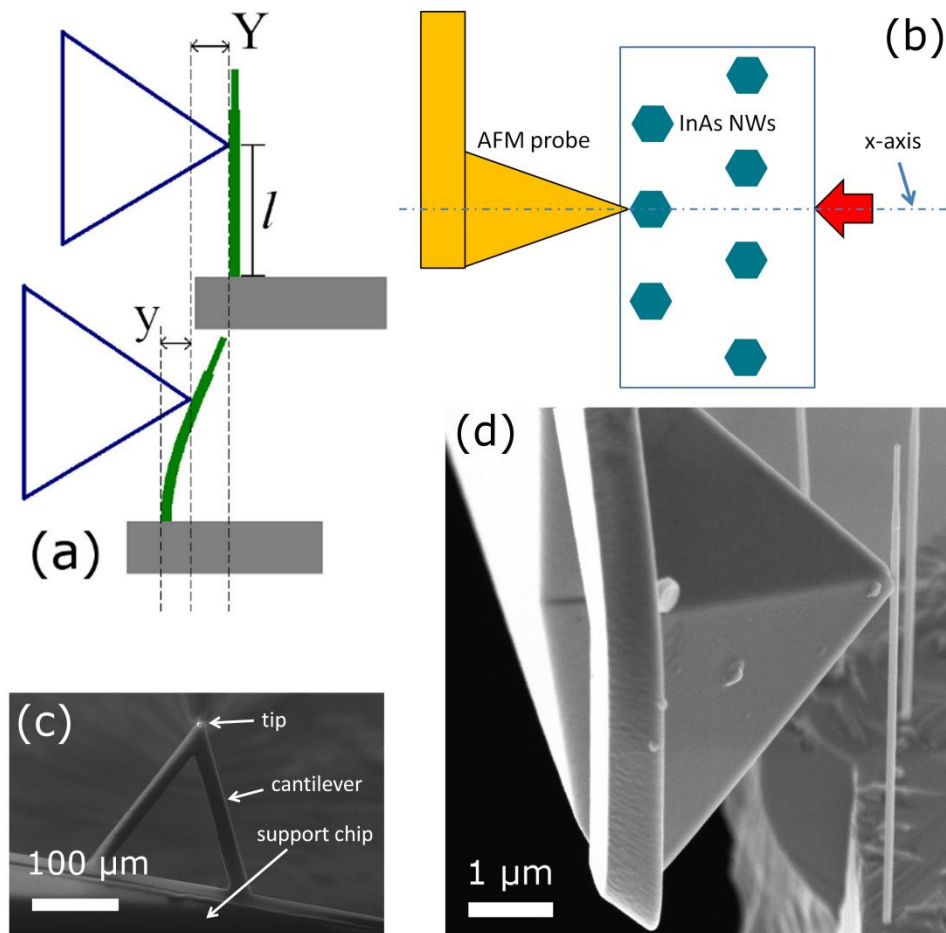


Figure 31. Schematic side-view (a) and top-view (b) of the static bending test on a single InAs NW. The relative position of the tip and the hexagonal cross-section of the NWs in (b) indicates that the bending load was applied in the $\langle 11\bar{2}0 \rangle$ crystallographic direction. Snapshots were taken in relaxed and stressed states to determine both cantilever and NW deflections (Y and y , respectively) and the vertical position of the applied load (l) (a). The corresponding SEM micrograph of the measurement (d). SEM micrograph of the triangular nitride cantilever attached to the support chip with a sharp tip at the end (c).

For data acquisition two snapshots were recorded during the bending: one in stressed and the other one in relaxed state. By overlapping the two snapshots, both NW and tip deflections could be determined (y and Y ; Fig. 31a). No plastic deformation was observed, therefore all deflections measured in this work can be assumed to be purely elastic.

The second *in situ* measurement was carried out on the same NW immediately after the manipulation with the AFM tip. Here the electrically induced mechanical resonance of the NW was studied by positioning the edge of a tungsten tip above the free end of the NW at a

distance of a few hundred nanometers (see subsection 1.3.1.). The tip was mounted on a second nanomanipulator arm. The direct component of the applied electric field was $V_{DC} = 1.36$ V, while the alternating part was $V_{AC} = 1$ V. By sweeping the applied frequency the resonance frequency was determined. I examined the first harmonic oscillation in each case. When the NW was in resonance, a snapshot was recorded showing the blurred oscillation of the NW between the two extrema. However, the edges of this blurred area could be clearly seen and hence the amplitude of the resonance could be easily determined.

5.2. Results and discussion

5.2.1. SEM and TEM study of the InAs nanowires

The SEM study revealed that the NWs are perpendicularly standing on their substrate (Fig. 32a) and having hexagonal cross-sections which are coherently aligned in the substrate plane. The NWs are constituted by a lower thicker and an upper thinner hexagonal prism shaped segments with a length ratio of 85:15, respectively. According to image analysis the average length and diameter are 9.6 ± 3.1 μm and 93 ± 11 nm, respectively. Due to the growth method, a hemispherical gold catalyst particle remained at the free end of the NWs (Fig. 32c).

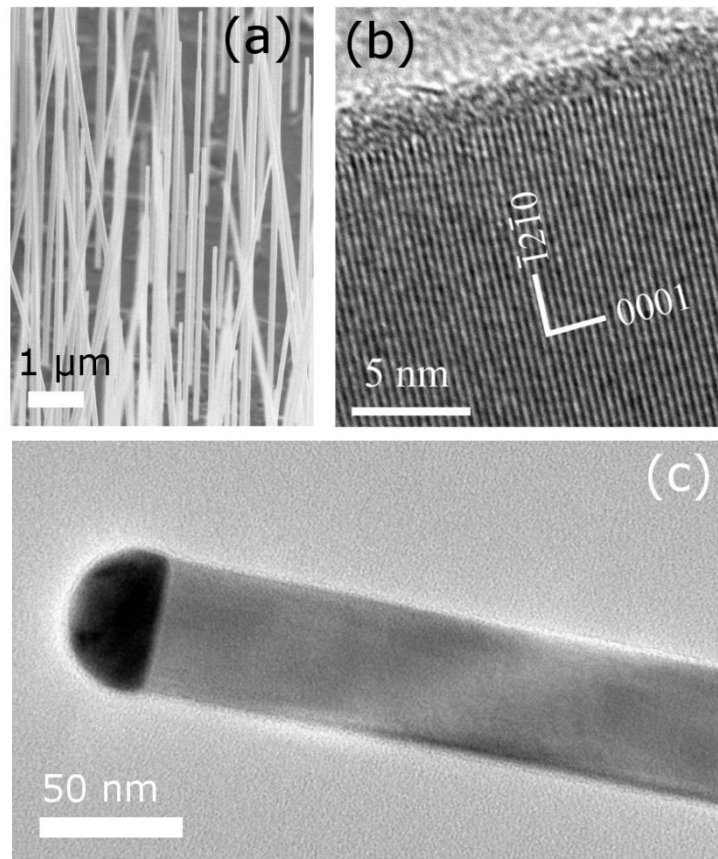


Figure 32. Electron microscopy images of InAs NWs grown by molecular beam epitaxy on an InAs(111)B substrate. Tilted view (45°) scanning electron micrograph of vertical InAs NW array (a), HRTEM image of individual NW indicating that the [0001] direction is parallel to the longitudinal axis (b), and TEM micrograph of the hemispherical gold catalyst particle at the free end of the NW (c).

The TEM and SAED observation revealed that the NWs are wurtzite type single crystals of high quality, where the longitudinal axis is parallel to the [0001] direction. We examined several NWs, and they exhibited wurtzite structure along the whole length with only few planar defects, even at the bottleneck shaped transition between the thinner and thicker parts of the NWs. Fig. 33a and 32b show the SAED pattern and the corresponding HRTEM image taken from the middle of the NW. It should be noted that since the SAED patterns at certain orientations can be indexed considering both cubic and hexagonal structures, one could confuse zinc-blende and wurtzite type InAs (both indexing are indicated in Fig. 33a). Therefore, we have paid attention to tilt the NW in the TEM, starting from the $z = [10\bar{1}0]$ zone axis of hexagonal by 30° around the [0001] direction (this would correspond to tilting from $z = [\bar{1}12]$ around [111] in the cubic system). The so revealed SAED pattern shown in Fig. 33b can be indexed only on the base of hexagonal structure. That excludes cubic zinc-blende and confirms that my InAs NWs are of hexagonal wurtzite type.

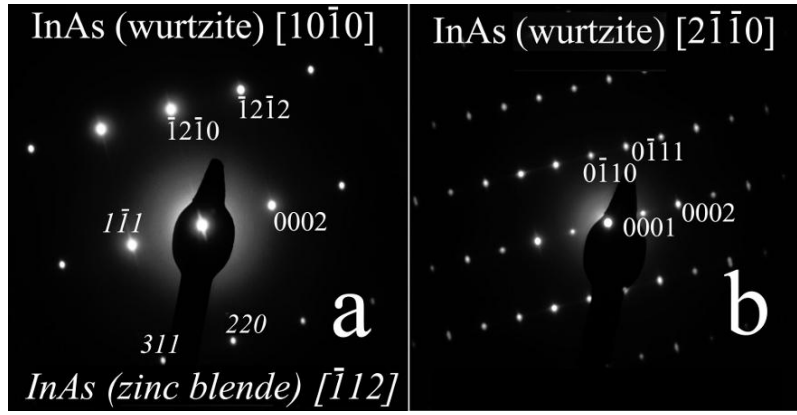


Figure 33. SAED patterns revealed during a tilting experiment in the TEM. The SAED in (a) was taken before tilting the NW. It can be indexed by both the cubic and hexagonal structures depicted by italic and normal characters, respectively. The SAED in (b) was taken after tilting the NW by 30° around its longitudinal axis. It can be indexed based exclusively on the hexagonal system. This confirms the hexagonal wurtzite structure of the InAs NWs and rules out cubic zinc-blende stacking.

5.2.2. Bending modulus of wurtzite InAs nanowires

I randomly selected five InAs NWs which were standing near the sample edge and they were mechanically tested using both static bending and dynamic excitation methods. In Table 4 the obtained NW and cantilever deflection values (y , Y) and the vertical position of the applied load (l) in the static and the resonance frequencies in the dynamic experiments (ν_{rez}) are listed with the corresponding geometrical parameters.

NW (#)	L_1 (μm)	L_2 (μm)	D_1 (nm)	D_2 (nm)	l (μm)	y (nm)	Y (nm)	ν_{rez} (kHz)
1	7.37	1.20	103	68	4.50	343	71	522.3
2	7.06	1.01	98	66	4.70	691	85	567.1
3	6.34	1.12	93	68	5.58	588	40	559.0
4	6.91	1.04	93	68	5.61	726	89	542.1
5	4.53	1.16	102	73	3.43	561	285	1138.7

Table 4. Geometrical parameters of the examined InAs NWs: length of the bottom part (L_1), length of the top part (L_2), diameter of the bottom part (D_1) and diameter of the top part (D_2). Vertical position of the applied load (l), NW deflections (y), the corresponding cantilever deflections (Y), and the resonance frequencies provided by the resonance excitation technique (ν_{rez}). Note that the NWs are built up from a thicker lower and a thinner upper segment. The measured diameter corresponds to the double of the edge of the hexagonal cross-section.

A typical normalized resonance curve obtained with NW#2 is plotted in Fig. 34a. The amplitude values in the frequency range around the resonance were determined from image

snapshots (Fig. 34b and c). The quality factor of the resonance ($Q = \nu_{rez}/\Delta\nu$, where $\Delta\nu$ is the FWHM of the resonance) is 1260, therefore the system is considerably underdamped.

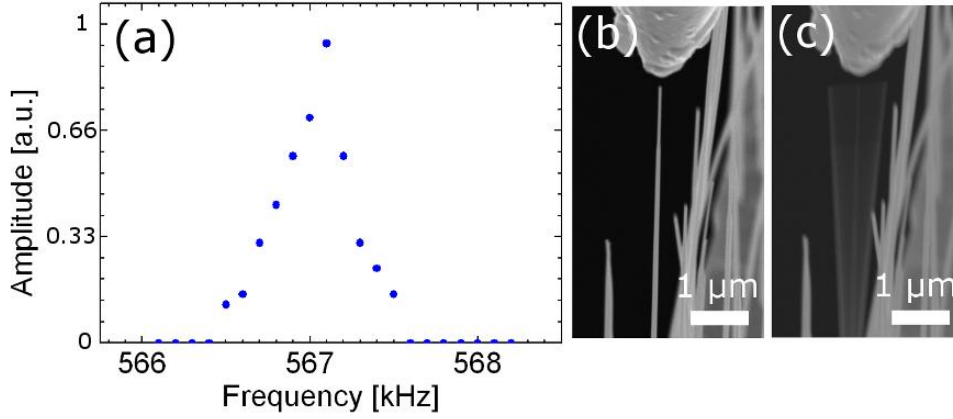


Figure 34. Resonance excitation of NW #2 using alternating electric field. Normalized amplitude resonance measured on the SEM snapshots taken around the natural resonance (a) (567.1 kHz) and the two typical SEM images recorded far from the natural resonance frequency of the NW (b) and at the resonance frequency (c). Note that the quality factor is considerably high (1260).

The bending moduli of the NWs were at first determined from the static mechanical test. The magnitude of the bending load can be calculated by multiplying the AFM cantilever deflection (Y) and its spring constant (k_{SiN})

$$F = k_{SiN}Y. \quad (15)$$

k_{SiN} was determined experimentally using a reference cantilever to avoid the calculations with the geometry and Young's modulus of silicon nitride, which spreads in a wide range in the literature. The reference beam was a rectangular Si cantilever with known spring constant ($6.81 \cdot 10^{-2}$ N/m). The cantilever to be calibrated can be used to record a force curve on a hard surface (Fig. 35a) as well as at the very end of the reference beam. The inverse slope of the contact portion of the two force curves (i.e. the deflection sensitivity) can be used to calculate the spring constant

$$k_{SiN} = k_{ref} \left(\frac{S_{ref}}{S_{hard}} - 1 \right), \quad (16)$$

where k_{ref} is the spring constant of the reference cantilever, S_{ref} and S_{hard} are the deflection sensitivities measured on the free end of the reference cantilever and on a hard surface, respectively. However, it is difficult to touch the reference beam exactly at its free end. Therefore the second force curve was recorded at a distance of ΔL from the free end (Fig. 35b) and this offset was taken into account by the following correction:

$$k_{SiN} = C_{corr} k_{ref} \left(\frac{S_{ref}}{S_{hard}} - 1 \right) \quad (17)$$

$$C_{corr} = \left(\frac{L_{beam}}{L_{beam} - \Delta L} \right)^3 \quad (18)$$

where L_{beam} is the total length of the reference beam. The force curves recorded on the hard surface (Fig. 35a) and on the reference cantilever (Fig. 35b) are plotted in Fig. 35c and d, respectively. As expected, the curves are showing hysteresis with a tilted segment corresponding to the contact portion of the tip-surface interaction. The deflection sensitivities were $S_{ref} = -13.24$ nm/a.u. and $S_{hard} = -11.21$ nm/a.u. revealing a spring constant of $2.34 \cdot 10^{-2}$ N/m.

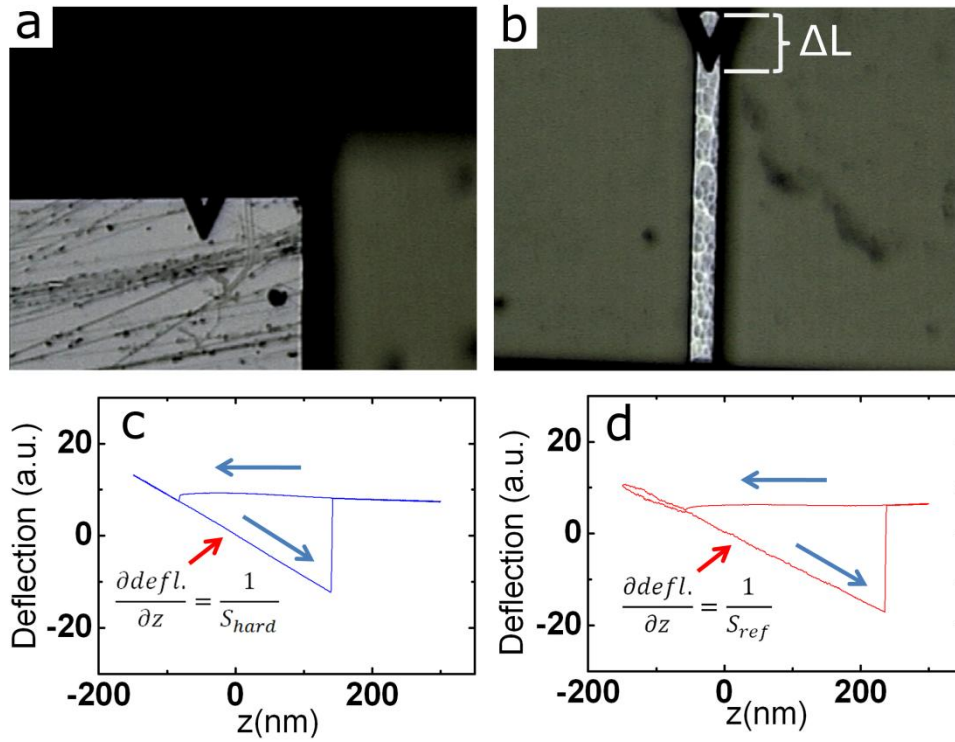


Figure 35. Snapshots taken by the CCD camera of the AFM showing the triangular nitride cantilever touching a hard silicon surface (a) and the reference cantilever at a distance of ΔL from its free end (b). The corresponding vertical stage displacement-deflection curves (c and d respectively). The slope of the tilted segments provides the deflection sensitivities. The hysteresis loops were recorded in the direction denoted by the blue arrows.

Since the bending load was applied below the thinner top part of the NW in the case of all five NWs (Fig. 31a), I calculated the BM by solving the static Euler–Bernoulli equation for a uniform cross-section [128]

$$E_{BM} = \frac{Fl^3}{3yI}, \quad (19)$$

where l is the vertical position of the applied load and I is the second moment of inertia. I can be calculated by assuming a hexagonal cross-section (Eq. 14). The obtained bending moduli range from 32 to 67 GPa, as shown in Fig. 36a (blue circles). The error bars are estimated according to Gauss's error propagation law assuming that the uncertainty of the quantities equals twice the pixel size of the corresponding SEM image. The mean BM, i.e. Young's modulus in the [0001] direction provided by the static bending test is 43.5 ± 13.6 GPa (Fig. 36b), where \pm indicates the standard deviation of the measurements.

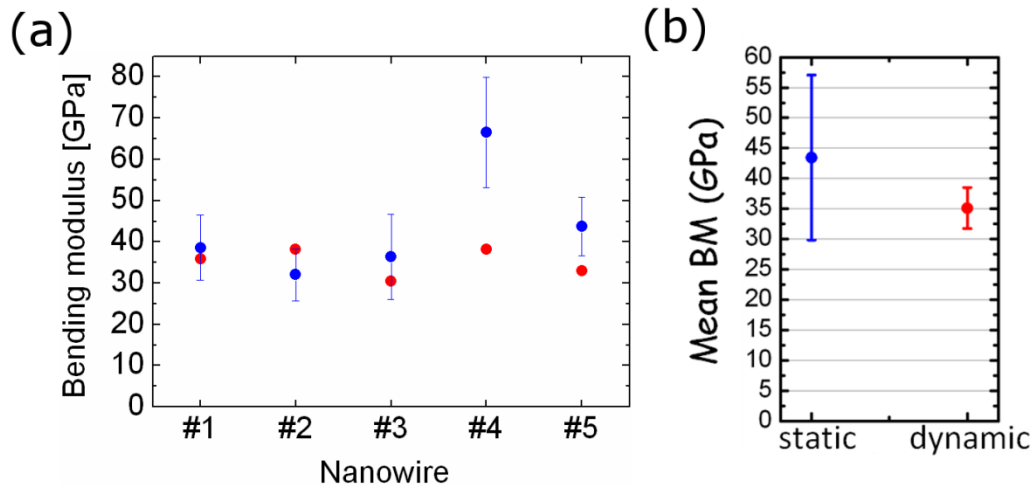


Figure 36. BM values of InAs NWs provided by the *in situ* bending experiment (blue circles with error bar) and the finite element method (red circles) considering the experimentally obtained resonance frequencies from the resonance excitation method (a). Comparison of the mean BM values provided by the two different methods with the corresponding standard deviations indicated by the error bars (b).

The BM of each NW was also determined from the resonance frequencies. Contrary to the bending experiment, here the mechanical model with uniform cross-section is not adequate, and the upper thinner part has to be also taken into account. Thus finite element method (FEM) was used where the NWs were modeled by considering their real geometry according to SEM analysis, i.e. the thicker part at the bottom, the thinner part at the top (Table 4) and the gold catalyst particle at the very end of the NWs (Fig. 32c). For the sake of simplicity the substrate beneath the NW was considered to be an InAs cuboid of 300nm x 300nm x 150 nm (Fig. 37a). Only the bottom of the substrate was anchored in the model. The Young's modulus was considered to be isotropic. The optimal mesh density was determined by gradually increasing the mesh density starting with a coarse mesh. We continued refining the mesh as long as any increasing in the mesh density had an impact on the final results (Fig. 37a). We applied a mass density of 5480 kg/m³ calculated using the lattice parameters of wurtzite InAs ($a = 4.327 \text{ \AA}$ and $c/a = 1.639$) [129]. The BM was determined by solving an inverse problem,

i.e. the resonance values were calculated by sweeping the Young's modulus in the model until a good agreement is reached with the experimental value. In accordance with the SEM experiments, we examined the first harmonic oscillations (Fig. 37b).

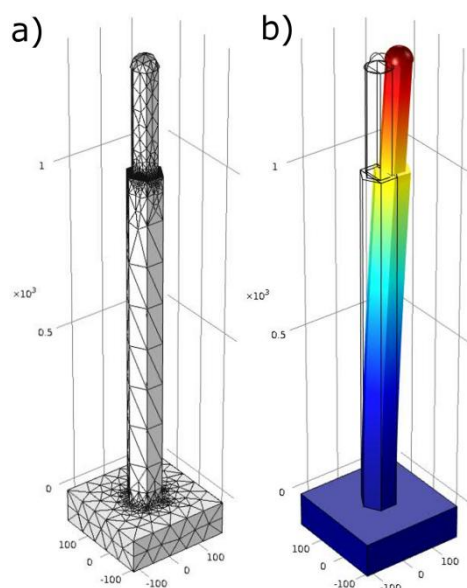


Figure 37. Model of InAs NWs for finite element calculations taking into account the real geometry: (a) illustrates the optimal mesh density, and (b) illustrates the deflection of the NW in the first harmonic mode.

The obtained bending moduli for the resonance experiments agree well with the values obtained in bending experiment (Fig. 36a) except for NW#4, where the BM from the resonance excitation technique considerably is out of the error range of the corresponding static BM. However, the degree of this discrepancy is far below the deviation of Young's modulus values of other wurtzite, e.g. ZnO NWs reported in the literature [63]. The mean BM provided by the dynamic test is 35.1 ± 3.4 GPa (Fig. 36b), where \pm indicates the standard deviation of the measurements. If we compare the mean bending modulus values provided by the two different techniques together with the corresponding standard deviations (Fig. 36b), the match is more convincing. This indicates that the resonance technique confirms the results of the static bending test. Therefore both the bending technique and Young's modulus of 43.5 GPa of wurtzite InAs NWs is validated. This value is significantly lower than Young's modulus of zinc-blende bulk InAs in the [111] direction ($E_{111} = 97$ GPa). Since wurtzite InAs does not exist in bulk form, there are no experimental data for Young's modulus on this. Only theoretical calculations exist, and they predict no difference in Young's modulus for wurtzite and zinc-blende crystals [130].

Part of the deviation from the bulk value of zinc-blende Young's modulus might be explained by softening at the surfaces [131]. Also the high quality wurtzite NWs may be the reason for the decreased BM. Both of these issues are also addressed and in agreement with data presented by Lexholm *et al.* [124]. Park *et al.* has summarized mechanical properties for different types of NWs and concludes that there is a significant discrepancy between theoretical and experimental values of Young's modulus [132]. Besides, it is also seen from the resonance in Fig. 34a that the high quality wurtzite NWs are suitable for ultra sensitive mass measurement by attaching a small particle to the free end of the NW and measuring the frequency shift. The calculated sensitivity of the vibrating cantilever balance at the first harmonic mode can be estimated by the following equation [66]:

$$\Delta M_P \approx \frac{6}{\beta_1^4 Q} M_0 \quad (20)$$

where M_0 is the mass of the NW. For NW#2 with $M_0 = 257$ fg and $Q = 1260$, the lowest estimated mass which can be measured is 0.099 fg.

Although as it turned out the two *in situ* methods lead to the very similar result both of them have advantages and disadvantages. While with the resonant excitation only high aspect ratio NWs can be characterized the static bending technique can be applied even for low aspect ratio (<20) and rigid NWs and NRs. Furthermore the latter method does not depend on the electrical properties of the NWs to be measured. Moreover, with the bending technique it is also possible to investigate the change of the Young's modulus along the axis of the NW by taking a series of bending experiments at different vertical load positions. On the other hand for homogenous, high aspect ratio NWs the resonant method can be easier since it is no need to carefully calibrate and prepare the probe. Moreover, the resonance excitation technique can provide the quality factor of the oscillating NW system.

In conclusion, I have presented a general combined method for measuring the BM of individual cantilevered nanostructures applying two nanomanipulator arms in the SEM. One is responsible for a static bending test, and the other one is used to electrically excite mechanical oscillations. The dynamic experiment validates the result of the static bending test. Up to my knowledge this is the first time, that the two techniques are used on the same individual nanostructures to cross-confirm the results. Moreover, the mechanical properties of wurtzite InAs NWs have been characterized by this method. Young's modulus in the [0001] direction was measured to be 43.5 ± 13.6 GPa by the static method, and 35.1 ± 3.4 GPa by the

dynamic method, which are significantly lower, than that of cubic bulk InAs in the [111] direction. The high resonance quality factor (1260) of the wurtzite InAs NWs makes the material a promising candidate for subfemtogram mass detectors.

6. Mechanical characterization of epitaxially grown ZnO nanorods

In this chapter, I apply the validated static bending test in order to mechanically characterize low aspect ratio, rigid ZnO NRs. In contrast with the references [21, 46, 51, 59, 62-63, 65-70], I performed my measurements on highly ordered ZnO NRs perpendicularly standing on their substrate. Up to my knowledge this thesis (and the corresponding own publication [T4]) is the first work on the mechanical characterization of wet chemically grown vertical ZnO NRs.

6.1. Experimental subsection

The NRs arranged in a triangular lattice were synthesized by selective area wet chemical growth method onto the surface of a c-axis oriented (Zn-polar), hydrothermal ZnO single crystal (CrysTec GmbH) (see subsection 4.1.). In order to make the NRs accessible for the AFM cantilever the ZnO wafer was cleaved across the patterned area (Fig. 38d). Hence, I obtained perpendicularly standing NRs at the edge of the substrate.

The bending experiments were carried out in SEM by a soft silicon AFM tip (Fig. 38a-b) (MikroMasch CSC17/Cr-Au), which was mounted on a nanomanipulator arm (see subsection 5.1.). Prior to testing, the resonance frequency of the cantilever (f) was measured by our scanning probe microscope. Contrary to the case of silicon-nitride cantilevers, here the calibration is much easier, since silicon cantilevers are manufactured by wet etching from the single crystalline wafer and therefore their crystallographic orientation and hence Young's modulus is well known. One only has to determine the dimensions (by SEM) and the resonance frequency (by AFM) of the cantilever, and the spring constant can be analytically calculated with high confidence. In order to ensure a permanent contact between the probe and the NR during the bending test and to avoid slipping from the edges, a U-shaped incision was etched by focused ion beam at the end of the tip (Fig. 38c). The coarse positioning of the AFM tip toward the sample was done with the robotic arm, while the fine positioning as well as the manipulation of the NRs was achieved by moving the sample with the stage. The schematic of the bending experiment is shown in Fig. 31a-b. In my systematic characterization carried out on six individual NRs, the bending load was applied in the $\langle 11\bar{2}0 \rangle$ crystallographic direction, i.e. perpendicular to the vertical axis of the NR and parallel to the long symmetry axis of the hexagonal cross-section. In order to investigate the

effect of the load direction, the bending experiment, in one case, was also done in the $\langle 10\bar{1}0 \rangle$ direction, i.e. perpendicular to the long symmetry axis of the hexagon (Fig. 39c inset). As in the case of InAs NWs in subsection 5.1., stress was applied via moving the stage and hence the NR towards the tip and thus deflecting the loading cantilever. Simultaneously, two snapshots were recorded at each bending test, one in stressed and the other one in relaxed state. By overlapping the two snapshots both NR and tip deflections (y and Y) can be determined by image analysis.

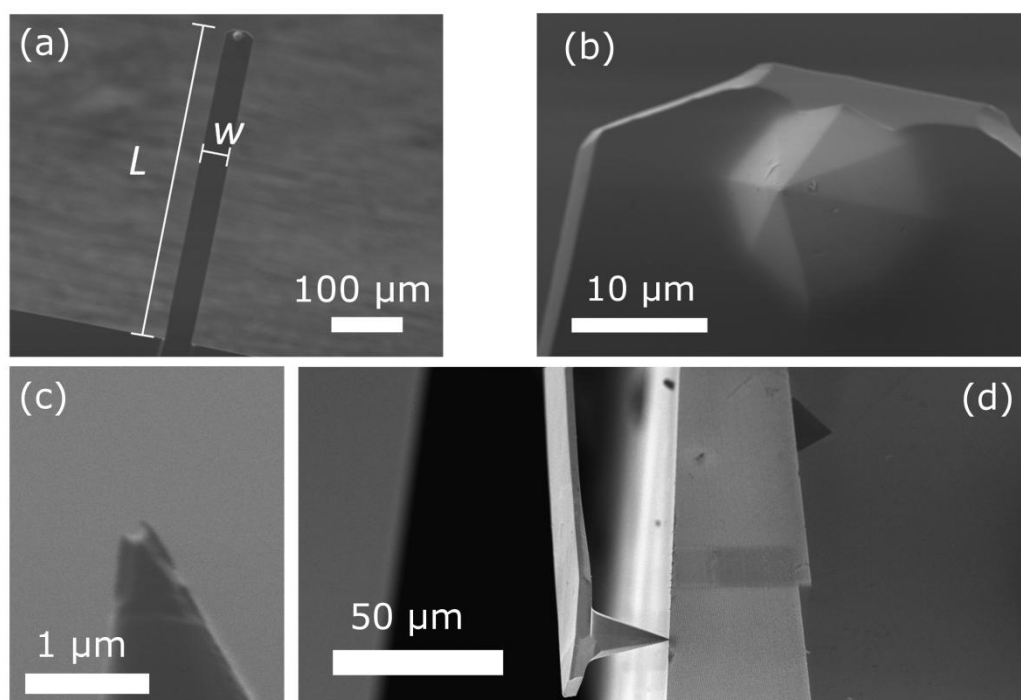


Figure 38. SEM micrographs of the MikroMasch CSC17/Cr-Au AFM cantilever in lower magnification (a) and in higher magnification (b) showing the pyramidal tip at the end. A U-shaped incision etched by FIB at the edge of the tip (c) to avoid slipping of the NR during manipulation. Lower magnification SEM image of the cantilever and tip touching the array of vertical ZnO NRs at the edge of the cleaved wafer (d).

6.2. Results and discussion

According to the SEM observation the ZnO NRs are arranged in the desired lattice (Fig. 39a). Each NR is c-axis aligned and consists of two parts: a shaft at the bottom, which was formed by filling the hole in the PMMA layer and a longer upper part having hexagonal cross-section (Fig. 39b), which was formed “naturally” during the chemical growth. The hexagonal cross-sections are collectively aligned according to the crystal orientation of the substrate. The length of the NRs varied in the range of 1.3–1.5 μm , while the Feret’s diameter of the (0001) hexagonal top face is 105 ± 8 nm.

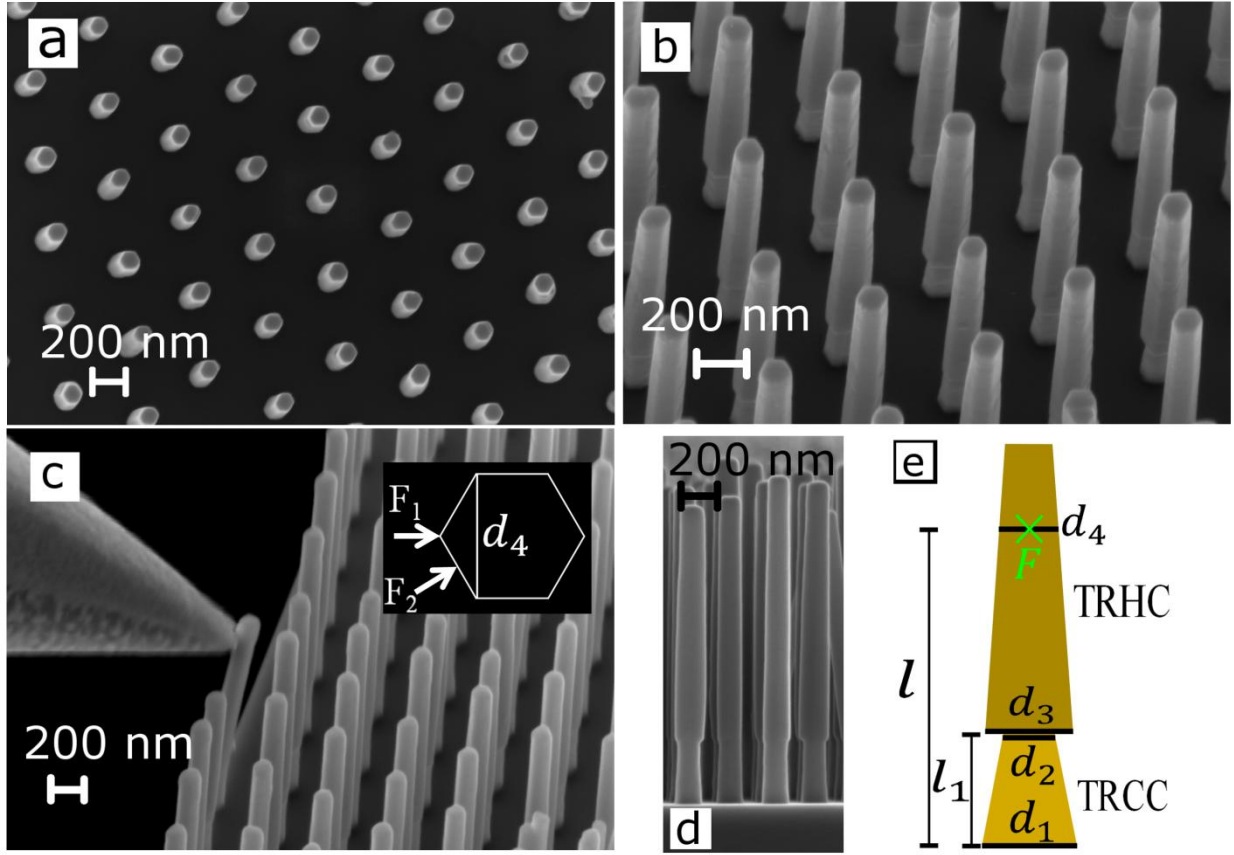


Figure 39. Top and perspective view scanning electron micrographs of the epitaxially grown NR array (a and b). Randomly selected NRs standing at the cleaved edge were bent by a calibrated AFM tip (c) in the $\langle 11\bar{2}0 \rangle$ (arrow marked by F_1) and $\langle 10\bar{1}0 \rangle$ (arrow marked by F_2) crystallographic directions (c inset). Side-view image taken on the NRs (d) shows the non-uniform cross-section along the vertical axis. During the calculation of the BM the NR geometry is divided into a lower truncated circular and in an upper truncated hexagonal cone (TRCC and TRHC) (e).

During the NR bending test I found that even strongly deflected NRs returned back to their original position when released. Therefore all deflections measured in this work can be assumed to be purely elastic. In a certain static bent state (Fig. 39c) the two spring forces of AFM cantilever and of ZnO NR are in equilibrium; therefore, it can be calculated by multiplying the AFM cantilever deflection (Y) and its spring constant (k_{Si})

$$F = k_{Si}Y. \quad (21)$$

Although k_{Si} can theoretically be calculated purely from the geometrical parameters and from the Young's modulus of Si (E_{Si}) I followed instead the method suggested by Cleveland *et al.* [133] to eliminate the purely measurable cantilever thickness value

$$k \approx \frac{2\pi^3 w (f_0 L \sqrt{\rho_{Si}})^3}{\sqrt{E_{Si}}}, \quad (22)$$

where w , f_0 , L , and ρ_{Si} are the width, unloaded resonant frequency, length, and mass density of the rectangular Si cantilever, respectively. The geometrical parameters of the cantilever were estimated from SEM images (Fig. 38a). The obtained k_{Si} value is $9.33 \cdot 10^{-2}$ N/m, while the bending force value in each experiment is shown in Table 5.

NR (#)	F (nN)	d_1 (nm)	d_2 (nm)	d_3 (nm)	d_4 (nm)	l_1 (nm)	l (nm)	NR defl. (nm)	E_{BM} (Gpa)
1	61	154	121	162	133	376	1358	58	40.8
	51	154	121	162	129	376	1463	74	33.1
	50	154	121	162	125	376	1531	75	36.7
2	83	155	135	155	136	336	1364	86	32.8
	78	155	135	155	133	336	1430	69	44.4
	68	155	135	155	130	336	1475	80	36.8
3	50	152	124	128	117	294	1154	42	37.1
	40	152	124	128	120	294	1109	38	28.6
4	53	152	121	140	126	337	1281	65	31.0
	46	152	121	140	126	337	1266	73	23.2
5	61	158	137	140	131	318	1328	101	20.9
	56	158	137	140	128	318	1361	104	20.3
6	61	157	139	143	125	380	1270	54	33.2
Average									32.2 ± 7.4

Table 5. Summary of the bending experiments. The columns from left to the right denote: NR number (NR), load (F), lower (d_1) and upper (d_2) diameter of the truncated circular cone, lower (d_3) and upper projected width (d_4) of the considered hexagonal cone, height of the truncated circular cone (l_1), point of the applied force (l), NR deflection ($NR\ defl.$) and calculated BM (E_{BM}) using equation (28).

The BM of a perpendicularly standing beam fixed at the bottom and pushed by a lateral force is most commonly calculated by solving the static Euler–Bernoulli equation on a uniform cross-section (Eq. 19). Here the second moment of inertia can be calculated by assuming either hexagonal (Eq. 14) or circular cross-section

$$I_{circle} = \frac{\pi r^4}{4}, \quad (23)$$

where r is the radius of the circle. However, as shown in Fig. 39d the change of the diameter along the vertical axis is obvious, which can cause a multiplied uncertainty in BM because of

the fourth-power dependence (Eqs. 14 and 23). Therefore, in case of as prepared vertical NRs the implementation of a non-uniform beam model is essential. In the specific case of elastic beams Castigliano's theorem says that the derivative of the total strain energy (U) of an elastic beam with respect to the load (F_i) is equal to the deflection (δ_i) corresponding to the load [128]:

$$\delta_i = \frac{\partial U}{\partial F_i}. \quad (24)$$

Assuming that the strain energy due to traverse shear loading is negligible, the strain energy resulting from bending of the NR can be calculated as follows:

$$U = \int_0^l \frac{M^2}{2EI} dx, \quad (25)$$

where the x axis runs along the NW with origin fixed at the height of the applied load, and $M=Fx$ is the internal bending moment, which is a function of x . Therefore the deflection of NR can be calculated as follows:

$$y = \frac{\partial U}{\partial F} = \frac{F}{E} \int_0^l \frac{x^2}{I} dx. \quad (26)$$

Or, if we fix the origin of the coordinate system at the bottom of the NR we can also write:

$$y = \frac{F}{E} \int_0^l \frac{(l-x)^2}{I} dx. \quad (27)$$

To describe the practical geometry, the ~300 nm high bottleneck-shaped part at the bottom of the nanocrystals can be approximated as a truncated right circular cone (TRCC), while the upper part as a truncated right hexagonal cone (TRHC) (Fig. 39d–e). Hence, using Eqs. (14), (23), and (27) the BM can be expressed by the following form:

$$E_{BM} = \frac{kY}{y} \left\{ \frac{4}{\pi} \int_0^{l_1} \frac{(l-x)^2}{\left[\frac{1}{2} \left(d_1 - \frac{(d_1-d_2)}{l_1} x \right) \right]^4} dx + \frac{16}{5\sqrt{3}} \int_{l_1}^l \frac{(l-x)^2}{\left[\frac{1}{\sqrt{3}} \left(d_3 - \frac{(d_3-d_4)}{l-l_1} (x-l_1) \right) \right]^4} dx \right\}, \quad (28)$$

where d_1, d_2, l_1, d_3, d_4 are the lower and upper diameter of the TRCC, the height of TRCC, the $\langle 11\bar{2}0 \rangle$ projected width ($\sqrt{3}a$) at the bottom and at the top of the considered TRHC, respectively. These parameters are determined from side view SEM images captured after each bending test by setting the electron beam parallel to the direction of the load (e.g. Fig.

39d). I examined six NRs under different bending states. Detailed geometrical parameters and the obtained BM values are summarized in Table 5.

The obtained bending moduli range from 20 to 44 GPa. The average value of 32.2 ± 7.4 GPa is significantly lower than the Young's modulus of bulk ZnO in the [0001] direction (140 GPa) [72]. The strong discrepancy is usually attributed to different effects such as surface stress or electromechanical coupling [63]. To answer this question a further systematic investigation is required. However, the modulus reported in this chapter is similar to the one which was measured by Manoharan *et al.* [63] (44 GPa) by applying also *in situ* static bending experiment. For comparison, the BM was calculated in the simpler way as well, i.e. by assuming a beam with uniform circular cross-section (Eq. 19) instead of the two-part mechanical model. The homogeneous second moment of inertia was estimated by Eq. (23), in which the half of the corresponding d_l diameter (at the bottom of the TRCC) was considered as the radius of the circle in the case of each NR. The so calculated mean BM of 24.8 ± 7.1 GPa is lower than that provided by the more sophisticated model, therefore the changing cross-section along the vertical axis cannot be neglected and the non-uniform beam model is essential.

The comparative bending tests carried out on the same NR along $\langle 11\bar{2}0 \rangle$ and $\langle 10\bar{1}0 \rangle$ directions (Fig. 39c inset) could not reveal significant load direction dependence. The obtained BM values calculated by Eq. (28) were $E_{BM\langle 11\bar{2}0 \rangle} = 29 \pm 5$ GPa and $E_{BM\langle 10\bar{1}0 \rangle} = 34 \pm 5$ GPa. Note, that the second moment of inertia for hexagonal cross-section (14) is valid for both horizontal and vertical axis through the centroid, therefore Eq. (28) is also valid for both load directions.

In conclusion, I have performed a well controlled and validated static experiment to determine the BM of low aspect ratio homoepitaxially grown vertical ZnO NRs. In the mechanical test the ZnO NRs were deformed along the $\langle 11\bar{2}0 \rangle$ direction by a calibrated AFM tip in an SEM chamber. I proposed a non-uniform beam model for the BM calculation, which takes into the account the changing cross-section of the NR along the vertical axis. I found that the average value of 32.2 ± 7.4 GPa is significantly higher than the calculated one which assumes a homogeneous circular cross-section along the whole length (24.8 ± 7.1 GPa). The demonstrated technique can be later also a powerful tool for the calibration of the proposed integrated nanoforce sensor. Moreover in the future I am also planning to carry out fracture tests by the same manner in order to determine the fracture strength of the NRs.

7. Towards the integrated nanomechanical sensor

In this final chapter of my results I will briefly describe the first steps towards the realization of the actual integrated NEMS device illustrating the future perspectives.

7.1. Synthesis of individual vertical ZnO NWs

As it was shown in chapter 4, large arrays of vertically aligned ZnO NRs/NWs can be fairly easily made on different substrates compatible with traditional Si technology by our selective area wet chemical growth method. However, here an important question has to be answered: can one synthesize freestanding individual NRs with similar dimensions? One of the most important drawbacks of our method is that the growth of such NRs is troublesome. As we saw the NWs are grown through cylindrical nucleation windows opened in the PMMA, which are arranged in a lattice with low spacing (~500-1000 nm) between the holes. In the case of NWs grown on BULK the geometry can be considered to be homogeneous far from the edge of the array (from at least the 5th-6th row) (Fig. 40b), however, it differs significantly closed to the unpatterned region (Fig. 40a). Namely they become considerably longer and the hexagonal upper part (TRHC) formed naturally above the PMMA layer becomes fairly thick. This is due to the different precursor consumption rates in the vicinity of the given NWs, as their growth from solution is a mass transport limited process [134]. At the edge of the array the number of surrounding nucleation windows (at the early stage of growth) or NWs (at the latter stage of growth) is low leading to higher local precursor supplement/consumption ratio. Obviously in the middle of the array the supplement/consumption ratio is much lower. Note, that the thicker shaft in Fig. 40b compared to Fig. 40a can be explained by the proximity effect of e-beam lithography. Proximity effect is a phenomenon when the electron scattering in resist and substrate leads to an undesired influence in the regions adjacent to those exposed by the electron beam. This causes e.g. a widening of the exposure region when the features to be exposed are densely arranged.

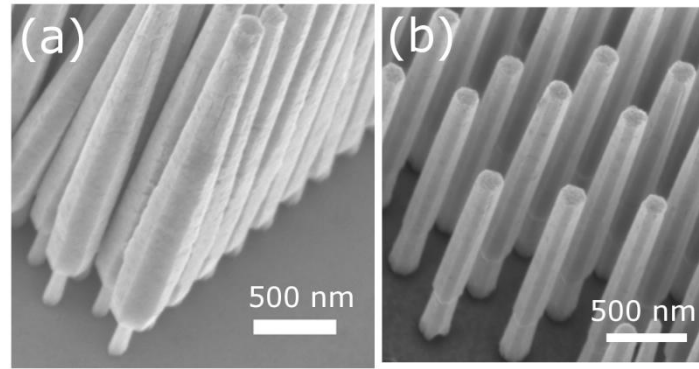


Figure 40. ZnO NWs grown on BULK at the edge of the array (a), and in the middle of the array (b).

Therefore the growth from a single nucleation hole under identical conditions would lead to a long and thick pillar with thin shaft at the bottom (compared to the upper part). From the point of view of the proposed nanoforce sensor this geometry is not beneficial, since an unacceptably high mechanical stress can arise at the connection point between the shaft and the upper part upon bending.

7.1.1. Experimental

To overcome this problem I suggest the following. Let us define precursor concentration controlling windows (PCCWs) closed to the nucleation window as can be schematically seen in Fig. 41a. There is a single cylindrical hole developed in the PMMA and two square shaped PCCWs are defined on either side at a distance of 1.5 μm . As substrate, I have chosen PLD/SiO₂/Si, since the final device would also apply this layer structure. The growth conditions of the NW in the solution having a concentration of 4mM were similar to that shown in Fig. 19e, however, the slow cooling step was skipped and after the plateau the sample was immediately removed from the nutrient solution. A series of NWs were synthesized with gradually increasing dimension of PCCW (t parameter in Fig. 41a), however, the edge of the square was always kept at 1.5 μm from the hole. The resulting NWs were examined by FE-SEM.

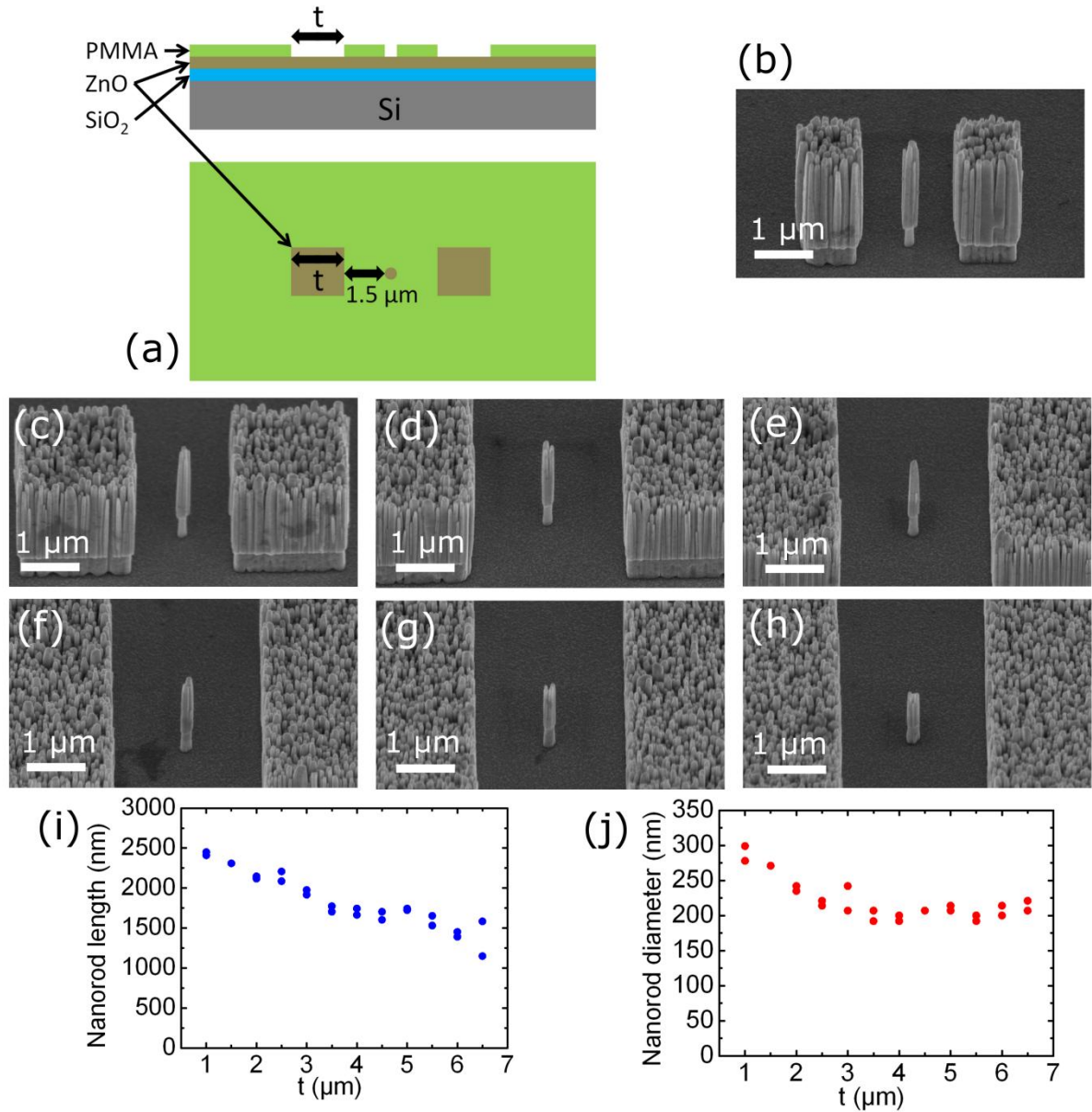


Figure 41. Schematic of the PCCWs (a). The geometry of the resulting NW can be tuned by changing the dimension (t) of the window. SEM micrographs of the NWs grown by the support of PCCWs (b: $t = 1 \mu\text{m}$; c: $t = 2 \mu\text{m}$; d: $t = 3 \mu\text{m}$; e: $t = 4 \mu\text{m}$; f: $t = 5 \mu\text{m}$; g: $t = 6 \mu\text{m}$; h: $t = 6.5 \mu\text{m}$). Plots of NW length and bottom diameter of the NW's top part (formed above the level of PMMA) as the function of the PCCW's dimension (i and j, respectively).

7.1.2. Results and discussion

The SEM images of the obtained NWs are shown in Fig. 41b-h (b: $t = 1 \mu\text{m}$; c: $t = 2 \mu\text{m}$; d: $t = 3 \mu\text{m}$; e: $t = 4 \mu\text{m}$; f: $t = 5 \mu\text{m}$; g: $t = 6 \mu\text{m}$; h: $t = 6.5 \mu\text{m}$). It can be seen that the geometry of the NW can be sufficiently tuned by changing the dimension (t) of the PCCW. In the case of $t = 1 \mu\text{m}$ the whole length and the bottom diameter of the top part formed above the level of PMMA (2.45 μm and 280 nm, respectively) is considerably higher than those

corresponding to $t = 6.5 \mu\text{m}$ ($1.15 \mu\text{m}$ and 210 nm , respectively). Fig. 41i and j show the measured NW length and diameter values as the function of t . From the point of view of my proposed device it can be concluded, that the PCCW is a powerful tool to tune the dimensions of individual NWs. If we consider the schematic of the device (Fig. 17), one can easily find bare ZnO surfaces where the PCCWs can be defined.

7.2. 1D mechanically gated ZnO thin film transistor

As it was mentioned in chapter 3, the substrate of the proposed device would be a highly p-doped Si wafer, which could serve as a bottom gate. Similarly to the case of NW bio- and gas sensors the bottom gate can be very beneficial e.g. for refreshing and tuning the sensitivity of the device. For the sake of simplicity let us fabricate the first proof-of-concept (PoC) device on c-sapphire. As we saw in subsection 4.2.1., c-sapphire substrate supports the growth of regular single crystalline NRs in contrast with the multiple NWs on ZnO/SiO₂/Si. Let us now find out whether my wet chemically grown vertical ZnO NRs can transform mechanical deformation into electrical signal.

7.2.1. Experimental

The schematic of the 1D PoC device is shown in Fig. 42. A thin ZnO stripe (width: $3.1 \mu\text{m}$) was etched in the mixture of HCl (5 ml) and H₂O (300 ml) from a homoepitaxial ZnO layer (thickness: 25 nm, sheet resistance: $52 \text{ k}\Omega/\square$) above the insulating c-sapphire. The ZnO layer was deposited by plasma assisted molecular beam epitaxy (MBE) at VCU (Richmond, Virginia, USA). Afterwards, two metal electrodes (Ti 30 nm/Au 70 nm) were deposited covering the two ends of the channel. The channel length between the metallization was $3.6 \mu\text{m}$. The structures were defined by a laser pattern generator using photoresist (Heidelberg Instruments Micro-PG Pattern Generator). In order to make good Ohmic contacts and minimize the resistance of the ZnO-metal junctions the sample was annealed in a two-step rapid thermal annealing (RTA) process in N₂ atmosphere ($375 \text{ }^\circ\text{C}$, 20s + $500 \text{ }^\circ\text{C}$, 10s). An array of vertical ZnO NRs were grown on the top of the ZnO channel as described in subsection 4.1. However, an important difference was here that due to the small dimensions of the array the growth was interrupted after 2 hours to avoid the formation of too thick pillars. Before electromechanical test the metal electrodes were contacted by wire bonding.

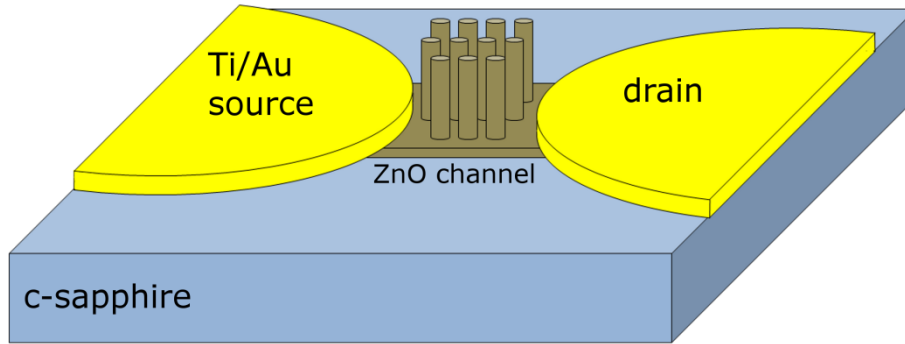


Figure 42. Schematic of the 1D PoC device. A ZnO conducting channel with vertical ZnO NRs on the top is located between two electrodes.

The obtained NRs were examined by FE-SEM. The electromechanical behavior of the device in response to NR bending was studied by AFM. The sample was mounted inside the AFM and a constant bias of 0.2 V was applied between the source and drain electrodes. The voltage was applied by the source-meter unit (c-unit) of the microscope by which the resulting current was also monitored. The schematic arrangement of the electromechanical test is shown in Fig. 43. Originally the c-unit is dedicated for measuring the conductance map of the sample's surface by a conductive probe, however, external resistors can be also characterized by that. In order to visualize the lateral and normal forces acting between the probe and the NRs the lateral (V_{lat}) and normal (V_{norm}) output of the PSPD were recorded. The NR bending was performed by the following way. The AFM stage with the NR array was scanned beneath the probe under deactivated feedback loop in a square area and the distance between the perpendicularly standing NRs and the edge of the probe was gradually decreased until V_{lat} and V_{norm} signals were detected. In order to ensure that the deflection of the NRs is significantly higher than the lateral torsion of the tip, instead of a common contact probe I have chosen a medium soft probe (BudgetSensors Multi75-G) having a nominal normal stiffness of 3 N/m and hence higher lateral stiffness compared to typical contact tips. The scan direction was perpendicular to the longitudinal axis of the cantilever. When the top of the rods was reached, as indicated by the appearance of both signals, the approach was stopped. Hence the NRs were bent at their free end by the apex of the probe as shown schematically in Fig. 43. V_{lat} and V_{norm} images in constant height mode, i.e. without feedback, were recorded simultaneously together with the current flowing through the channel. The probe was electrically insulated from the microscope.

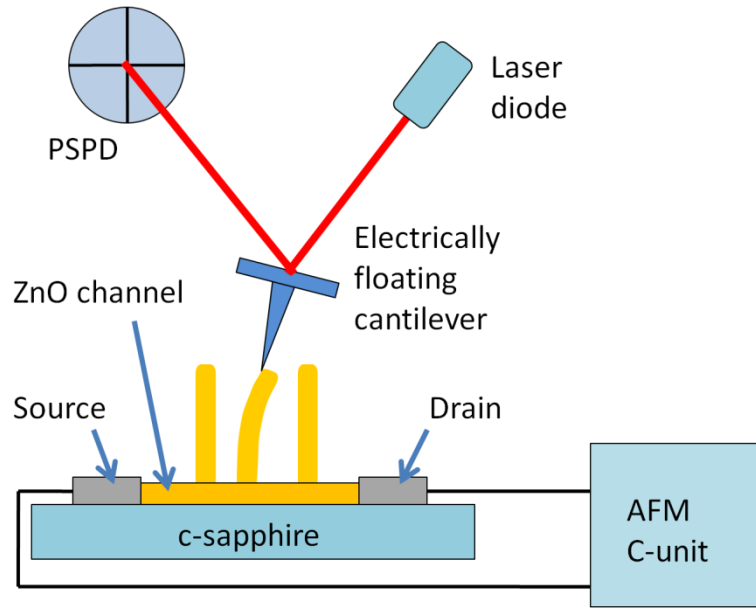


Figure 43. Schematic of the measurement arrangement for the PoC device's electromechanical characterization. The NRs are bent by an AFM probe while the current flowing through the ZnO channel is monitored.

7.2.2. Results and discussion

Fig. 44a and b show the tapping AFM and the SEM image of the NR array standing on the ZnO conducting channel. The typical length and diameter are $\sim 1.2 \mu\text{m}$ and $\sim 300 \text{ nm}$, respectively.

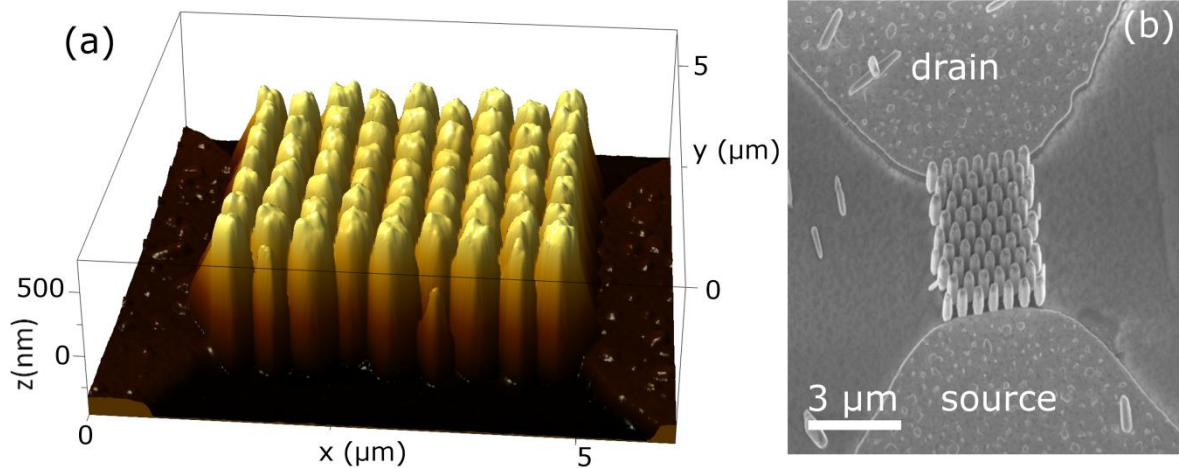


Figure 44. Tapping mode AFM image of the NR array on the ZnO conducting channel lying between two Ti/Au electrodes (a). The corresponding SEM micrograph (b) (rotated by $\sim 90^\circ$ compared to (a)).

The current-voltage curve recorded by the c-unit (Fig. 45d) shows that the device has excellent linear characteristic with a resistance of $59.7 \text{ k}\Omega$. Fig. 45a and b show the V_{lat} and V_{norm} maps recorded after reaching the appropriate height for the bending experiment. The

appeared trapezoids correspond to elastic bending whereas the triangles indicate fracture. It can be seen that several fractures occurred most likely due to the especially low aspect ratio of the NRs. Nevertheless, a slight resistivity modulation of the channel was observed in given NR positions as indicated by black negative peaks on the source-drain current map (Fig. 45c). The cross-section of the current map along the green dashed line plotted in Fig. 45e indicates that the depth of the negative peaks is about ~ 10 nA, i.e. about three thousandth of the background.

I think higher signal could not be achieved by this arrangement, since we either approached or exceeded the fracture strength at the bottom of the NRs. However, by lowering the channel width and thus increasing the effected cross-sectional area in the channel a significantly enhanced relative signal can be expected. Indeed, according to FEM calculation shown in Fig. 15, the cross-sectional footprint of the mechanically and electromechanically affected area is rather limited beneath the bent NR. In this perspective, the ultimate design is a NR-diameter-wide channel carrying a single NR on its surface. The realization of such device is technologically challenging but feasible with the available infrastructure at MFA.

Nevertheless, the origin of the signal is not clear yet and cannot be explained entirely by the above described piezoelectric gated mechanism, since the negative peaks, in each case, occurred at NRs standing directly next to the metal electrode which suggests contact governed conduction mechanism. For a deeper understanding, a systematic electromechanical investigation using different channel geometries is essential. However, the goal of this chapter, i.e. to demonstrate the applicability of the wet chemically grown vertical ZnO NRs as building blocks of novel NEMS devices was achieved and the latter aspects are out of the scope of this thesis.

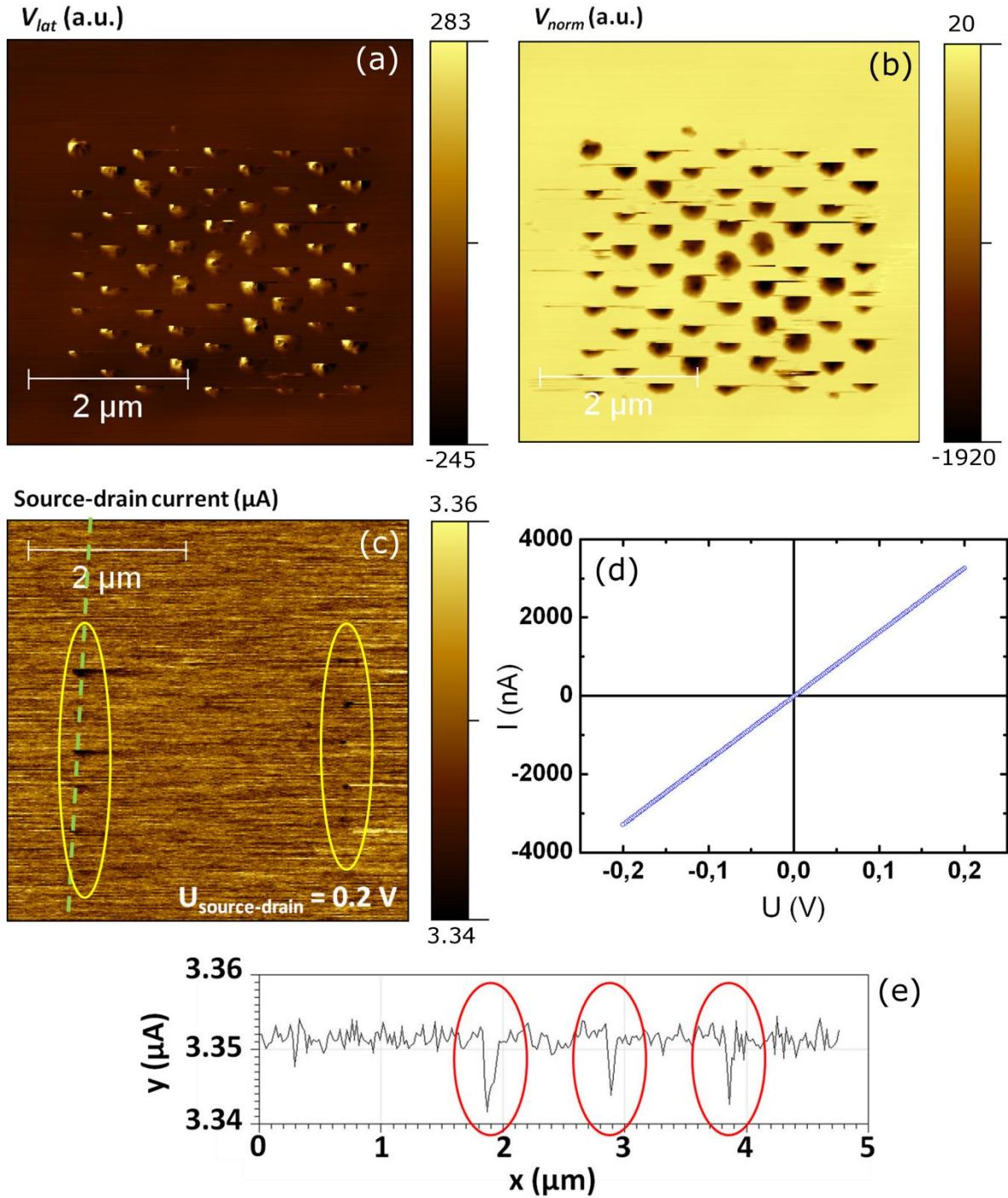


Figure 45. Lateral (a) and normal (b) output of the AFM's position sensitive photo detector recorded during NR bending in constant height mode. The corresponding source-drain current of the PoC device (c). The negative current peaks on the latter indicate the slight resistivity modulation of the channel as a result of bending. Current-voltage characteristic of the device recorded by the c-unit of the AFM (d). Cross-section of the source-drain current map along the green dashed line (e).

8. Summary

In this thesis I have proposed the design of an integrated nanoelectromechanical sensor based on the bending of an individual vertical ZnO NW. As the first steps of the realization of such a device I have explored the preparation of wet chemically grown c-axis aligned ZnO NWs on different substrates and the mechanical characterization of vertical InAs and ZnO NWs. The results of my research can be summarized in two main parts.

I have investigated the impact of various ZnO seed layers on the alignment and geometry of wet chemically grown vertical ZnO NW arrays. The NWs were seeded at nucleation windows which were patterned in poly(methyl methacrylate)-coated ZnO surfaces using electron beam lithography. This growth approach was shown to have the potential for low-cost and low-temperature fabrication of regular, highly aligned, and transparent NW arrays with tunable conductivities on cheap substrates with precise engineering of the NW dimensions and positioning. The compared ZnO templates included a single crystal ZnO substrate, epitaxial films on c-sapphire, and GaN/c-sapphire substrates, and polycrystalline films on Si(111), Si(100), thermal SiO₂, and Pt/c-sapphire. SEM, AFM, XRD and TEM analysis revealed that the alignment, crystal structure, and geometry of the NW arrays were dictated by the crystal structure of the underlying ZnO, while the influence of the surface roughness was negligible. Thus, the choice of seed layer crystallinity gives control over the NW form, alignment, and in-plane crystallographic orientation. In particular, hydrothermal ZnO substrates, epitaxial ZnO layers grown on c-sapphire by PLD and epitaxial ZnO layers grown on GaN/c-sapphire by ALD gave similar NW arrays with very regular form, strong vertical alignment, and a common relative orientation of their hexagonal crystal facets in the surface plane. As it was pointed out by PFM the wet chemically grown NRs on PLD ZnO seed layer showed high piezoelectric constant (8.4 ± 1.7 pm/V) which can be beneficial for nanomechanical sensors and energy harvesting devices. It was also shown, that definite improvement in the vertical alignment of the NWs can be achieved by additional heat treatment of seed layers.

I have examined the mechanical properties of high aspect ratio vertical InAs NWs in a SEM equipped with two nanomanipulators. One, equipped with a calibrated AFM probe, was used for *in situ* static bending of single NWs along the $\langle 11\bar{2}0 \rangle$ crystallographic direction. The other one was equipped with a tungsten tip for dynamic resonance excitation of the same NWs. This setup enabled a direct comparison between the two techniques. I have shown that the two *in situ* methods lead to the very similar result hence cross-confirming each other. I

determined the BM value of InAs NWs with a hexagonal wurtzite crystal structure, which was found to $BM = 43.5 \pm 13.6$ GPa by the static method, and $BM = 35.1 \pm 3.4$ GPa by the dynamic method. These values are significantly lower than previously reported for both cubic zinc blende InAs bulk crystals and InAs NWs. Besides, due to their high resonance quality factor ($Q > 1200$), I have shown that the wurtzite InAs NWs are a promising candidate for sub-femtogram mass detectors. Due to their low aspect ratio, the dynamic resonance excitation of my wet chemically grown ZnO NRs would be troublesome. Therefore I applied the validated static bending test for the mechanical exploration thereof. The NRs, which are naturally affixed onto the substrate, were bent at their free end along $\langle 11\bar{2}0 \rangle$ and $\langle 10\bar{1}0 \rangle$ crystallographic directions. The typical deflections, caused by $\sim 40\text{--}60$ nN lateral loads, fall in the range of $\sim 50\text{--}100$ nm. In order to take into account the non-uniform cross-section along the vertical axis, I proposed a two-part mechanical model, which is built up from a lower truncated circular, and an upper truncated hexagonal cone. The obtained BM is 32.2 ± 7.4 GPa, which is significantly lower than that of the bulk ZnO (140 GPa) and higher than the value of 24.8 ± 7.1 GPa calculated by assuming the homogeneous model of a right circular prism. The demonstrated static bending is a perfect tool for the examination of the fracture strength of the NRs and the electromechanical testing of the proposed integrated NEMS device.

Illustrating the future perspectives, I fabricated and electromechanically tested a mechanically gated ZnO thin film transistor on c-sapphire, as a proof-of-concept device. I obtained a slight resistivity modulation (3 %) of the conducting channel as a result of NR bending carried out in AFM. Hence it was proved, that electromechanical response can be expected from the proposed integrated device. However, the geometry optimization and the further systematic electromechanical investigation are beyond the scope of this work.

9. Thesis highlights

1. Through the examination of seven ZnO seed layers of different quality I have shown that highly aligned, wet chemically grown ZnO nanowires with tunable geometry can be synthesized by choosing the appropriate ZnO seed layer and using e-beam lithography for positioning. Therefore the nanowires can operate as building blocks of different integrated nano- and optoelectronic devices [T1].
2. I have shown by quantitative X-ray diffraction and transmission electron microscopy analysis that the crystal structure and alignment of the ZnO nanowires is determined by the dispersion in the crystallographic orientation and the crystal structure of the crystallites in the seed layer [T1].
3. I have determined for the first time by piezoresponse force microscopy the d_{33} piezoelectric constant (corresponding to the [0001] crystallographic direction) of ZnO nanorods positioned by lithography and grown by the wet chemical method. Due to the considerably high obtained piezoelectric constant of 8.4 ± 1.7 pm/V, the ZnO nanorods grown by the demonstrated method can be the basis of novel nanomechanical sensors and energy harvesting devices [T2].
4. I have determined the bending modulus of high aspect ratio wurtzite InAs nanowires using two independent methods applied on the same individual nanowires in situ in a scanning electron microscope: a static bending test with a calibrated atomic force microscopy tip; and an electric field induced resonance experiment. By applying the two methods I have determined the Young's modulus of pure wurtzite InAs for the first time; the mean value in the [0001] crystallographic direction was measured to be 43.5 ± 13.6 GPa by the static method and 35.1 ± 3.4 GPa by the dynamic method. The two independent methods led to the same result within the uncertainty range, therefore I have validated the static method by the common dynamic method considered as standard [T3].
5. By applying the validated static bending test I have determined the bending modulus of low aspect ratio, wet chemically grown, vertical ZnO nanorods, which cannot be carried out by the resonance method due to experimental limitations. According to the analytical mechanical model describing the changing cross-section of the nanorods along the longitudinal axis the mean value in the [0001] crystallographic direction was measured to be 32.2 ± 7.4 GPa [T4].

Tézispontok magyarul

1. Hét különböző minőségű ZnO magréteg vizsgálatán keresztül megmutattam, hogy nagyfokú rendezettséget és hangolható geometriát mutató ZnO nanoszálak nedves kémiai előállítására lehetséges megfelelő ZnO magréteg választásával és az elektronsugaras pozicionálás módszerével. Mindez lehetővé teszi a nanoszálak alkalmazását különféle integrált nano- és optoelektronikai eszközökben [T1].
2. Kvantitatív röntgendiffrakciós és transzmissziós elektronmikroszkópos vizsgálatokkal megmutattam, hogy a ZnO nanoszálak kristályszerkezetét és rendezettségét a magrétegben található kristallitok kristályszerkezete és orientációjának szórása határozza meg [T1].
3. A piezoválasz atomi erőmikroszkópia módszerével (piezoresponse force microscopy) elsőként határoztam meg litográfiai úton pozicionált és nedves kémiai úton növesztett ZnO nanorudak [0001] kristálytani irányhoz rendelt (d_{33}) piezoelektromos állandóját. A kapott 8.4 ± 1.7 pm/V-os – azaz meglehetősen magas – piezoelektromos állandó révén a demonstrált eljárás útján növesztett ZnO nanorudak újszerű nanomechanikai érzékelőknek és energia-átalakító eszközöknek alapját képezhetik [T2].
4. Karcsú (high aspect ratio), wurtzit-kristályrácsú InAs nanoszálak hajlítási moduluszát határoztam meg ugyanazon egyedi nanoszálakon két egymástól független, pásztázó elektronmikroszkópban végzett in situ vizsgálattal: statikus hajlítási kísérlettel kalibrált atomi erőmikroszkópos tűvel; valamint periodikusan változó elektromos tér által gerjesztett rezonancia vizsgálattal. Az alkalmazott módszerek segítségével elsőként határoztam meg tisztán wurtzit-kristályrácsú InAs Young-moduluszát, mely a statikus módszerrel 43.5 ± 13.6 GPa, míg a dinamikus módszerrel 35.1 ± 3.4 GPa átlagos értéknek adódott a [0001] kristálytani irányban. A két független módszer a hibahatáron belül azonos eredményre vezetett, így módon a statikus vizsgálati módszert a standardnak tekintett dinamikus méréssel hitelesítettem [T3].
5. A hitelesített statikus hajlítási módszerrel meghatároztam alacsony oldalarányú (low aspect ratio), nedves kémiai úton növesztett, vertikális ZnO nanorudak hajlítási moduluszát, ami a dinamikus rezonancia módszerével kísérleti korlátok miatt nem kivitelezhető. A nanorudak hossztengetly menti változó keresztmetszetét leíró analitikus mechanikai modell alapján a [0001] kristálytani irányhoz tartozó átlagos érték 32.2 ± 7.4 GPa-nak adódott [T4].

10. List of publications

10.1. Papers used to compose the thesis highlights

[T1] **R. Erdélyi**, T. Nagata, D. J. Rogers, F. H. Teherani, Zs. E. Horváth, Z. Lábadi, Zs. Baji, Y. Wakayama, J. Volk: *Investigations into the Impact of the Template Layer on ZnO Nanowire Arrays Made Using Low Temperature Wet Chemical Growth*, *Crystal Growth & Design* **11** (2011) 2515. Impact factor: **4.720**.

[T2] J. Volk, **R. Erdélyi**: *Morphology and crystallinity control of wet chemically grown ZnO nanorods*, accepted for publication in *Turkish Journal of Physics*, DOI: 10.3906/fiz-1405-12

[T3] **R. Erdélyi**, M. H. Madsen, Gy. Sáfrán, Z. Hajnal, I. E. Lukács, G. Fülöp, Sz. Csonka, J. Nygård, J. Volk: *In-Situ Mechanical Characterization of Wurtzite InAs Nanowires*, *Solid State Communications* **152** (2012) 1829. Impact factor: **1.534**.

[T4] **R. Erdélyi**, V. Halász, Z. Szabó, I.E. Lukács, J. Volk: *Mechanical characterization of epitaxially grown zinc oxide nanorods*, *Physica E* **44** (2012) 1050. Impact factor: **1.522**.

10.2. Other papers

[P1] J. Volk, T. Nagata, **R. Erdélyi**, I. Bársony, A. L. Tóth, I. E. Lukács, Zs. Czigány, H. Tomimoto, Y. Shingaya, T. Chikyow: *Highly Uniform Epitaxial ZnO Nanorod Arrays for Nanopiezotronics*, *Nanoscale Research Letters* **4** (2009) 699. Impact factor: **2.894**.

[P2] N. Q. Khánh, I. E. Lukács, Gy. Sáfrán, **R. Erdélyi**, E. Fülöp, A. Deák, J. Volk: *Effect of nanosphere monolayer on the morphology of ZnO nanowires grown by hydrothermal method*, *Materials Letters* **79** (2012) 242. Impact factor: **2.224**.

[P3] J. Volk, Z. Szabó, **R. Erdélyi**, N.Q. Khánh: *Engineered ZnO nanowire arrays using different nanopatterning techniques*, *Proc. of SPIE* **8263** (2012) 82631L.

[P4] Z. Szabó, **R. Erdélyi**, J. Makai, J. Balázs, J. Volk: *Highly ordered three-dimensional ZnO nanorods for novel photonic devices*, *Phys. Status Solidi C* **8** (2011) 2895.

10.3. Participation in conferences

10.3.1. International conferences

[C1] **R. Erdélyi**, I.E. Lukács , V. Halász, J. Volk: *Electromechanical characterization of vertically grown ZnO nanorods*, E-MRS Spring Meeting 2010, Strasbourg, France, 7th-11th June 2010, oral presentation

[C2] **R. Erdélyi**, J. Volk: *ZnO nanowire based mechanical sensor for in vivo applications*, E-MRS Spring Meeting 2012, Strasbourg, France, 14th-18th May 2012, oral presentation

[C3] **R. Erdélyi**, J. Volk: *Novel nanoforce sensor based on vertical ZnO nanorods*, International Workshop on Zinc-oxide and Related Materials (IWZnO) 2012, Nice, France, 11th-14th September 2012, poster presentation

[C4] **R. Erdélyi**, M. S. White, Z. Szabó, J. Volk: *ZnO/transparent organic hole-transport material based solid-state dye-sensitized solar cells*, Metal Oxide / Polymer Nanocomposites and Applications (MOPNA) workshop, Budapest, Hungary, 19th-21th September 2011, invited oral presentation

10.3.2. Domestic conferences

[C5] **R. Erdélyi**, J. Volk: *Egyedi félvezető nanoszálak nanomechanikai vizsgálata*, Műszaki Kémiai Napok 2012, Veszprém, Hungary, 24th-26th April 2012, poster presentation

[C6] **R. Erdélyi**, G. Galántai, J. Volk, I.E. Lukács: *Vertikális cink-oxid nanoszálak mechanikai tulajdonságainak vizsgálata*, VII. Országos anyagtudományi konferencia 2009, Balatonkenese, Hungary, 11th-13th October 2009, oral presentation

11. Acknowledgements

First and foremost I thank my advisor János Volk. It has been an honor to be his first PhD student. I appreciate all his contributions of time, ideas, and funding to make my PhD experience productive and stimulating. I am also grateful to my colleagues in the Semiconductor Nanodevices Group (especially Nguyen Quoc Khánh, István Endre Lukács and Zoltán Szabó) for helpful advice and guidance. The numerical simulations of István Lukács and the help of Levente Illés in SEM bending experiments are greatly appreciated. I am also thankful for the work and collaboration of scientists of the National Institute for Materials Science, especially Takahiro Nagata who measured the XRD patterns of the ZnO nanowire arrays and thin films. The mechanical studies of InAs nanowires discussed in this dissertation would not have been possible without the samples from Morten Hannibal Madsen at the University of Copenhagen. The deposition of ZnO seed layers by Takahiro Nagata (PLD), David J. Rogers (PLD), Ferechteh Hosseini Teherani (PLD), Ágoston Németh (sputtering), Zsófia Baji (ALD), Mykyta Toporkov (MBE), Vitaly Avrutin (MBE), and Jacopo Brivio (CVD) for the examination of the substrate effect was essential. The TEM study of the nanowires by Ákos Koppány Kiss (ZnO) and György Sáfrán (InAs) is acknowledged. I also appreciate any contribution of the colleagues of the MFA MEMS laboratory.

I would also thank Prof. Dr. István Bársony (director of MFA), Prof. Dr. Ferenc Vonderviszt (head of Doctoral School of Molecular- and Nanotechnologies), Dr. Csaba Balázs (former head of the Ceramics and Nanocomposites Department) and Dr. Gábor Battistig (head of the Microtechnology Department) for their support and for providing the necessary background to my research and PhD studies. This work was supported by the European Commission in the frame of the PIEZOMAT project, grant No. 611019.

Last but not least, I would like to thank my family for all their love and support. I am very grateful to my parents and sisters who helped me become the person I am today. I am especially thankful to Kata for her understanding and faithful support as well as her patience and unconditional love. And finally, this work would not have been possible without all of the relaxing and funny moments I have spent with my children, Johanna and Lujza. Thank you!

12. Appendix

12.1. Elasticity theory of wurtzite crystals

For the generalized case, Hooke's law may be expressed as

$$\varepsilon_{ij} = S_{ijkl}\tau_{kl}, \quad (\text{I})$$

where the compliance (S_{ijkl}) is fourth-rank tensor quantity, ε_{ij} and τ_{kl} denote the strain and stress tensors, respectively. The direct consequence of the symmetry in the stress and strain tensors is that only 36 components (instead of 81) of the compliance tensor are independent and distinct terms. Additional simplification of the stress-strain relationship can be realized through applying the Voigt notation:

$$\varepsilon_i = S_{ij}\tau_j. \quad (\text{II})$$

Moreover, due to the symmetry in compliance matrix for the general anisotropic linear elastic solid there are 21 independent elastic constants. By considering the symmetry conditions found in the wurtzite crystal structure of our InAs and ZnO NWs the strain-stress relations are therefore expressed as (c-axis is chosen to be the z-axis):

$$\begin{pmatrix} \varepsilon_1 \\ \varepsilon_2 \\ \varepsilon_3 \\ \varepsilon_4 \\ \varepsilon_5 \\ \varepsilon_6 \end{pmatrix} = \begin{pmatrix} S_{11} & S_{12} & S_{13} & 0 & 0 & 0 \\ S_{12} & S_{11} & S_{13} & 0 & 0 & 0 \\ S_{13} & S_{13} & S_{33} & 0 & 0 & 0 \\ 0 & 0 & 0 & S_{44} & 0 & 0 \\ 0 & 0 & 0 & 0 & S_{44} & 0 \\ 0 & 0 & 0 & 0 & 0 & 2(S_{11}-S_{12}) \end{pmatrix} \begin{pmatrix} \tau_1 \\ \tau_2 \\ \tau_3 \\ \tau_4 \\ \tau_5 \\ \tau_6 \end{pmatrix}. \quad (\text{III})$$

Therefore the Young's modulus in notable crystallographic directions can be deduced from the compliance matrix by the following forms:

$$E_{[2\bar{1}\bar{1}0]} = \tau_1/\varepsilon_1 = (S_{11})^{-1}, \quad (\text{IV})$$

$$E_{[01\bar{1}0]} = \tau_2/\varepsilon_2 = (S_{11})^{-1}, \quad (\text{V})$$

$$E_{[0001]} = \tau_3/\varepsilon_3 = (S_{33})^{-1}. \quad (\text{VI})$$

12.2. Piezoelectric theory of wurtzite ZnO

Piezoelectric crystals produce an electric polarization in response to mechanical deformation as follows:

$$P_m = e_{mj}\varepsilon_j, \quad (\text{VII})$$

where P_m ($m = 1, 2, 3$) are the components of the piezoelectric polarization vector \vec{P} , ε_j ($j = 1, 2, 3, 4, 5, 6$) are the components of the strain tensor, and e_{mj} is the tensor of the piezoelectric stress constants using Voigt notation. For the wurtzite structure of ZnO, the matrix of the latter is written as [31]

$$e_{mj} = \begin{pmatrix} 0 & 0 & 0 & 0 & e_{15} & 0 \\ 0 & 0 & 0 & e_{15} & 0 & 0 \\ e_{31} & e_{31} & e_{33} & 0 & 0 & 0 \end{pmatrix}, \quad (\text{VIII})$$

therefore it has only three independent elements. The inverse piezoelectric effect describes how an applied electric field (E_k) will create a resultant strain (ε_i) which in turn leads to a physical deformation of the material. The inverse piezoelectric effect in Voigt notation can be written as

$$\varepsilon_i = d_{ki}E_k, \quad (\text{IX})$$

where d_{ki} is the tensor of the piezoelectric strain constants. If the latter is considered to be that of the hexagonal wurtzite crystal system then it is

$$d_{ki} = \begin{bmatrix} 0 & 0 & d_{31} \\ 0 & 0 & d_{31} \\ 0 & 0 & d_{33} \\ 0 & d_{15} & 0 \\ d_{15} & 0 & 0 \\ 0 & 0 & 0 \end{bmatrix}. \quad (\text{X})$$

The relationship between stress tensor, strain tensor, electric field and electric displacement (D_m) for a linear piezoelectric material can be given by the constitutive equations [135]:

$$\varepsilon_i = S_{ij}^E \tau_j + d_{mi} E_m, \quad (\text{XI})$$

$$D_m = d_{mi}\tau_i + \xi_{ik}^T E_k, \quad (\text{XII})$$

where the indexes $i, j = 1, 2, \dots, 6$ and $m, k = 1, 2, 3$ refer to different directions within the material coordinate system, and ξ_{ik}^T is the permittivity of the material.

References

- [1] H. Morkoc, U. Özgür, Zinc Oxide: Fundamentals, Materials and Device Technology, Wiley-VCH Verlag GmbH & Co, Weinheim (2007).
- [2] C. Jagadish, S.J. Pearton, Zinc Oxide Bulk, Thin Films and Nanostructures, Elsevier, New York (2006).
- [3] Wikipedia online encyclopedia, ZnO. http://en.wikipedia.org/wiki/Zinc_oxide
- [4] A. Janotti, C.G. Van de Walle, Fundamentals of zinc oxide as a semiconductor, Reports on Progress in Physics 72 (2009) 126501.
- [5] T. Yao, S.K. Hong, Oxide and Nitride Semiconductors: Processing, Properties and Applications, Springer Berlin Heidelberg (2009).
- [6] I. Ivanov, J. Pollmann, Electronic structure of ideal and relaxed surfaces of ZnO: a prototype ionic wurtzite semiconductor and its surface properties, Phys. Rev. B. 24 (1981) 7275.
- [7] Ü. Özgür, Y.I. Alivov, C. Liu, A. Teke, M.A. Reshchikov, S. Doğan, V. Avrutin, S.-J. Cho, H. Morkoç, A comprehensive review of ZnO materials and devices, J. Appl. Phys. 98 (2005) 041301.
- [8] C.D. Look, D.C. Reynolds, J.R. Sizelove, R.L. Jones, C.W. Litton, G. Cantwell, W.C. Harsch, Electrical properties of bulk ZnO, Solid State Commun. 105 (1998) 399.
- [9] F.A. Kohan, G. Ceder, D. Morgan, C.G. Van de Walle, First-principles study of native point defects in ZnO, Phys. Rev. B. 61 (2000) 15019.
- [10] C.G. Van de Walle, Hydrogen as a cause of doping in Zinc oxide, Phys. Rev. Lett. 85 (2000) 1012.
- [11] Y.S. Kim, C.H. Park, Rich variety of defects in ZnO via an attractive interaction between O vacancies and Zn interstitials: Origin of n-type doping, Phys. Rev. Lett. 102 (2009) 086403.
- [12] S.M. Park, T. Ikegami, K. Ebihara, Effects of substrate temperature on the properties of Ga-doped ZnO by pulsed laser deposition, Thin Solid Films 513 (2006) 90.
- [13] B.S. Zhang, S.H. Wei, A. Zunger, A phenomenological model for systematization and prediction of doping limits in II–VI and I–III–VI₂ compounds, J. Appl. Phys. 83 (1998) 3192.
- [14] T. Yamamoto, H. Katayama-Yoshida, Unipolarity of ZnO with a wide band gap and its solution using codoping method, J. Crys. Growth 214 (2000) 552.
- [15] A. Tsukazaki, A. Ohtomo, T. Onuma, M. Ohtani, T. Mahino, M. Sumiya, K. Ohtani, S.F. Chichibu, S. Fuke, Y. Segawa, H. Ohno, H. Koinuma, M. Kawasaki, Repeated temperature modulation epitaxy for p-type doping and light emitting diode based on ZnO, Nat. Mater. 4 (2005) 42.
- [16] J.-R. Duclère, M. Novotny, A. Meaney, R. O’Haire, E. McGlynn, M.O. Henry, J.-P. Mosnier, Properties of Li-, P- and N-doped ZnO thin films prepared by pulsed laser deposition, Superlattices Microstruct. 38 (2005) 397.
- [17] H.S. Jeong, D.G. Yoo, D.Y. Kim, N.E. Lee, J.H. Boo, Physical properties and etching characteristics of metal (Al, Ag, Li) doped ZnO films grown by RF magnetron sputtering, Thin Solid Films 516 (2008) 6598.

- [18] D.P. Singh, Synthesis and Growth of ZnO Nanowires, *Science of Advanced Materials* 2 (2010) 245.
- [19] R. S. Wagner, W. C. Ellis, Vapor-liquid-solid mechanism of single crystal growth, *Appl. Phys. Lett.* 4 (1964) 89.
- [20] P. Yang, C.M. Lieber, Nanostructured high-temperature superconductors: Creation of strong-pinning columnar defects in nanorod/superconductor composites, *J. Mater. Res.* 12 (1997) 2981.
- [21] J. Song, X. Wang, E. Riedo, Z.L. Wang, Elastic Property of Vertically Aligned Nanowires, *Nano Letters* 5 (2005) 1954.
- [22] G.-C. Yi (editor), *Semiconductor Nanostructures for Optoelectronic Devices*, NanoScience and Technology, Springer-Verlag Berlin Heidelberg (2012).
- [23] M.A. Vergés, A. Mifsud, C.J. Serna, Formation of rod-like zinc oxide microcrystals in homogeneous solutions, *J. Chem. Soc., Faraday Trans.* 86 (1990) 959.
- [24] L. Vayssieres, K. Keis, S.-E. Lindquist, A. Hagfeldt, Purpose-Built Anisotropic Metal Oxide Material: 3D Highly Oriented Microrod Array of ZnO, *J. Phys. Chem. B* 105 (2001) 3350.
- [25] L. Vayssieres, Growth of Arrayed Nanorods and Nanowires of ZnO from Aqueous Solutions, *Advanced Materials* 15 (2003) 464.
- [26] D. Yuan, R. Guo, Y. Wei, W. Wu, Y. Ding, Z.L. Wang, S. Das, Heteroepitaxial Patterned Growth of Vertically Aligned and Periodically Distributed ZnO Nanowires on GaN Using Laser Interference Ablation, *Adv. Funct. Mater.* 20 (2010) 3484.
- [27] L. Schmidt-Mende, J.L. MacManus-Driscoll, ZnO – nanostructures, defects, and devices, *Mater. Today* 10 (2007) 40.
- [28] S. Xu, Z.L. Wang, One-dimensional ZnO nanostructures: solution growth and functional properties, *Nano Res.* 4 (2011) 1013.
- [29] M.N.R. Ashfold, R.P. Doherty, N.G. Ndi-for-Angwafor, D.J. Riley, Y. Sun, The kinetics of the hydrothermal growth of ZnO nanostructures, *Thin Solid Films* 515 (2007) 8679.
- [30] C.-H. Lee, G.-C. Yi in “*Semiconductor Nanostructures for Optoelectronic Devices*“, ed. G.-C. Yi, Springer-Verlag Berlin Heidelberg, pp. 37-68 (2012).
- [31] Y. Gao, Z.L. Wang, Electrostatic Potential in a Bent Piezoelectric Nanowire. The Fundamental Theory of Nanogenerator and Nanopiezotronics, *Nano Letters* 7 (2007) 2499.
- [32] X. Wang, J. Zhou, J. Song, J. Liu, N. Xu, Z.L. Wang, Piezoelectric Field Effect Transistor and Nanoforce Sensor Based on a Single ZnO Nanowire, *Nano Letters* 6 (2006) 2768.
- [33] W. Wu, X. Wen, Z.L. Wang, Taxel-Addressable Matrix of Vertical-Nanowire Piezotronic Transistors for Active and Adaptive Tactile Imaging, *Science* 340 (2013) 952.
- [34] Z.L. Wang, J. Song, Piezoelectric Nanogenerators Based on Zinc Oxide Nanowire Arrays, *Science* 312 (2006) 242.
- [35] X. Wang, J. Song, J. Liu, Z.L. Wang, Direct-Current Nanogenerator Driven by Ultrasonic Waves, *Science* 316 (2007) 102.

- [36] M. Alexe, S. Senz, M.A. Schubert, D. Hesse, U. Gösele, Energy Harvesting Using Nanowires?, *Advanced Materials* 20 (2008) 4021.
- [37] M.H. Huang, S. Mao, H. Feick, H. Yan, Y. Wu, H. Kind, E. Weber, R. Russo, P. Yang, Room-Temperature Ultraviolet Nanowire Nanolasers, *Science* 292 (2001) 1897.
- [38] S. Xu, C. Xu, Y. Liu, Y. Hu, R. Yang, Q. Yang, J.-H. Ryou, H.J. Kim, Z. Lochner, S. Choi, R. Dupuis, Z.L. Wang, Ordered Nanowire Array Blue/Near-UV Light Emitting Diodes, *Advanced Materials* 22 (2010) 4749.
- [39] M. Law, L.E. Greene, J.C. Johnson, R. Saykally, P. Yang, Nanowire dye-sensitized solar cells, *Nature Materials* 4 (2005) 455.
- [40] X.-M. Zhang, M.-Y. Lu, Y. Zhang, L.-J. Chen, Z.L. Wang, Fabrication of a High-Brightness Blue-Light-Emitting Diode Using a ZnO-Nanowire Array Grown on p-GaN Thin Film, *Advanced Materials* 21 (2009) 2767.
- [41] H. Kind, H. Yan, B. Messer, M. Law, P. Yang, Nanowire Ultraviolet Photodetectors and Optical Switches, *Advanced Materials* 14 (2002) 158.
- [42] Q. Yang, X. Guo, W. Wang, Y. Zhang, S. Xu, D.H. Lien, Z.L. Wang, Enhancing Sensitivity of a Single ZnO Micro-/Nanowire Photodetector by Piezo-phototronic Effect, *ACS Nano* 4 (2010) 6285.
- [43] Y. Shi, C.Q. Chen, Y.S. Zhang, J. Zhu, Y.J. Yan, Determination of the natural frequency of a cantilevered ZnO nanowire resonantly excited by a sinusoidal electric field, *Nanotechnology* 18 (2007) 075709.
- [44] P. Poncharal, Z.L. Wang, D. Ugarte, W.A. de Heer, Electrostatic Deflections and Electromechanical Resonances of Carbon Nanotubes, *Science* 283 (1999) 1513.
- [45] K.H. Liu, W.L. Wang, Z. Xu, L. Liao, X.D. Bai, E.G. Wang, *In situ* probing mechanical properties of individual tungsten oxide nanowires directly grown on tungsten tips inside transmission electron microscope, *Applied Physics Letters* 89 (2006) 221908.
- [46] C.Q. Chen, Y. Shi, Y.S. Zhang, J. Zhu, Y.J. Yan, Size Dependence of Young's Modulus in ZnO Nanowires, *Physical Review Letters* 96 (2006) 075505.
- [47] D.A. Dikin, X. Chen, W. Ding, G. Wagner, and R.S. Ruoff, Resonance vibration of amorphous SiO₂ nanowires driven by mechanical or electrical field excitation, *Journal of Applied Physics* 93 (2003) 226.
- [48] J. Fujita, M. Ishida, T. Sakamoto, Y. Ochiai, T. Kaito, S. Matsui, Observation and characteristics of mechanical vibration in three-dimensional nanostructures and pillars grown by focused ion beam chemical vapor deposition, *Journal of Vacuum Science & Technology B* 19 (2001) 2834.
- [49] M.-F. Yu, O. Lourie, M.J. Dyer, K. Moloni, T.F. Kelly, R.S. Ruoff, Strength and Breaking Mechanism of Multiwalled Carbon Nanotubes Under Tensile Load, *Science* 287 (2000) 637.
- [50] C.H. Lin, M. Chang, X. Li, J.R. Deka, Measurement of Mechanical Properties of Boron Nanowire Using Nano-manipulation System, *Proceedings of the 35th International MATADOR Conference* (2007) pp 275-278.
- [51] F. Xu, Q. Qin, A. Mishra, Y. Gu, Y. Zhu, Mechanical Properties of ZnO Nanowires Under Different Loading Modes, *Nano Research* 3 (2010) 271.

- [52] Y. Zhu, H.D. Espinosa, An electromechanical material testing system for *in situ* electron microscopy and applications, *Proc. Natl. Acad. Sci.* 102 (2005) 14503.
- [53] M. Naraghi, I. Chasiotis, H. Kahn, Y. Wen, Y. Dzenis, Novel method for mechanical characterization of polymeric nanofibers, *Review of Scientific Instruments* 78 (2007) 085108.
- [54] M. Naragh, T. Ozkan, I. Chasiotis, S.S. Hazra, M.P. de Boer, MEMS platform for on-chip nanomechanical experiments with strong and highly ductile nanofibers, *Journal of Micromechanics and Microengineering* 20 (2010) 125022.
- [55] E.W. Wong, P.E. Sheehan, C.M. Lieber, Nanobeam Mechanics: Elasticity, Strength, and Toughness of Nanorods and Nanotubes, *Science* 277 (1997) 1971.
- [56] A. San Paulo, J. Bokor, R.T. Howe, R. He, P. Yang, D. Gao, C. Carraro, R. Maboudian, Mechanical elasticity of single and double clamped silicon nanobeams fabricated by the vapor-liquid-solid method, *Applied Physics Letters* 87 (2005) 053111.
- [57] H. Ni, X. Li, H. Gao, Elastic modulus of amorphous SiO₂ nanowires, *Applied Physics Letters* 88 (2006) 043108.
- [58] B. Wu, A. Heidelberg, J.J. Boland, Mechanical Properties of Ultrahigh Strength Gold Nanowires, *Nature Materials* 4 (2005) 525.
- [59] B. Wen, J.E. Sader, J.J. Boland, Mechanical Properties of ZnO Nanowires, *Physical Review Letters* 101 (2008) 175502.
- [60] E. Celik, I. Guven, E. Madenci, Mechanical characterization of nickel nanowires by using a customized atomic force microscope, *Nanotechnology* 22 (2011) 155702.
- [61] X. Li, H. Gao, C.J. Murphy, K.K. Caswell, Nanoindentation of Silver Nanowires, *Nano Letters* 3 (2003) 1495.
- [62] S. Hoffmann, F. Östlund, J. Michler, H.J. Fan, M. Zacharias, S.H. Christiansen, C. Ballif, Fracture strength and Young's modulus of ZnO nanowires, *Nanotechnology* 18 (2007) 205503.
- [63] M.P. Manoharan, A.V. Desai, G. Neely, M.A. Haque, Synthesis and Elastic Characterization of Zinc Oxide Nanowires, *Journal of Nanomaterials* 2008 (2008) 849745.
- [64] P.E. Marszalek, W.J. Greenleaf, H. Li, A.F. Oberhauser, J.M. Fernandez, Atomic force microscopy captures quantized plastic deformation in gold nanowires, *Proc. Natl. Acad. Sci.* 97 (2000) 6282.
- [65] Y. Huang, X. Bai, Y. Zhang, *In situ* mechanical properties of individual ZnO nanowires and the mass measurement of nanoparticles, *J. Phys.: Condens. Matter* 18 (2006) L179.
- [66] J. Zhou, C.S. Lao, P. Gao, W. Mai, W.L. Hughes, S.Z. Deng, N.S. Xu, Z.L. Wang, Nanowire as pico-gram balance at workplace atmosphere, *Solid State Commun.* 139 (2006) 222.
- [67] Y. Huang, Y. Zhang, X. Wang, X. Bai, Y. Gu, X. Yan, Q. Liao, J. Qi, J. Liu, Size Independence and Doping Dependence of Bending Modulus in ZnO Nanowires, *Cryst. Growth Des.* 9 (2009) 1640.
- [68] A.V. Desai, M.A. Haque, Mechanical properties of ZnO nanowires, *Sens. Actuators A-Phys.* 134 (2007) 169.

- [69] R. Agrawal, B. Peng, E.E. Gdoutos, H.D. Espinosa, Elasticity Size Effects in ZnO Nanowires—A Combined Experimental-Computational Approach, *Nano Lett.* 8 (2008) 3668.
- [70] M.-R. He, Y. Shi, W. Zhou, J.W. Chen, Y.J. Yan, J. Zhu, Diameter dependence of modulus in zinc oxide nanowires and the effect of loading mode: *In situ* experiments and universal core-shell approach, *Appl. Phys. Lett.* 95 (2009) 091912.
- [71] M.-Y. Choi, D. Choi, M.-J. Jin, I. Kim, S.-H. Kim, J.-Y. Choi, S.Y. Lee, J.M. Kim, S.-W. Kim, Mechanically Powered Transparent Flexible Charge-Generating Nanodevices with Piezoelectric ZnO Nanorods, *Adv. Mater.* 21 (2009) 2185.
- [72] I.B. Kobiakov, Elastic, piezoelectric and dielectric properties of ZnO and CdS single crystals in a wide range of temperatures, *Solid State Commun.* 35 (1980) 305.
- [73] R. Jenkins, R.L. Snyder, *Introduction to X-ray Powder Diffractometry*, John Wiley & Sons, New York (1996).
- [74] P.R. Rudolf, B.G. Landes, Two-dimensional X-ray Diffraction and Scattering of Microcrystalline and Polymeric Materials, *Spectroscopy* 9 (1994) 22.
- [75] S.N. Sulyanov, A.N. Popov, D.M. Kheiker, Using a Two-dimensional Detector for X-ray Powder Diffractometry, *J. Appl. Cryst.* 27 (1994) 934.
- [76] J. Mayer, L.A. Giannuzzi, T. Kamino, J. Michael, TEM Sample Preparation and FIB-Induced Damage, *MRS Bulletin* 32 (2007) 400.
- [77] High-resolution Scanning Electron Microscope: Model HFS-2, *Hitachi Review*, 21 (1972) 262.
- [78] M. Nambi, A. Damani, J.J. Abbott, Toward Intuitive Teleoperation of Micro/Nano-Manipulators with Piezoelectric Stick-Slip Actuators, 2011 IEEE/RSJ International Conference on Intelligent Robots and Systems, September 25-30, 2011. San Francisco, CA, USA, pp. 445-450.
- [79] Kleindiek Nanotechnik MM3A-EM. <http://www.nanotechnik.com/>
- [80] G. Binnig, C.F. Quate, C. Gerber, Atomic Force Microscope, *Phys. Rev. Lett.* 56 (1986) 930.
- [81] S.V. Kalinin, B.J. Rodriguez, S. Jesse, E. Karapetian, B. Mirman, E.A. Eliseev, A.N. Morozovska, Nanoscale Electromechanics of Ferroelectric and Biological Systems: A New Dimension in Scanning Probe Microscopy, *Annu. Rev. Mater. Res.* 37 (2007) 189.
- [82] Z.L. Wang, Energy Harvesting Using Piezoelectric Nanowires—A Correspondence on “Energy Harvesting Using Nanowires?” by Alexe *et al.*, *Adv. Mater.* 21 (2009) 1311.
- [83] J. Zhou, P. Fei, Y. Gao, Y. Gu, J. Liu, G. Bao, Z.L. Wang, Mechanical-Electrical Triggers and Sensors Using Piezoelectric Microwires/Nanowires, *Nano Lett.* 8 (2008) 2725.
- [84] S.Y. Kim, H.W. Jang, J.K. Kim, C.M. Jeon, W.I. Park, G.-C. Yi, J.-L. Lee, Low-Resistance Ti/Al Ohmic Contact on Undoped ZnO, *Journal of Electronic Materials*, 31 (2002) 868.
- [85] H.-K. Kim, S.-H. Han, T.-Y. Seong, W.-K. Choi, Low-resistance Ti/Au ohmic contacts to Al-doped ZnO layers, *Applied Physics Letters* 77 (2000) 1647.
- [86] J. L. Tan, J Tien, D. M. Pirone, D. S. Gray, K. Bhadriraju, C. S. Chen, Cells lying on a bed of microneedles: An approach to isolate mechanical force, *Proc. Natl. Acad. Sci.* 100 (2003) 1484.

- [87] M.-T. Chen, M.-P. Lu, Y.-J. Wu, J. Song, Ch.-Y. Lee, M.-Y. Lu, Y.-Ch. Chang, L.-J. Chou, Z.L. Wang, L.-J. Chen, Near UV LEDs Made with in Situ Doped p-n Homojunction ZnO Nanowire Arrays, *Nano Lett.* 10 (2010) 4387.
- [88] G. Shen, P.-C. Chen, K. Ryu, C. Zhou, Devices and chemical sensing applications of metal oxide nanowires, *J. Mater. Chem.* 19 (2009) 828.
- [89] J. Qiu, X. Li, F. Zhuge, X. Gan, X. Gao, W. He, S.-J. Park, H.-K. Kim, Y.-H. Hwang, Solution-derived 40 μ m vertically aligned ZnO nanowire arrays as photoelectrodes in dye-sensitized solar cells, *Nanotechnology* 21 (2010) 195602.
- [90] J. Volk, A. Håkansson, H.T. Miyazaki, T. Nagata, J. Shimizu, T. Chikyow, Fully engineered homoepitaxial zinc oxide nanopillar array for near-surface light wave manipulation, *Appl. Phys. Lett.* 92 (2008) 183114.
- [91] S.H.G. Teo, A.Q. Liu, J. Singh, M.B. Yu, G.Q. Lo, Rod type photonic crystal optical line defect waveguides with optical modulations, *Appl. Phys. A: Mater.* 89 (2007) 417.
- [92] J.X. Wang, X.W. Sun, Y. Yang, H. Huang, Y.C. Lee, O.K. Tan, L. Vayssieres, Hydrothermally grown oriented ZnO nanorod arrays for gas sensing applications, *Nanotechnology* 17 (2006) 4995.
- [93] J. Volk, T. Nagata, R. Erdélyi, I. Bársony, A.L. Tóth, I.E. Lukács, Zs. Czigány, H. Tomimoto, Y. Shingaya, T. Chikyow, Highly Uniform Epitaxial ZnO Nanorod Arrays for Nanopiezotronics, *Nanoscale Res. Lett.* 4 (2009) 699.
- [94] R. Liu, A.A. Vertegel, E.W. Bohannon, T.A. Sorenson, J.A. Switzer, Epitaxial Electrodeposition of Zinc Oxide Nanopillars on Single-Crystal Gold, *Chem. Mater.* 13 (2001) 508.
- [95] X. Wang, J. Song, P. Li, J.H. Ryou, R.D. Dupuis, C.J. Summers, Z.L. Wang, Growth of Uniformly Aligned ZnO Nanowire Heterojunction Arrays on GaN, AlN, and Al_{0.5}Ga_{0.5}N Substrates, *J. Am. Chem. Soc.* 127 (2005) 7920.
- [96] M. Wang, Ch.-H. Ye, Y. Zhang, H.-X. Wang, X.-Y. Zeng, L.-D. Zhang, Seed-layer controlled synthesis of well-aligned ZnO nanowire arrays via a low temperature aqueous solution method, *J. Mater. Sci.: Mater. Electron.* 19 (2008) 211.
- [97] J. Song, S. J. Lim, Effect of Seed Layer on the Growth of ZnO Nanorods, *Phys. Chem. C* 111 (2007) 596.
- [98] T.-U. Kim, J.-A. Kim, S. M. Pawar, J.-H. Moon, J. H. Kim, Creation of Nanoscale Two-Dimensional Patterns of ZnO Nanorods using Laser Interference Lithography Followed by Hydrothermal Synthesis at 90 °C, *Cryst. Growth Des.* 10 (2010) 4256.
- [99] Y.-J. Kim, Ch.-H. Lee, Y. J. Hong, G.-Ch. Yi, S.S. Kim, H. Cheong, Controlled selective growth of ZnO nanorod and microrod arrays on Si substrates by a wet chemical method, *Appl. Phys. Lett.* 89 (2006) 163128.
- [100] Y. Wei, W. Wu, R. Guo, D. Yuan, S. Das, Z.L. Wang, Wafer-Scale High-Throughput Ordered Growth of Vertically Aligned ZnO Nanowire Arrays, *Nano Lett.* 10 (2010) 3414.
- [101] D. J. Rogers, F.H. Teherani, A. Ougazzaden, S. Gautier, L. Divay, A. Lusson, O. Durand, F. Wyczisk, G. Garry, T. Monteiro, M.R. Correia, M. Peres, A. Neves, D. McGruther, J.N. Chapman,

- M. Razeghi, Use of ZnO thin films as sacrificial templates for metal organic vapor phase epitaxy and chemical lift-off of GaN, *Appl. Phys. Lett.* 91 (2007) 071120.
- [102] Zs. Baji, Z. Lábadi, Zs.E. Horváth, Gy. Molnár, J. Volk, I. Bársony, P. Barna, Nucleation and Growth Modes of ALD ZnO, *Cryst. Growth Des.* 12 (2012) 5615.
- [103] M. Zerdali, S. Hamzaoui, F.H. Teherani, D. Rogers, Growth of ZnO thin film on SiO₂/Si substrate by pulsed laser deposition and study of their physical properties, *Mater. Lett.* 60 (2006) 504.
- [104] T. Kim, M. Yoshitake, S. Yagyu, S. Nemsak, T. Nagata, T. Chikyow, XPS study on band alignment at Pt–O-terminated ZnO(000 $\bar{1}$) interface, *Surf. Interface Anal.* 42 (2010) 1528.
- [105] Á. Németh, Cs. Major, M. Fried, Z. Lábadi, I. Bársony, Spectroscopic ellipsometry study of transparent conductive ZnO layers for CIGS solar cell applications, *Thin Solid Films* 516 (2008) 7016.
- [106] B.B. He, Introduction to two-dimensional X-ray diffraction, *Powder Diffr.* 18 (2003) 71.
- [107] P.F. Fewster, X-ray scattering from semiconductors; Imperial College Press: London (2000) Chapter 4, pp 167-276.
- [108] I. Ohkubo, A. Ohtomo, T. Ohnishi, Y. Mastumoto, H. Koinuma, M. Kawasaki, In-plane and polar orientations of ZnO thin films grown on atomically flat sapphire, *Surf. Sci.* 443 (1999) L1043–L1048.
- [109] C.S. Steplecaru, M.S. Martín-González, J.F. Fernandez, J.L. Costa-Krämer, How to prevent twin formation in epitaxial ZnO thin films grown on c-plane sapphire, *Thin Solid Films* 518 (2010) 4630.
- [110] K.S.A. Butcher, P. Afifuddin, P.-T. Chen, M. Godlewski, A. Sczerbakow, E.M. Goldys, T.L. Tansley, J.A. Freitas, Recrystallization prospects for freestanding low-temperature GaN grown using ZnO buffer layers, *Journal of Crystal Growth* 246 (2002) 237.
- [111] Zs. Baji, Z. Lábadi, Gy. Molnár, B. Pécz, K. Vad, Zs.E. Horváth, P.J. Szabó; T. Nagata, J. Volk, Highly conductive epitaxial ZnO layers deposited by ALD, *Thin Solid Films* 562 (2014) 485.
- [112] A. Ougazzaden, D.J. Rogers, F.H. Teherani, G. Orsal, T. Moudakir, S. Gautier, V.E. Sandana, F. Jomard, M. Abid, M. Molinari, M. Troyon, P.L. Voss, D. McGrouther, J.N. Chapman, Epitaxial MOVPE growth of highly c-axis oriented InGa_N/Ga_N films on ZnO-buffered Si (111) substrates, *Proc. SPIE* 7603 (2010) 76031D-1.
- [113] D.A. Scrymgeour, J.W.P. Hsu, Correlated Piezoelectric and Electrical Properties in Individual ZnO Nanorods, *Nano Lett.* 8 (2008) 2204.
- [114] D.F. Crisler, J.J. Cupal, A.R. Moore, *Proc. IEEE* 56 (1968) 225.
- [115] T. Ogawa, H. Oikawa, A. Kojima, Decrement of Piezoelectric Constants Caused by Screening Effect of Conduction Electrons on the Effective Charge of CdS Crystals, *Jpn. J. Appl. Phys.* 10 (1971) 593.
- [116] P.B. Barna, M. Adamik, in "Science and Technology of Thin Films", ed. F.C. Maticotta and G. Ottaviani, World Scientific Publishing Co., Singapore, pp. 1-28 (1995).
- [117] R.J. Lad, P.D. Funkenbusch, C.R. Aita, Postdeposition annealing behavior of rf sputtered ZnO films, *J. Vac. Sci. Technol.* 17 (1980) 808.

- [118] V. Gupta, A. Mansingh, Influence of postdeposition annealing on the structural and optical properties of sputtered zinc oxide film, *J. Appl. Phys.* 80 (1996) 1063.
- [119] P.H. Dupont, C. Couteau, D.J. Rogers, F.H. T  herani, G. L  rondel, Waveguiding-assisted random lasing in epitaxial ZnO thin film, *Appl. Phys. Lett.* 97 (2010) 261109.
- [120] C. Sartel, V. Sallet, A. Lusson, N. Haneche, J.M. Laroche, P. Galtier, D.J. Rogers, F.H. Teherani, Homoepitaxy of ZnO on bulk and thin film substrates by low temperature metal organic chemical vapor deposition using tert-butanol, *J. Vac. Sci. Technol. B* 27 (2009) 1615.
- [121] L. Meirovich, *Elements of Vibration Analysis*, McGraw-Hill, New York (1986).
- [122] A.G. Milnes, A.Y. Polyakov, Indium arsenide: a semiconductor for high speed and electro-optical devices, *Mater. Sci. Eng. B* 18 (1993) 237.
- [123] S.O. Mariager, D. Khakhulin, H.T. Lemke, K.S. Kj  r, L. Guerin, L. Nuccio, C.B. S  rensen, M.M. Nielsen, R. Feidenhans'l, Direct observation of acoustic oscillations in InAs nanowires, *Nano Lett.* 10 (2010) 2461.
- [124] M. Lexholm, I. Karlsson, F. Boxberg, D. Hessman, Optical determination of Young's modulus of InAs nanowires, *Appl. Phys. Lett.* 95 (2009) 113103.
- [125] M. Koguchi, H. Kakibayashi, M. Yazawa, K. Hiruma, T. Katsuyama, Crystal Structure Change of GaAs and InAs Whiskers from Zinc-Blende to Wurtzite Type, *Jpn. J. Appl. Phys.* 31 (1992) 2061.
- [126] P. Caroff, K.A. Dick, J. Johansson, M.E. Messing, K. Deppert, L. Samuelson, Controlled polytypic and twin-plane superlattices in III–V nanowires, *Nat. Nanotechnol.* 4 (2009) 50.
- [127] H. Shtrikman, R. Popovitz-Biro, A. Kretinin, L. Houben, M. Heiblum, M. Buka  a, M. Galicka, R. Buczko, P. Kacman, Method for Suppression of Stacking Faults in Wurtzite III–V Nanowires, *Nano Lett.* 9 (2009) 1506.
- [128] J.M. Gere, S.P. Timoshenko, *Mechanics of Materials*, Third Edition, PWS-Kent Publishing Company, Boston, Massachusetts (1990).
- [129] H. Shu, X. Chen, H. Zhao, X. Zhou, W. Lu, Structural Stability and Electronic Properties of InAs Nanowires and Nanotubes: Effects of Surface and Size, *J. Phys. Chem. C* 114 (2010) 17514.
- [130] R.M. Martin, Relation between Elastic Tensors of Wurtzite and Zinc-Blende Structure Materials, *Phys. Rev. B* 6 (1972) 4546.
- [131] L.G. Zhou, H. Huang, Are surfaces elastically softer or stiffer?, *Appl. Phys. Lett.* 84 (2004) 1940.
- [132] H.S. Park, W. Cai, H.D. Espinosa, H. Huang, *MRS Bull.* 34 (2009) 178.
- [133] J.P. Cleveland, S. Manne, D. Bocek, P.K. Hansma, A nondestructive method for determining the spring constant of cantilevers for scanning force microscopy, *Rev. Sci. Instrum.* 64 (1993) 403.
- [134] J.E. Boercker, J.B. Schmidt, E.S. Aydil, Transport Limited Growth of Zinc Oxide Nanowires, *Crystal Growth and Design* 9 (2009) 2783.
- [135] S.O.R. Moheimani, A.J. Fleming, in "Piezoelectric Transducers for Vibration Control and Damping", Springer-Verlag London, pp. 9-35 (2006).